

**CONSTRAINING THE DENSITY  
DEPENDENCE OF SYMMETRY ENERGY  
USING MEAN FIELD MODELS**

*By*  
**CHIRANJIB MONDAL**  
**PHYS05201204016**

**Saha Institute of Nuclear Physics, Kolkata**

*A thesis submitted to the*

*Board of Studies in Physical Sciences*

*In partial fulfillment of requirements*

*For the Degree of*

**DOCTOR OF PHILOSOPHY**

*of*

**HOMI BHABHA NATIONAL INSTITUTE**



**October, 2017**



# Homi Bhabha National Institute

## Recommendations of the Viva Voce Committee

As members of the Viva Voce Committee, we certify that we have read the dissertation prepared by **Chiranjib Mondal** entitled “**Constraining the density dependence of symmetry energy using mean-field models**” and recommend that it may be accepted as fulfilling the thesis requirement for the award of Degree of Doctor of Philosophy.

\_\_\_\_\_ Date:

Chairman - Prof. Munshi Golam Mustafa

\_\_\_\_\_ Date:

Guide / Convener - Prof. Bijay Kumar Agrawal

\_\_\_\_\_ Date:

Co-guide - (if any)

\_\_\_\_\_ Date:

External Examiner - Prof. Praveen C. Srivastava

\_\_\_\_\_ Date:

Member 1 - Prof. Debades Bandyopadhyay

\_\_\_\_\_ Date:

Member 2 - Prof. Maitreyee Saha Sarkar

\_\_\_\_\_

Final approval and acceptance of this thesis is contingent upon the candidate's submission of the final copies of the thesis to HBNI.

I/We hereby certify that I/we have read this thesis prepared under my/our direction and recommend that it may be accepted as fulfilling the thesis requirement.

**Date:**

**Place:**

**Guide:** \_\_\_\_\_



## **STATEMENT BY AUTHOR**

This dissertation has been submitted in partial fulfillment of requirements for an advanced degree at Homi Bhabha National Institute (HBNI) and is deposited in the Library to be made available to borrowers under rules of the HBNI.

Brief quotations from this dissertation are allowable without special permission, provided that accurate acknowledgement of source is made. Requests for permission for extended quotation from or reproduction of this manuscript in whole or in part may be granted by the Competent Authority of HBNI when in his or her judgment the proposed use of the material is in the interests of scholarship. In all other instances, however, permission must be obtained from the author.

Chiranjib Mondal



## **DECLARATION**

I, hereby declare that the investigation presented in the thesis has been carried out by me. The work is original and has not been submitted earlier as a whole or in part for a degree / diploma at this or any other Institution / University.

Chiranjib Mondal





---

---

# LIST OF PUBLICATIONS ARISING FROM THE THESIS

---

## Peer reviewed journal:

1. Constraining the symmetry energy content of nuclear matter from nuclear masses: A covariance analysis.  
Chiranjib Mondal, Bijay Agrawal and J. N. De;  
*Physical Review C*, **2015**, *92*, 024302 [arXiv:1507.05384]
2. Sensitivity of elements of the symmetry energy of nuclear matter to the properties of neutron-rich systems.  
Chiranjib Mondal, Bijay Agrawal, J. N. De and S. K. Samaddar;  
*Physical Review C*, **2016**, *93*, 044328 [arXiv:1603.08645]
3. Model dependence of the neutron-skin thickness on the symmetry energy.  
Chiranjib Mondal, B. K. Agrawal, M. Centelles, G. Colò, X. Roca-Maza, N. Paar, X. Viñas, S. K. Singh and S. K. Patra;  
*Physical Review C*, **2016**, *93*, 064303 [arXiv:1605.05048]

4. Interdependence of different symmetry energy elements.

Chiranjib Mondal, B. K. Agrawal, J. N. De, S. K. Samaddar, M. Centelles  
and X. Viñas;

*Physical Review C (Rapid Communication)*, **2017**, 96, 021302 [arXiv:1708.03846]

#### **Contribution other than thesis:**

1. Limiting symmetry energy elements from empirical evidence.

Bijay Agrawal, J. N. De, S. K. Samaddar, Chiranjib Mondal and Subhranil De;

*International Journal of Modern Physics E*, **2017**, 26, 1750022 [arXiv:1703.03549]

#### **Conference proceeding:**

1. Model dependence in the density content of nuclear symmetry energy

Chiranjib Mondal, S. K. Singh, B. K. Agrawal, M. Centelles, G. Colò, X. Roca-Maza, N. Paar, S. K. Patra and X. Viñas;

*Proceedings of the DAE-BRNS Symp. on Nucl. Phys.*, **2014**, 59, 66-67.

2. Information content of nuclear masses: A covariance analysis

Chiranjib Mondal, Bijay Agrawal and J. N. De;

*Proceedings of the DAE-BRNS Symp. on Nucl. Phys.*, **2015**, 60, 56-57.

3. Sensitivity analysis of optimized nuclear energy density functional

Chiranjib Mondal, Bijay Agrawal, J. N. De and S. K. Samaddar;

*Proceedings of the DAE-BRNS Symp. on Nucl. Phys.*, **2016**, 61, 66-67.

Chiranjib Mondal

**To My Family  
and Ajit da ...**



## ACKNOWLEDGEMENTS

Probably no gratitude is enough for the constant support provided by Prof. Bijay Kumar Agrawal, who has been the supervisor for this project. I was introduced to the subject of theoretical nuclear physics by him. The amount of inquisitiveness and enthusiasm he has to offer towards the subject is truly inspiring. I am forever in debt to him for making me love the subject. The relationship with him was never limited to the discussion of Physics. The biggest lesson I learned from him is that the path of morale and hardship is always the right path in life. I also acknowledge the fatherly guidance and care of Prof. Jadunath De and Prof. Santosh Samaddar, with whom I was so privileged to collaborate for a number of occasions. The wisdom and the stories what they shared, will always bring a joyous smile in my face. I also acknowledge the help provided by Mrs. Tanuja Agrawal during any technical difficulties. She has been a true inspiration for solving the puzzle called 'life'.

I take great pleasure to express my gratitude towards Prof. Xavier Vi nas and Prof. Mario Centelles for collaborating at different phases of this thesis work, who had also hosted me at University of Barcelona offering very warm hospitality during April, 2017. I take this opportunity to thank all my other collaborators Prof. Gianluca Col'ò, Xavier Roca-Maza, Nils Paar, Prof. Suresh Kumar Patra, Shailesh Kumar Singh and Subhranil De. Name of Tuhin Malik needs a special mention, as he is not only a collaborator but also a good friend. I also want to thank the members of my doctoral committee Prof. Debades Bandyopadhyay, Prof. Munshi Golam Mustafa and Prof. Maitreyee Saha Sarkar for giving very useful suggestions. I also acknowledge the careful guidance of Prof. Asimananda Goswami during my Post-MSc project.

I gratefully acknowledge the financial support provided by Department of Atomic En-

ergy, Govt. of India throughout the whole project. The support was also extended for attending several school, workshop and conferences.

I started the journey of my PhD with a very vibrant set of people at Saha Institute of Nuclear Physics (SINP) back in 2012, the so called Post MSc batch. It has been a memorable last five years with these wonderful people. I thank all of you from the bottom of my heart. I am sure the journey with most of you will be life-long. Achyut da, Kuntal da, Suvankar, Gouranga da, I will cherish the friendship what we have developed during last five years and beyond. Naosad da, Satyajit, Pankaj, Sayanee, Sanjib da, Sukanta, Mily and all the other students of our Post MSc year, I acknowledge the presence of you around me whenever I needed it. Thank you for all those trips together, what brought a lot of oxygen into life.

I thank all the present and past members of Theory Division, who actively helped in this project. To name a few, Parijat di, Prasanta da, Satya da, Goutam da, thank you for your elderly suggestions at the time of my need. Thank you Aminul da for sharing your thoughts about life. I also want to record my appreciation for Kumar da, Augniva, Avik (Jr), Aranya, Sukannya, Mugdha and all the other members of 3319. A significant part of the numerical calculations of this project was carried out by using the computer cluster facility of Theory Division, SINP. I also appreciate the official jobs taken care by Pradyut da, Dola di and Sangita di and the other non-academic members of the Theory division. I heartily recognize the friendships what I have developed with people outside the Theory division, to name a few, Samrat, Abhishek, Sudesna, Maireyee, Samik and many others. Suparna, I will cherish all the wonderful conversations we had during last two years or so.

Life has blessed me with lot of good friends, who often showed the best ways to deal with a problem, becoming the best teachers. Ananta, Suchandan, Amitava and Buddha, without you life would not be this beautiful. Gagan and Arshiya, it has been a pleasure

having you in my life.

Now comes the members of MSA-II, with whom I spent the last five years of my life. I have very fond memories of those birthday celebrations with Kuntal, Amrita, Barnamala, Binita, Sanjukta, Tirthankar and Aritra. Discussions with Tirthankar (Tirtha) probably brought out the best of my way of life. Whatever doubts or questions I used to have, Tirtha always had the best words to describe it. Sanjukta, I always dream to be as compassionate as you. I have no other words to describe you. Aritra, I will cherish your witty silences and silly jokes. Tirtha, Sanjukta and Aritra, it was one hell of a journey together. Kuntal, the memories we created together won't fade easily.

I express my deepest love and respect towards my family for being at my side, no matter what paths I have chosen so far in my life. Believe me, *Baba-Ma*, I wish I could show my admiration more! *Didibhai*, thank you for all your support.

Before I finish, I want to pay my tribute to *Ajit da*. Your words still inspire me, "*sobai bole choroibeti, choroibeti! Ami boli thamte sekh.*"

Chiranjib Mondal

---

---

# CONTENTS

---

<b>Synopsis</b>	<b>iv</b>
<b>List of Figures</b>	<b>viii</b>
<b>List of Tables</b>	<b>xiv</b>
<b>1 Introduction</b>	<b>1</b>
<b>2 Mean Field Models</b>	<b>10</b>
2.1 Introduction . . . . .	10
2.2 Finite nuclei . . . . .	11
2.2.1 Skyrme Formalism . . . . .	11
2.2.2 Relativistic Mean Field formalism . . . . .	17
2.2.3 Pairing in BCS approximation . . . . .	24
2.3 Infinite Nuclear Matter . . . . .	29
<b>3 Error Analysis</b>	<b>32</b>
3.1 Introduction . . . . .	32



3.2	Covariance analysis . . . . .	33
3.3	Minimization and Sensitivity analysis . . . . .	42
<b>4</b>	<b>Constraining the symmetry energy parameters using a relativistic mean field model</b>	<b>45</b>
4.1	Introduction . . . . .	45
4.2	A Covariance analysis . . . . .	49
4.2.1	Fit data and model parameters . . . . .	49
4.2.2	Results . . . . .	51
4.3	A sensitivity analysis . . . . .	54
4.3.1	The RMF models SINPB and SINPA . . . . .	55
4.3.2	Results for SINPB and SINPA . . . . .	58
4.3.3	Nuclear Matter properties at high density . . . . .	66
4.4	Summary . . . . .	69
<b>5</b>	<b>Model dependence in the symmetry energy parameters</b>	<b>71</b>
5.1	Introduction . . . . .	71
5.2	Neutron-skin thickness and symmetry energy parameters in Droplet Model . . . . .	73
5.3	Results and discussions . . . . .	78
5.3.1	Correlation plots associated with isovector indicators . . . . .	79
5.3.2	Systematic differences between the families of functionals . . . . .	85
5.4	Summary . . . . .	90

<b>6</b>	<b>Interdependence among the symmetry energy parameters</b>	<b>92</b>
6.1	Introduction . . . . .	92
6.2	Theoretical Framework . . . . .	95
6.2.1	Symmetric Nuclear Matter . . . . .	95
6.2.2	Asymmetric Nuclear Matter . . . . .	100
6.2.3	Symmetry energy parameters . . . . .	102
6.3	Results and discussion . . . . .	105
6.4	Summary . . . . .	113
<b>7</b>	<b>Summary and Future outlook</b>	<b>114</b>
	<b>Bibliography</b>	<b>118</b>

---

---

## SYNOPSIS

---

Apart from a very few light nuclei, all terrestrial finite nuclei are asymmetric. In other words, for most of the finite nuclei, number of neutrons is higher than protons. Competition between Coulomb energy and symmetry energy makes them asymmetric. On the other extreme, astrophysical objects like neutron stars are also highly asymmetric. However, the reason behind asymmetry in neutron star is attributed to charge neutrality and beta equilibrium of the system. The density associated with the center of the nucleus is very close to saturation density ( $\rho_0 = 0.16 \text{ fm}^{-3} = 2.7 \times 10^{14} \text{ gm/cm}^3$ ) of infinite nuclear matter. Density at the core of a neutron star is four to five times  $\rho_0$ . The symmetry energy controls the radii of neutron stars, the thicknesses of their crusts, the rate of cooling of neutron stars, and the properties of nuclei involved in r-process nucleosynthesis. Studying symmetry energy and its density dependence over a wide range of density is thus a major topic of research for past few decades. Presently, several laboratories around the world are set up to test the limits of stability of nuclei towards the neutron drip-line or super-heavy region. A precise understanding of density dependence of symmetry energy can facilitate to explore new areas of research, which might help to understand the isovector part of the effective nucleon-nucleon interaction inside the nucleus, which is still not known

accurately.

Density dependence of symmetry energy can be characterized essentially by three quantities, namely, symmetry energy  $J$ , slope parameter  $L$  and curvature parameter  $K_{sym}$ ; all of these quantities pertain to infinite nuclear matter at the density  $\rho_0$ . To find reliable constraints on  $J$ ,  $L$  or  $K_{sym}$  one needs to relate them with experimental observables of finite nuclei or neutron stars since infinite nuclear matter can not be accessed in laboratories. Due to computational limitations, starting from no-core shell model, finding even the ground state properties of finite nuclei e.g. binding energy, charge radii etc beyond  $^{40}\text{Ca}$  is yet far fetched. Over the years mean field models with very few parameters thus became a viable alternative to calculate the properties of finite nuclei spanning the entire periodic table as well as of neutron stars.

Fitting few thousand observed nuclear masses within a finite range droplet model (FRDM) or taking double differences of nuclear masses the estimated value of symmetry energy  $J$  at saturation is  $\sim 32$  MeV with an accuracy of 1-2 MeV [1, 2]. Droplet model (DM) suggests that neutron-skin thickness  $\Delta r_{np}$  (difference between root mean square radii of neutron and proton distribution) of a heavy nucleus is linearly correlated to the slope parameter  $L$  [3, 4]. This correlation was verified by using a representative set of relativistic and non-relativistic mean field models. There have been several attempts to measure the neutron-skin thickness of  $^{208}\text{Pb}$ . However, the most model independent measurement at Jefferson lab (Lead radius experiment or PREX), based on weak interaction, predicts a value with very large uncertainty [5–7]. There have also been attempts to look for alternative isovector probes e.g isovector giant dipole resonance (IVGDR) [8–11], isospin diffusion [12],  $\pi^+ - \pi^-$  ratio etc. The uncertainty associated with the value of slope parameter  $L$  still remains large. The shrouds of uncertainty looms even larger when one tries to constrain curvature parameter  $K_{sym}$ .

In this dissertation, our primary goal is to constrain the density dependence of symmetry energy by obtaining tighter bounds on  $L$  and  $K_{sym}$  using some relativistic and non-relativistic mean field models. The investigation has been carried out by using two different methods. Firstly, covariance analysis is employed to study the relations among different experimental observables and parameters of a relativistic mean field model. We attempt to constrain the density dependence of symmetry energy by incorporating in the fit-data the binding energies of some highly asymmetric nuclei; binding energies of finite nuclei are the most accurately measured quantities in nuclear physics. Secondly, using different mean field models existing in the literature, we tried to explore new model independent correlations among different isovector sensitive quantities.

In the study based on covariance method, we observed that parameters of mean field models obtained by fitting binding energies and charge radii of few closed shell nuclei predict a wide range of values for the slope parameter  $L$  [13–15]. However, macroscopic FRDM model obtained by fitting binding energies of few thousand nuclei predicts a quite restricted value of  $L$  [1]. Inspired by this result we incorporated for the first time binding energies of some highly asymmetric nuclei ( $^{24}\text{O}$ ,  $^{30}\text{Ne}$ ), where the neutron number is twice to that of protons, in the fit-data in order to optimize the parameters of a relativistic mean field model. Our detailed investigation clearly reveals that the inclusion of highly asymmetric nuclei in the fitting protocol reduces the uncertainty on the symmetry energy elements significantly. A sensitivity analysis is performed by including further in the fitting protocol the binding energies of few more highly asymmetric nuclei ( $^{36}\text{Mg}$ ,  $^{58}\text{Ca}$ ) together with the measured maximum mass of neutron star [16]. Such an analysis reveals quantitatively the sensitivity of binding energies of highly asymmetric nuclei to the symmetry energy parameters. It also shows that maximum mass of neutron star has some sensitivity to the symmetry energy parameters.

Using a representative set of different mean-field models, we found that correlation between neutron-skin thickness  $\Delta r_{np}$  of  $^{208}\text{Pb}$  with slope parameter  $L$  is model dependent [17]. A model independent correlation was found between slope parameter  $L$  and bulk part of the neutron skin thickness  $\Delta r_{np}^{bulk}$  of  $^{208}\text{Pb}$  conjectured by DM. Models from different families predicting similar values of  $L$ , show a variation in  $\Delta r_{np}$  which is few times higher than what is predicted by DM. We defined an effective value of slope parameter  $L_{eff}$  within local density approximation, pertaining to the average density of a heavy nucleus. Variation in  $L_{eff}$  seems to be in harmony with variation in  $\Delta r_{np}$  predicted by DM.

Having constrained the slope of symmetry energy  $L$ , we also explored the possibility of constraining the symmetry curvature parameter  $K_{sym}$ . Considering a general form of the density dependent nucleon nucleon interaction along with the Gibbs-Duhem relation we found an analytical relation connecting curvature parameter  $K_{sym}$ , slope parameter  $L$  and symmetry energy  $J$ . Using five hundred mean field models both relativistic and non-relativistic, this correlation was realized between  $K_{sym}$  with linear combination of  $L$  and  $J$ . The correlation stood out further for few realistic as well as finite range Gogny interactions. The universality in the correlation of  $K_{sym}$  with linear combination of  $L$  and  $J$  strongly suggests that a tight bound on  $K_{sym}$  can be obtained from bounds on  $L$  and  $J$ .

---



---

## LIST OF FIGURES

---

1.1	Nuclear chart for $\sim 6000$ nuclei in the $N$ - $Z$ plane. See text for details. . . . .	2
1.2	Structure of a neutron star depicting constituents of different layers along with the density and range associated with the corresponding layers. The density $\rho_0$ depicted in the figure is the saturation density of symmetric infinite nuclear matter. . . . .	4
3.1	Covariance ellipsoids for two pairs of observables as given in Ref. [61]. See text for details. . . . .	37
3.2	Relative Sensitivity of different parameters of UNEDF1 [68] to different type of data used in the fit, as given in Ref. [62]. . . . .	44
4.1	$\Delta r_{np}$ of $^{208}\text{Pb}$ plotted as a function of $L_0$ (left panel) and $\frac{L_0}{C_2^0}$ (right panel), for $\sim 40$ mean-field models as given in Ref [15]. . . . .	46
4.2	The binding energy difference $\Delta B(^{132}\text{Sn}, ^{100}\text{Sn}) = BE(^{132}\text{Sn}) - BE(^{100}\text{Sn})$ plotted against neutron-skin thickness $\Delta r_{np}$ of the $^{132}\text{Sn}$ nucleus for different mean-field models as shown in Ref. [76]. . . . .	47

4.3	The binding energy difference $\Delta BE(X, Y) = BE(X) - BE(Y)$ for four different pairs of isotopes are plotted against neutron-skin thickness $\Delta r_{np}$ in the $^{208}\text{Pb}$ nucleus for 16 different RMF models (See text for details). The values of correlation coefficients $r$ are also displayed. . . . .	48
4.4	The covariance ellipsoids for the parameters $g_\rho - \eta_{2\rho}$ (upper panel) and the corresponding $L_0 - \Delta r_{np}$ (lower panel) for the model I (blue) and model II (red). The area inside the ellipsoids indicate the reasonable domain of the parameters. . . . .	52
4.5	The correlation between $\Delta r_{np}$ of $^{208}\text{Pb}$ and different fit-data on binding energies used to obtain the model parameters of model-II. . . . .	54
4.6	Optimum values of the objective function ( $\chi_0^2$ ) are plotted as a function of $\Delta r_{np}$ (neutron skin of $^{208}\text{Pb}$ ) for two families of models, namely, SINPB-Variant and SINPA-Variant (see text for details). . . . .	61
4.7	Binding energy differences $\Delta B (=BE(\text{SINPB}) - BE(\text{SINPA}))$ extracted using models SINPB and SINPA for even isotopes of O, Ca and Ni nuclei plotted as a function of asymmetry $\delta$ . . . . .	62
4.8	Relative sensitivity of different parameters of the effective Lagrangian density to three groups of fit data used in optimization of SINPA. These groups are nuclear binding energies ( $BE$ ), charge radii ( $r_{ch}$ ) and maximum mass of neutron star ( $M_{max}^{NS}$ ). . . . .	63
4.9	Same as Fig. 4.8, but, with different grouping of the fit data of finite nuclei. One group contains binding energies of highly asymmetric nuclei ( $^{24}\text{O}$ , $^{30}\text{Ne}$ , $^{36}\text{Mg}$ and $^{58}\text{Ca}$ ) and another contains remaining fit data on the finite nuclei. . . . .	64
4.10	Relative sensitivity of the nuclear matter properties at saturation density to the fit data of SINPA with the same grouping as in Fig. 4.9. . . . .	65



4.11	Binding energy per nucleon for symmetric matter $\mathcal{E}$ , symmetry energy parameter $C_2$ and its density derivative $L$ along with their errors as a function of density $\rho/\rho_0$ for SINPB and SINPA. . . . .	67
4.12	Square of the effective mass of $\rho$ meson (scaled by $10^5$ ) as a function of density $\rho/\rho_0$ plotted for SINPB and SINPA. . . . .	69
5.1	Plots for the difference between the symmetry energy coefficient for infinite nuclear matter $C_2^0$ and that for finite nuclei $a_{\text{sym}}(A)$ as a function of the neutron-skin thickness (left panels) and of the bulk part of the neutron-skin thickness (right panels). The results are obtained using five different families of mean-field models, namely, FSV (blue squares), TSV (red circles), DDME (green triangles), SAMi-J (orange diamonds) and KDE0-J (maroon inverted triangles). The correlation coefficients are: $C(C_2^0 - a_{\text{sym}}(A), \Delta r_{\text{np}}) = 0.972$ (0.967) and $C(C_2^0 - a_{\text{sym}}(A), \Delta r_{\text{np}}^{\text{bulk}}) = 0.988$ (0.979) for $^{208}\text{Pb}$ ( $^{132}\text{Sn}$ ) nuclei. The inner (outer) colored regions depict the loci of the 95% confidence (prediction) bands of the regression [121]. . . . .	80
5.2	Plots for the ratio of the nuclear symmetry energy coefficient for finite nuclei $a_{\text{sym}}(A)$ to that for infinite nuclear matter $C_2^0$ , as a function of the neutron-skin thickness (left panels) and of the bulk part of the neutron-skin thickness (right panels). The square shaded region in the upper-left panel corresponds to $a_{\text{sym}}(A) = 22.4 \pm 0.3$ [122] MeV and $C_2^0 = 32.3 \pm 1.3$ MeV [31]. The correlation coefficients are $ C(a_{\text{sym}}(A)/C_2^0, \Delta r_{\text{np}})  = 0.965$ (0.959) and $ C(a_{\text{sym}}(A)/C_2^0, \Delta r_{\text{np}}^{\text{bulk}})  = 0.992$ (0.989) for $^{208}\text{Pb}$ ( $^{132}\text{Sn}$ ) nuclei. The inner (outer) colored regions depict the loci of the 95% confidence (prediction) bands of the regression [121]. . . . .	81

5.3	Neutron-skin thickness (left) and its bulk (middle) and surface (right) contributions for the $^{132}\text{Sn}$ nucleus plotted against the same quantities for the $^{208}\text{Pb}$ nucleus. The shaded region corresponds to the values of the neutron-skin thickness in $^{132}\text{Sn}$ determined from the ones estimated for the $^{208}\text{Pb}$ nucleus (see also Fig. 5.2). The correlation coefficients obtained for the results presented in the left, middle and right panels are 0.999, 0.993 and 0.995, respectively. The inner (outer) colored regions depict the loci of the 95% confidence (prediction) bands of the regression [121]. . . . .	83
5.4	Plots for the symmetry energy slope parameter $L_0$ as a function of the neutron-skin thickness (left), its bulk part (middle) and its surface part (right) for the $^{208}\text{Pb}$ nucleus. The shaded region in the left panel projects out the values of $L_0 = 62 \pm 15$ MeV obtained from $\Delta r_{\text{np}} = 0.193 \pm 0.028$ fm which, in turn, is obtained by using the empirical values of $C_2^0$ and $a_{\text{sym}}(A)$ (see also Fig. 5.2). The arrow marks in the left panel indicate the points with the slope parameter $L_0 \sim 65$ MeV. The values of the correlation coefficients are $C(L_0, \Delta r_{\text{np}}) = 0.950$ , $C(L_0, \Delta r_{\text{np}}^{\text{bulk}}) = 0.963$ and $C(L_0, \Delta r_{\text{np}}^{\text{surf}}) = 0.469$ . The inner (outer) colored regions depict the loci of the 95% confidence (prediction) bands of the regression [121]. . . . .	84
5.5	The nuclear symmetry energy $C_2$ (lower panel) and its density derivative $C_2'$ multiplied by $3\rho_0$ (upper panel) as a function of density for the five different models associated with the slope parameter for nuclear matter $L_0 \sim 65$ MeV. Each of these models belongs to a different family (see also Table 5.1). . . . .	86
5.6	The variation of $r^2\rho(r)I^2(r)$ as a function of the radial coordinate $r$ in $^{208}\text{Pb}$ for the five models that yield a symmetry energy slope parameter $L_0 \sim 65$ MeV.	89

6.1	Values of $L_0$ plotted against $C_2^0$ as obtained from 500 EDFs based on both relativistic and non-relativistic mean-field [13, 14]. The black circles correspond to the non-relativistic Skyrme-inspired EDFs and the red squares refer to those obtained from relativistic mean field (RMF) models. . . . .	93
6.2	The correlation between $L_0$ and $K_{sym}^0$ is plotted for 500 relativistic and non-relativistic EDFs [13, 14]. The black circles correspond to the non-relativistic Skyrme-inspired EDFs, the red squares refer to those obtained from relativistic mean field (RMF) models. . . . .	94
6.3	The correlation between $K_{sym}^0$ and $[3C_2^0 - L_0]$ as obtained from 500 EDFs [13, 14]. The black circles correspond to the Skyrme-inspired EDFs, the red squares refer to those obtained from RMF models. The models consistent with all the constraints demanded by Dutra et al. are highlighted by orange circles for Skyrme EDFs [13] and blue squares for RMF EDFs [14]. The inner (outer) colored regions around the best-fit straight line through these points depict the loci of 95% confidence (prediction) bands of the regression analysis. . . . .	105
6.4	The correlation line between $K_{sym}^0$ and $[3C_2^0 - L_0]$ obtained from the Skyrme-RMF models in Fig. (6.3) is depicted. The magenta triangles are the results obtained from EDFs with realistic interactions, MDI(0), MDI(1), MDI(-1) [131], APR [141], BHF [142], BCPM [143] and SBM [144], respectively. The green diamonds represent results from a few Gogny interactions [130]. . . . .	106
6.5	The correlation between $Q_{sym}^0$ and $[3C_2^0 - L_0]$ as obtained from 500 EDFs [13, 14]. The black circles correspond to the Skyrme-inspired EDFs, the red squares refer to those obtained from RMF models. . . . .	107

6.6	The correlation between $Q_{sym}^0$ and $[3C_2^0 - L_0]$ as obtained from $\sim 200$ EDFs chosen from [13, 14] with constraints on $K_0 = 230 \pm 30$ and $\frac{m_0^*}{m} = 0.75 \pm 0.1$ . The black circles correspond to the Skyrme-inspired EDFs, the red squares refer to those obtained from RMF models. . . . .	108
6.7	Contours of constant $L_0$ , $K_{sym}^0$ , $Q_{sym}^0$ and $\Delta m_0^*$ in color shades (as indicated on the right side of each panel) as functions of the input nuclear constants $C_2^0$ , $C_2^1$ and $\rho_0$ depicting the interdependence between various symmetry energy elements. The values of $L_0$ , $K_{sym}^0$ and $Q_{sym}^0$ are in units of MeV and those for $\Delta m_0^*$ are in units of the free nucleon mass. For details, see text. . . . .	112

---



---

## LIST OF TABLES

---

4.1	The best fit values for the parameters of model-I and model-II. $m_\sigma$ is the mass of $\sigma$ meson given in units of MeV. The masses of $\omega$ and $\rho$ mesons are kept fixed to $m_\omega = 782.5$ MeV and $m_\rho = 763$ MeV and nucleon mass is taken to be $M = 939$ MeV. Statistical errors on the fitted parameters are also given for both the models. . . . .	50
4.2	Observables $\mathcal{O}$ of different nuclei, adopted errors on them $\Delta\mathcal{O}$ , their experimental values and the ones obtained for model-I and II. $BE$ and $r_{ch}$ refers to binding energy and charge radius of a nucleus respectively, and $\Delta B$ is binding energy difference of two isotopes of a nucleus as indicated. $BE$ and $\Delta B$ are in units of MeV and $r_{ch}$ in fm. . . . .	51
4.3	The values for the binding energy per nucleon $\mathcal{E}_0$ , incompressibility coefficient $K_0$ , Dirac effective mass of nucleon $M^*/M$ , symmetry energy coefficient $C_2^0$ and density slope parameter of symmetry energy $L_0$ for the nuclear matter evaluated at saturation density $\rho_0$ along with the correlated errors on them obtained within the covariance analysis for the models I and II. The results for neutron-skin thickness $\Delta r_{np}$ in $^{48}\text{Ca}$ , $^{132}\text{Sn}$ and $^{208}\text{Pb}$ are also presented. . . . .	53

4.4	Optimum values of the parameters for the models SINPB and SINPA, statistical errors on them are given. Mass of the $\sigma$ meson ( $m_\sigma$ ) is given in units of MeV. The masses of $\omega$ and $\rho$ mesons are kept fixed to $m_\omega=782.5$ MeV and $m_\rho=763$ MeV and nucleon mass is taken to be $M=939$ MeV. . . . .	55
4.5	Various observables $\mathcal{O}$ , adopted errors on them $\Delta\mathcal{O}$ , corresponding experimental data (Expt.) and their best-fit values for SINPB and SINPA. $BE$ and $r_{ch}$ corresponds to binding energy and charge radius of a nucleus, respectively and $M_{max}^{NS}$ is the maximum mass of neutron star (NS). Values of $BE$ are given in units of MeV and $r_{ch}$ in fm. $M_{max}^{NS}$ is in units of Solar Mass ( $M_\odot$ ). . . . .	57
4.6	Different nuclear matter properties: the binding energy per nucleon for symmetric matter $\mathcal{E}_0$ , incompressibility coefficient $K_0$ , Dirac effective mass of nucleon $M_0^*$ (scaled by nucleon mass $M$ ), symmetry energy coefficient $C_2^0$ and density slope parameter of symmetry energy $L_0$ for the nuclear matter evaluated at saturation density $\rho_0$ along with the correlated errors on them for the models SINPB and SINPA. The values of $C_2(\rho_c)$ and $L(\rho_c)$ calculated at crossing density $\rho_c$ along with the neutron skin $\Delta r_{np}$ in $^{208}\text{Pb}$ are also presented for these two models. . . . .	59
5.1	Comparison of the properties of infinite nuclear matter (NM) and of the $^{208}\text{Pb}$ and $^{132}\text{Sn}$ nuclei for the five different models that yield a value of $L_0$ around 65 MeV. . . . .	88



---

## CHAPTER 1

---

# INTRODUCTION

---

An atom possesses a tiny positive core surrounded by negatively charged electrons. This positive core is coined as nucleus. Although, the most of the mass of an atom is carried by its nucleus, the size of an atom is orders of magnitude higher compared to its nucleus. The length scale associated to an atom is few angstroms ( $10^{-10}$  meter) whereas size of a nucleus is few femtometers ( $10^{-15}$  meter). The nucleus not only contains positively charged protons, but also electrically neutral neutrons. Due to the presence of protons, which are positively charged, binding of a nucleus has to overcome Coulomb repulsion. That is why nuclear force needs to be very strong in nature. The tiny size of the nucleus further suggests that the nuclear force is a short-range one in nature. Unlike atoms, a nucleus is a self-bound many-body system. Perturbing a nucleus by colliding a particle or by means of electromagnetic probes gives rise a plethora of phenomena like rotation, giant collective vibration, deformation and unique nuclear phenomena like fission or fusion. That is why even after a century of discovery of nucleus by Rutherford, understanding the nature of nuclear force inside the medium presents various unique challenges both in theoretical



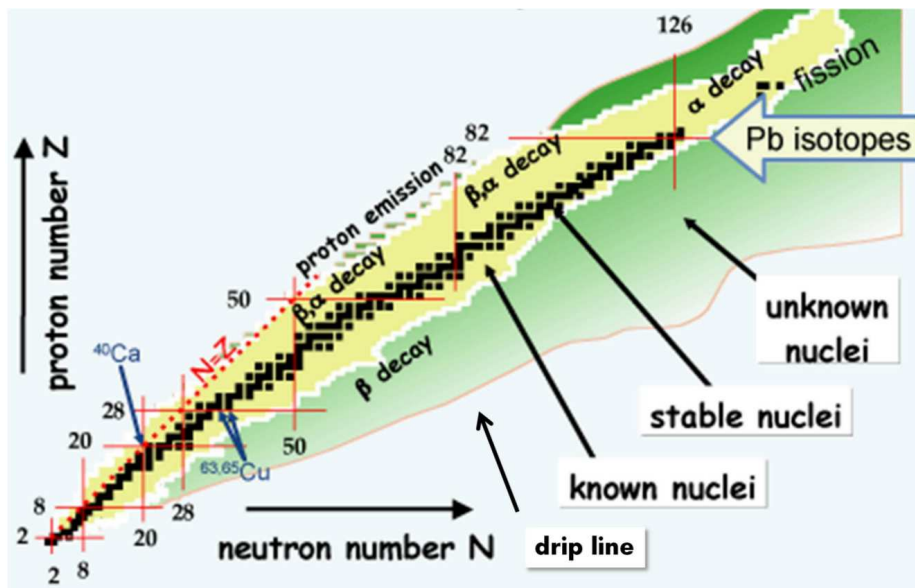


Figure 1.1: Nuclear chart for  $\sim 6000$  nuclei in the  $N$ - $Z$  plane. See text for details.

and experimental studies.

Since the discovery of neutron by Chadwick in 1932, the study of nuclei has become even more fascinating. Based on the number of protons ( $Z$ ) inside a nucleus, chemical nature of the corresponding atom (element) changes. However, it is the number of neutrons ( $N$ ) in a nucleus which plays a decisive role in its binding and eventually determining the stability and abundance of different isotopes ( $A = N + Z$ ). Based on the knowledge so far, there exist  $\sim 118$  different elements with  $\sim 300$  stable isotopes. One should keep in mind that by “stable” it is meant that the half-life of decay for these nuclei are of the order of the age of the earth. In the nuclear chart depicted in Fig. 1.1, these stable isotopes are marked as black dots. Through various experiments performed over the years, existence of  $\sim 2700$  unstable nuclei are also found. These unstable nuclei are displayed by yellow region in Fig. 1.1. There exist a few nuclei with certain number of neutrons and/or protons (magic numbers), which show a greater amount of stability compared to their neighbours. These nuclei are called magic nuclei, which are marked with red horizontal (magic  $Z$ ) and vertical

(magic  $N$ ) lines in Fig. 1.1. The green region, largely occupying the neutron-rich region depicts the nuclei whose existence are predicted by different theoretical conjectures, but not yet found experimentally. During the evolution of a star, heavier nuclei are thought to be formed through rapid neutron-capture process or r-process, which involves the nuclei lying in the green region shown in Fig. 1.1. Beyond this green region, the boundary given by red line depicts the neutron drip line. It signifies that beyond this line adding or subtracting a neutron from a nucleus does not cost any energy. The neutron drip line and the red dotted line representing  $N = Z$  points out that apart from a very few light nuclei, most of the terrestrial finite nuclei are asymmetric.

Upon discovery of neutron star in 1967, a new dimension opened up in the research of systems made up of nucleons i.e. neutrons and protons. When a massive star with mass greater than 10 times the solar mass exhausts its nuclear fuel, it starts collapsing under gravity resulting in a supernova explosion [18]. The remnant of this explosion further collapses under gravity and end up in one of the most compact objects in the universe, called neutron stars. Due to the enormous amount of gravitational pull, the electrons inside the stellar matter collide with the protons forming neutrons. Further gravitational pull tries to bring these neutrons closer and closer. However, Pauli's exclusion principle restricts two neutrons to occupy the same quantum state resulting in an opposing pressure to that of the gravitational pull. In the steady state, the matter inside this compact object is in beta equilibrium and electrically neutral. This results in the primary constituent of these compact objects being neutrons and hence the name neutron star.

The heaviest neutron star observed so far has twice the mass of sun [19, 20] and radius of about 10 to 15 kilometers. The compactness can be understood by looking into the fact that the radius of sun is  $\sim 6.9 \times 10^5$  kilometers. The generic features of a typical neutron star is depicted in Fig. 1.2. It is conjectured that at the very core of a neutron star there

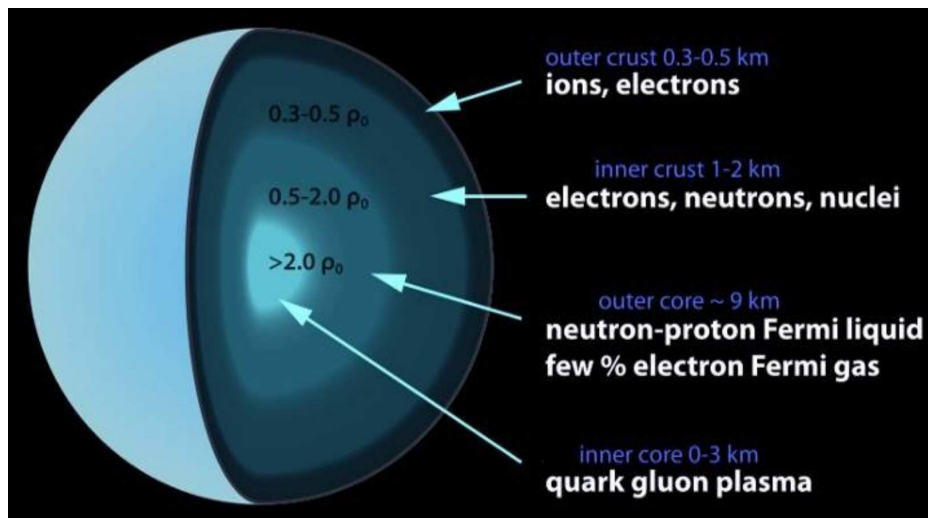


Figure 1.2: Structure of a neutron star depicting constituents of different layers along with the density and range associated with the corresponding layers. The density  $\rho_0$  depicted in the figure is the saturation density of symmetric infinite nuclear matter.

might be a possibility of finding the matter in its most fundamental form i.e. quark-gluon plasma. The outer core, which constitutes the major part of the volume of a neutron star is thought to be beta-equilibrated, electrically neutral nuclear matter with a typical ratio of  $N/Z \approx 6$  and small amount of electron Fermi gas. The crust of the neutron star can be imagined to be made of an inner and outer crust. In the inner crust, there might be still some possibility of occurring the usual nuclear reactions what happens inside a burning star. Possibly very neutron rich nuclei along with free neutrons and electrons are thought to be the constituents of the inner crust. The outer crust is mainly made of cold ions and electrons.

Terrestrial finite nuclei and the neutron stars are complex many-body systems governed by the strong force. Quantum chromodynamics (QCD) is the most fundamental theory which can explain the properties of these nuclear systems. However, tremendous amount of challenges are faced when one tries to solve the theory in non-perturbative regime for a complex many-body system. Only very recently, the state-of-the-art computational fa-

cilities made it possible for theorists to develop some *ab initio* approaches to calculate the ground state properties of nuclei like binding energy or charge radius, based on QCD [21, 22]. However, it has only been possible for lighter nuclei. To calculate the properties of finite nuclei as well as of neutron star in the same framework has only been possible for effective mean-field theories with a few degrees of freedom. These theories are developed on the basis of an *energy density functional* (EDF) with few parameters. There are mainly two types EDFs used in the literature: non-relativistic and relativistic. Skyrme functional is the most popular EDF in the non-relativistic domain where the nucleons interact through local effective potentials. Relativistic mean field models provide a covariant description of the nuclear system which is based on quantum field theory. A comprehensive discussion on the mean-field models can be found in Ref. [23]. The parameters of the mean-field models are obtained by fitting gross nuclear properties which contain the many-body correlations. That is why, even if the mean-field EDFs are constructed by one body densities, the many-body effects get embedded in the parameters of the model. At a nominal computational cost, mean-field models based on EDFs provide a very high accuracy on the global nuclear properties both in the domain of finite nuclei and neutron stars.

From the discussions of Figs. 1.1 and 1.2 it is clear that most of the nuclear systems are asymmetric across a scale of 18 orders of magnitude (length scale associated to finite nuclei is  $10^{-15}$  meter and for neutron star it is  $10^3$  meter). Inside a nucleus, strength of the interaction of a neutron ( $n$ ) - proton ( $p$ ) pair is stronger compared to a  $n$ - $n$  or  $p$ - $p$  pair. In other words, in the absence of any Coulomb force, all finite nuclei would be symmetric with same number of neutrons and protons. In reality, there is always a competition between the Coulomb energy and the symmetry energy what makes most of the finite nuclei asymmetric. In neutron star, however, the requirement of charge neutrality and beta equilibrium is primarily responsible for the asymmetry. Nuclear symmetry energy, char-

acterized by the variation of the energy of a nuclear system with the change in the ratio of its neutron and proton content, plays a crucial role in the binding of the corresponding nuclear system. Symmetry energy also plays crucial roles in controlling the radii of neutron stars, the thickness of their crusts and the properties of nuclei produced in the r-process nucleosynthesis [24].

The density associated with the center of a nucleus is  $\sim 0.16 \text{ fm}^{-3}$  or  $2.7 \times 10^{14} \text{ gm/cm}^3$ . Density at the core of a neutron star is 5-6 times to this density. A microscopic description of symmetry energy along with its density dependence over a wide range of density is thus a major topic of research in nuclear physics. Moreover, across several laboratories nuclei are being synthesized near the drip-lines. Nuclei near neutron-drip lines carry valuable informations regarding the r-process nucleosynthesis in the stellar matter. Understanding of terrestrial nuclei from the conventional theories often fail to explain the properties of nuclides in these extremely asymmetric regions. A precise knowledge of symmetry energy and its density dependence is thus inevitable in order to explore this region of “*terra-incognita*”. Conversely, inputs from experiments performed in these asymmetric nuclei hold the key to improve the existing nuclear theories to be applied to the physics near drip-lines.

To understand the behavior of different nuclear systems, a hypothetical system is defined which is called infinite nuclear matter. It is a system of infinite number of neutrons and protons which is uniform in nature with no boundary and Coulomb interaction. This simplified system helps to understand the bare nucleon-nucleon interaction. In general, nuclear matter can be asymmetric. The energy density of such a system can be decomposed into a symmetric and a purely asymmetric part. The symmetric matter saturates at a certain density where the energy density corresponding to it becomes minimum. The density is called as saturation density  $\rho_0$ . One should note that the density at the center of a heavy

nucleus is very close to  $\rho_0$ . The asymmetric part of the energy is essentially called the symmetry energy of nuclear matter. Symmetry energy is mainly characterized by three parameters namely, symmetry energy coefficient  $C_2^0$ , its density slope  $L_0$  and curvature parameter  $K_{sym}^0$ ; all of these quantities are defined at  $\rho_0$ . Proper definitions of these nuclear matter properties are given in Section 2.3 of Chapter 2.

Constraining quantitatively the symmetry energy parameters  $C_2^0$ ,  $L_0$  and  $K_{sym}^0$  has been a major focus of research in present day nuclear physics. One should keep in mind that these parameters are defined in the domain of infinite nuclear matter. As nuclear matter is not accessible in laboratories one needs to connect these quantities to actual experimentally measurable entities. These connections often imply finding correlation between the symmetry energy parameters and some experimentally measurable quantities using theoretical models. Conventionally, the correlations can be studied using different models. A classic example would be studying correlation between  $L_0$  and neutron-skin thickness  $\Delta r_{np}$  of a heavy nucleus, where  $\Delta r_{np}$  is defined by the difference between the root mean square radii of the neutron and proton distributions inside a nucleus [15]. The models which are explored in the present thesis work, are primarily based on mean-field approach. Over the years mean-field models, both relativistic and non-relativistic, proved to be very successful at very reasonable computing costs. The accuracies over extracted quantities, however, are at par with theories based on more fundamental approaches e.g. *ab-initio* method or configuration-interaction method. A theoretical edifice to calculate the ground state properties like binding energy and charge radius of closed-shell spherical nuclei using mean-field models is given in Chapter 2. It includes discussion of Skyrme models based on a non-relativistic mean-field as well as a relativistic mean-field model. Chapter 2 also incorporates a discussion on properties of infinite nuclear matter which are extracted used different men-field models in the present thesis work. Different correlations mentioned

above can also be studied using a single model by applying the method of covariance analysis. Apart from the correlations one can also study the errors on the model parameters and calculated observables. These informations are very important to benchmark the findings of a theoretical model. How one can study the errors on quantities of interest along with different correlations are discussed in Chapter 3.

Out of the three symmetry energy parameters mentioned above,  $C_2^0$  has been known to lie in good confidence in the range  $\sim 32 \pm 4$  MeV from different experimental data. Using the finite range droplet model [1] or studying the double differences of experimental nuclear masses [2], the error bar is further reduced to  $\sim 0.5$  MeV. Exploration on the slope parameter  $L_0$ , however, shows a wide variation. The value of  $L_0$  may lie in the range from 20 MeV - 120 MeV [15]. There have been a tremendous amount of effort to constrain the value of  $L_0$  from several experimental findings in finite nuclei and astrophysical observations [10, 15, 25–38]. Among different experimental data, binding energies are the most accurately known experimental quantities. However, using binding energies of few closed shell spherical nuclei, mean-field models fail to constrain the value of  $L_0$  (c.f. Fig. 4.1) in a narrow range. In Chapter 4 we reconcile this view by using binding energies of some extremely asymmetric nuclei, where number of neutrons is twice to that of protons, to obtain the parameters of a relativistic mean-field model [39, 40]. A covariance analysis accompanied by a sensitivity analysis is performed further to find the merits of incorporating these highly asymmetric nuclei in the fitting protocol. Correlations existing between different quantities are also explored.

As mentioned above,  $\Delta r_{np}$  of a heavy nucleus like  $^{208}\text{Pb}$  is correlated to  $L_0$ , which was originally proposed in Ref. [15] by using Droplet Model [3, 4]. This correlation was realized by using  $\sim 40$  mean-field models. We find this correlation has some degree of model dependence [17] which is discussed in Chapter 5 in view of Droplet Model.

Compared to  $L_0$ , the uncertainty creeps in by even in larger amount for the case of curvature parameter  $K_{sym}^0$ . Across several mean-field models both relativistic and non-relativistic, the values of  $K_{sym}^0$  lie within a huge range,  $-700 \text{ MeV} < K_{sym}^0 < 400 \text{ MeV}$ . The value of  $K_{sym}^0$  plays quite a significant role in determining the symmetry energy behavior of highly asymmetric dense matter e.g. in neutron star or supernova explosion. There has been no attempt till date to constrain the value of  $K_{sym}^0$  from experimental data. Theoretical calculations connecting poorly known  $K_{sym}^0$  to other comparatively better known nuclear matter properties may hold the key to pin down the value of  $K_{sym}^0$  [41, 42]. In Chapter 6 a simple model based on fundamental laws of statistical mechanics is proposed. Analytical relations between different symmetry energy parameters are derived further. Special importance is given to the relatively poorly known quantity  $K_{sym}^0$ . A linear correlation is suggested by the simple model between  $K_{sym}^0$  and other nuclear matter properties. The correlation was realized by using 500 mean-field models used in the literature which shows the near-universality in the correlation which is proposed.

In a nutshell, this thesis aims towards constraining the different symmetry energy parameters using different mean-field models. Contents of different chapters are described very briefly above. Special attention was given to those parameters which controls the density dependence of symmetry energy. A brief summary and future outlooks are discussed in Chapter 7.



---

# MEAN FIELD MODELS

---

## 2.1 Introduction

*Ab initio* methods based quantum chromodynamics (QCD) or configuration interaction are the most fundamental theories to describe the many-body nuclear systems like finite nuclei or neutron stars [21, 22]. However, the computational cost is too high to calculate even the ground state properties of lighter nuclei (mass number  $A \leq 40$ ) with these methods. Unless there is an unprecedented improvement in the modern day computing facilities, it will be extremely unlikely to provide even the ground state description of heavy or super-heavy nuclei with these *ab-initio* approaches. On the contrary, mean field models provide a coherent description of astrophysical objects like neutron stars as well as terrestrial finite nuclei throughout the whole nuclear chart at a very nominal computational cost with quite high accuracy.

In this thesis work mainly two class of mean-field models are employed namely, a non-relativistic variant based on zero range Skyrme force [43, 44] and a relativistic one formulated on the basis of interaction between nucleons through mesons [45, 46]. The

parameters of these two variants of mean-field models are obtained by fitting experimental data on binding energy and charge radii of closed shell nuclei. In this chapter, we discuss the method to obtain the binding energy and charge radii for closed shell nuclei along with the properties of infinite nuclear matter in the mean-field framework.

## 2.2 Finite nuclei

In the present thesis work, mostly we have dealt with closed shell spherical nuclei. The ground state properties are calculated within Hartree-Fock approximation both with the non-relativistic Skyrme and relativistic formalism. Pairing for nucleons is also discussed in the constant BCS approximation [47].

### 2.2.1 Skyrme Formalism

For Hartree-Fock (HF) description [36, 48, 49] of ground state configuration, the many body wave function  $\psi$  of a nucleus of mass number  $A$  can be given by the Slater determinant as,

$$\psi(x_1, x_2, \dots, x_A) = \frac{1}{\sqrt{A!}} \begin{vmatrix} \phi_1(x_1) & \phi_1(x_2) & \phi_1(x_3) & \cdots & \phi_1(x_A) \\ \phi_2(x_1) & \phi_2(x_2) & \cdots & \cdots & \cdots \\ \dots & & & & \\ \phi_A(x_1) & \phi_A(x_2) & \phi_A(x_3) & \cdots & \phi_A(x_A) \end{vmatrix}, \quad (2.1)$$

where  $\phi_i$  (with  $i = 1, 2, \dots, A$ ) denotes the occupied single particle states and  $x$ 's run over  $\mathbf{r}$ , spin  $\sigma$  and isospin  $q$  ( $= p$  for proton and  $n$  for neutron). Then the expectation value of

the total energy of system can be written as,

$$\begin{aligned}
E &= \langle \psi | (T + V) | \psi \rangle \\
&= \sum_i \langle \phi_i | \left| \frac{p^2}{2m} \right| \phi_i \rangle + \frac{1}{2} \sum_{ij} \langle \phi_i \phi_j | \bar{v}_{12} | \phi_i \phi_j \rangle + \frac{1}{6} \sum_{ijk} \langle \phi_i \phi_j \phi_k | \bar{v}_{123} | \phi_i \phi_j \phi_k \rangle \\
&= \int \mathcal{H}(\mathbf{r}) d^3\mathbf{r}.
\end{aligned} \tag{2.2}$$

Here,  $\bar{v}$ 's denote the two-body and three body antisymmetrized matrix elements. For Skyrme interaction the Hamiltonian density  $\mathcal{H}$  is algebraic function of nucleon densities  $\rho_q$ , kinetic energy densities  $\tau_q$  and spin densities  $\mathbf{J}_q$ . With some phenomenological corrections [36, 49] over the actual interaction given by Skyrme [43, 44], the interaction part of the Hamiltonian density can be given by,

$$\begin{aligned}
V(\mathbf{r}_1, \mathbf{r}_2) &= t_0(1 + x_0 P_\sigma) \delta(\mathbf{r}) + \frac{1}{2} t_1(1 + x_1 P_\sigma) \left[ \delta(\mathbf{r}) \mathbf{k}'^2 + \mathbf{k}^2 \delta(\mathbf{r}) \right] + t_2(1 + x_2 P_\sigma) \mathbf{k}' \cdot \delta(\mathbf{r}) \mathbf{k} \\
&\quad + t_3 \rho^\alpha (1 + x_3 P_\sigma) \delta(\mathbf{r}) + i W_0 \boldsymbol{\sigma} \cdot [\mathbf{k}' \times \delta(\mathbf{r}) \mathbf{k}],
\end{aligned} \tag{2.3}$$

where,  $\mathbf{r} = \mathbf{r}_1 - \mathbf{r}_2$ ,  $\mathbf{k} = \frac{\nabla_1 - \nabla_2}{2i}$ ,  $\mathbf{k}'$  is complex conjugate of  $\mathbf{k}$  acting on the left,  $\boldsymbol{\sigma} = \boldsymbol{\sigma}_1 + \boldsymbol{\sigma}_2$ , and the spin exchange operator  $P_\sigma = \frac{1}{2}(1 + \boldsymbol{\sigma}_1 \cdot \boldsymbol{\sigma}_2)$ . Consequently following Eq. (2.2) the Energy density functional (EDF) or the Hamiltonian density is given by,

$$\mathcal{H} = \mathcal{K} + \mathcal{H}_0 + \mathcal{H}_3 + \mathcal{H}_{\text{eff}} + \mathcal{H}_{\text{fin}} + \mathcal{H}_{\text{SO}} + \mathcal{H}_{\text{sg}} + \mathcal{H}_{\text{Coul}} + \mathcal{H}_{\text{pair}}. \tag{2.4}$$

Here, kinetic energy is denoted by,  $\mathcal{K} = \frac{\hbar^2}{2m} \tau$ , Coulomb energy for the protons and the pairing energy are given by  $\mathcal{H}_{\text{Coul}}$  and  $\mathcal{H}_{\text{pair}}$ , respectively. The rest of the terms are coming from the Skyrme interaction given in Eq. (2.3), which are written in terms of different

densities as,

$$\begin{aligned}
\mathcal{H}_0(\mathbf{r}) &= \frac{1}{4}t_0 [(2+x_0)\rho^2 - (2x_0+1)(\rho_p^2 + \rho_n^2)], \\
\mathcal{H}_3(\mathbf{r}) &= \frac{1}{24}t_3\rho^\alpha [(2+x_3)\rho^2 - (2x_3+1)(\rho_p^2 + \rho_n^2)], \\
\mathcal{H}_{\text{eff}}(\mathbf{r}) &= \frac{1}{8}[t_1(2+x_1) + t_2(2+x_2)]\tau\rho + \frac{1}{8}[t_2(2x_2+1) - t_1(2x_1+1)](\tau_p\rho_p + \tau_n\rho_n), \\
\mathcal{H}_{\text{fin}}(\mathbf{r}) &= \frac{1}{32}[3t_1(2+x_1) - t_2(2+x_2)](\nabla\rho)^2, \\
&\quad - \frac{1}{32}[3t_1(2x_1+1) + t_2(2x_2+1)][(\nabla\rho_p)^2 + (\nabla\rho_n)^2], \\
\mathcal{H}_{\text{SO}}(\mathbf{r}) &= \frac{1}{2}W_0[\mathbf{J}\cdot\nabla\rho + \mathbf{J}\cdot\nabla\rho_p + \mathbf{J}\cdot\nabla\rho_n], \\
\mathcal{H}_{\text{sg}}(\mathbf{r}) &= \frac{1}{16}(t_1 - t_2)[\mathbf{J}_p^2 + \mathbf{J}_n^2] - \frac{1}{16}(t_1x_1 + t_2x_2)\mathbf{J}^2.
\end{aligned} \tag{2.5}$$

The Coulomb energy for the protons is given by,

$$\mathcal{H}_{\text{Coul}}(\mathbf{r}) = \frac{1}{2}e^2\rho_p(\mathbf{r}) \int d^3\mathbf{r}' \frac{\rho_p(\mathbf{r}')}{|\mathbf{r}-\mathbf{r}'|} - \frac{3}{4}e^2\rho_p(\mathbf{r}) \left(\frac{3\rho_p(\mathbf{r})}{\pi}\right)^{1/3}. \tag{2.6}$$

In Eqs. (2.5) and (2.6), the various densities are given by,

$$\begin{aligned}
\rho_q(\mathbf{r}) &= \sum_{i,\sigma} |\phi_i(\mathbf{r}, \sigma, q)|^2, \\
\tau_q(\mathbf{r}) &= \sum_{i,\sigma} |\nabla\phi_i(\mathbf{r}, \sigma, q)|^2, \\
\mathbf{J}_q(\mathbf{r}) &= -i \sum_{i,\sigma,\sigma'} \phi_i^*(\mathbf{r}, \sigma, q) [\nabla\phi_i(\mathbf{r}, \sigma', q) \times \langle\sigma|\sigma'\rangle].
\end{aligned} \tag{2.7}$$

The total densities  $\rho$ ,  $\tau$  and  $\mathbf{J}$  are calculated by summing over  $q = n$  and  $p$ .

Now the HF equations are obtained by writing E stationary with respect to variation of

individual single particle states  $\phi_i$  with the added condition that  $\phi_i$ 's are normalized,

$$\frac{\delta}{\delta\phi_i} \left( E - \sum_i \epsilon_i \int |\phi_i(\mathbf{r})|^2 d^3r \right) = 0. \quad (2.8)$$

An equivalent description can be obtained if the variation is performed with respect to the densities  $\tau_q$ ,  $\rho_q$  and  $\mathbf{J}_q$  instead of  $\phi_i$ . Then the variational equation takes the form

$$\left[ -\nabla \frac{\hbar^2}{2m_q^*(\mathbf{r})} \cdot \nabla + U_q(\mathbf{r}) - i\mathbf{W}_q(\mathbf{r}) \cdot (\nabla \times \boldsymbol{\sigma}) \right] \phi_i(\mathbf{r}, q) = \epsilon_i \phi_i(\mathbf{r}, q). \quad (2.9)$$

Eq. (2.9) represents the Schrödinger equation for the single particle states  $\phi_i$ . The different coefficients  $\frac{\hbar^2}{2m^*}$ ,  $U_q$  and  $\mathbf{W}_q$  determine the effective mass, central potential and the spin-orbit potential, respectively. The effective mass  $m_q^*$  is given by,

$$\begin{aligned} \frac{\delta\mathcal{H}}{\delta\tau_q(\mathbf{r})} = \frac{\hbar^2}{2m_q^*(\mathbf{r})} &= \frac{\hbar^2}{2m} + \frac{1}{8} [t_1(2+x_1) + t_2(2+x_2)] \rho(\mathbf{r}) \\ &+ \frac{1}{8} [t_2(2x_2+1) - t_1(2x_1+1)] \rho_q(\mathbf{r}). \end{aligned} \quad (2.10)$$

The central, spin-orbit and Coulomb potentials are given by,

$$\begin{aligned} \frac{\delta\mathcal{H}}{\delta\rho_q(\mathbf{r})} = U_q(\mathbf{r}) &= \frac{1}{2}t_0 [(2+x_0)\rho(\mathbf{r}) - (1+2x_0)\rho_q(\mathbf{r})] \\ &+ \frac{1}{24}t_3 \{ (2+x_3)(2+\alpha)\rho^{\alpha+1}(\mathbf{r}) \\ &\quad - (2x_3+1) [2\rho^\alpha(\mathbf{r})\rho_q(\mathbf{r}) + \alpha\rho^{\alpha-1}(\mathbf{r}) (\rho_p^2(\mathbf{r}) + \rho_n^2(\mathbf{r}))] \} \\ &+ \frac{1}{8} [t_1(2+x_1) + t_2(2+x_2)] \tau(\mathbf{r}) + \frac{1}{8} [t_2(2x_2+1) - t_1(2x_1+1)] \tau_q(\mathbf{r}) \\ &+ \frac{1}{16} [t_2(2+x_2) - 3t_1(2+x_1)] \nabla^2\rho(\mathbf{r}) \\ &\quad + \frac{1}{16} [3t_1(2x_1+1) + t_2(2x_2+1)] \nabla^2\rho_q(\mathbf{r}) \end{aligned}$$

$$- \frac{1}{2}W_0 (\nabla \cdot \mathbf{J}(\mathbf{r}) + \nabla \cdot \mathbf{J}_q(\mathbf{r})) + \delta_{q,p}V_{\text{Coul}}(\mathbf{r}), \quad (2.11)$$

$$\frac{\delta\mathcal{H}}{\delta\mathbf{J}_q(\mathbf{r})} = \mathbf{W}_q(\mathbf{r}) = \frac{1}{2}W_0 (\nabla\rho(\mathbf{r}) + \nabla\rho_q(\mathbf{r})) + \frac{1}{8}(t_1 - t_2)\mathbf{J}_q(\mathbf{r}) - \frac{1}{8}(t_1x_1 + t_2x_2)\mathbf{J}(\mathbf{r}), \quad (2.12)$$

$$V_{\text{Coul}}(\mathbf{r}) = \frac{1}{2}e^2 \int d^3\mathbf{r}' \frac{\rho_p(\mathbf{r}')}{|\mathbf{r} - \mathbf{r}'|} - \frac{3}{4}e^2 \left( \frac{3\rho_p(\mathbf{r})}{\pi} \right)^{1/3}. \quad (2.13)$$

For doubly closed shell nuclei the HF equations can be derived using,

$$\begin{aligned} \phi_i(\mathbf{r}, \sigma, \boldsymbol{\tau}) &= \frac{R_\alpha(r)}{r} \mathcal{Y}_{ljm}(\hat{r}, \sigma) \chi_q(\boldsymbol{\tau}), \\ \mathcal{Y}_{ljm}(\hat{r}, \sigma) &= \sum_{m_l m_s} \langle l \frac{1}{2} m_l m_s | j m \rangle Y_{lm_l}(\hat{r}) \chi_{m_s}(\sigma), \end{aligned} \quad (2.14)$$

where,  $R_\alpha(r)$  is the radial part of the wave-function and  $\mathcal{Y}_{ljm}$  is the spherical harmonics representing the spin and angular part of the wave-function. In Eq. (2.14)  $i \equiv (q, n, l, j, m)$  and  $\alpha \equiv (n, l, j)$  convention was used, where,  $q$  is the charge, the principal quantum number  $n$ , orbital angular momentum  $l$ , total single-particle angular momentum  $j$  and magnetic quantum number  $m$ . Consequently the densities in Eq. (2.7) get modified as [48],

$$\begin{aligned} \rho_q(r) &= \frac{1}{4\pi r^2} \sum_{\alpha} (2j_{\alpha} + 1) R_{\alpha}^2(r) \chi_q^2, \\ \tau_q(r) &= \frac{1}{4\pi} \sum_{\alpha} (2j_{\alpha} + 1) \left[ \left( \frac{d\varphi_{\alpha}}{dr} \right)^2 + \frac{l_{\alpha}(l_{\alpha} + 1)}{r^2} \varphi_{\alpha}^2 \right] \chi_q^2, \\ \mathbf{J}_q(\mathbf{r}) &= \frac{\mathbf{r}}{r} J_q(r), \quad \text{with} \\ J_q(r) &= \frac{1}{4\pi r^3} \sum_{\alpha} (2j_{\alpha} + 1) \left[ j_{\alpha}(j_{\alpha} + 1) - l_{\alpha}(l_{\alpha} + 1) - \frac{3}{4} \right] R_{\alpha}^2(r) \chi_q^2, \end{aligned} \quad (2.15)$$

where,  $\varphi_{\alpha} = \frac{R_{\alpha}(r)}{r}$ . Due to the symmetry in  $\mathbf{J}_q$  in Eq. (2.15), expression of  $\mathbf{W}_q$  in Eq.

(2.9) gets modified as,

$$\begin{aligned}\mathbf{W}_q(\mathbf{r}) &= \frac{1}{r}W_q(r)\vec{l} \cdot \boldsymbol{\sigma} \quad \text{with} \\ W_q(r) &= \frac{1}{2}W_0\frac{d}{dr}(\rho + \rho_q) + \frac{1}{8}(t_1 - t_2)J_q(r) - \frac{1}{8}(t_1x_1 + t_2x_2)J(r).\end{aligned}\quad (2.16)$$

Consequently, for closed shell spherical nuclei Eq. (2.9) takes the form,

$$-\frac{\hbar^2}{2m_q^*}\nabla^2\phi_i - \left(\nabla\frac{\hbar^2}{2m_q^*}\right) \cdot \nabla\phi_i + \left(U_q + \frac{1}{r}W_q\vec{l} \cdot \boldsymbol{\sigma}\right)\phi_i = \epsilon_i\phi_i.\quad (2.17)$$

Using the expressions for gradient and Laplacian operators in spherical coordinate as,

$$\begin{aligned}\nabla^2 &\equiv \frac{1}{r}\frac{\partial^2}{\partial r^2}r - \frac{\vec{l}^2}{r^2}, \\ \nabla\frac{\hbar^2}{2m_q^*} &= \frac{\mathbf{r}}{r}\frac{d}{dr}\frac{\hbar^2}{2m_q^*},\end{aligned}\quad (2.18)$$

one can write the coupled Schrödinger equation for radial part of the wave-function  $R_\alpha(r)$

as,

$$\begin{aligned}&\frac{\hbar^2}{2m_q^*}\left[-\frac{d^2R_\alpha(r)}{dr^2} + \frac{l_\alpha(l_\alpha + 1)}{r^2}R_\alpha(r)\right] - \frac{d}{dr}\left(\frac{\hbar^2}{2m_q^*}\right)\frac{dR_\alpha(r)}{dr} \\ &+ \left\{U_q(r) + \frac{1}{r}\frac{d}{dr}\left(\frac{\hbar^2}{2m_q^*}\right) + \left[j_\alpha(j_\alpha + 1) - l_\alpha(l_\alpha + 1) - \frac{3}{4}\right] \times \frac{1}{r}W_q(r)\right\}R_\alpha(r) = \epsilon_\alpha R_\alpha(r)\end{aligned}\quad (2.19)$$

The solutions for  $R_\alpha$  in Eq. (2.19) are obtained iteratively by solving self-consistently the Eqs. (2.10), (2.11) and (2.16). First a guess solution for the unknown  $R_\alpha$  is taken as Harmonic-oscillator or Wood-Saxon wave functions along with a particular occupation probability distributions of the single particle levels. Inserting them in Eq. (2.15) ex-

pression for densities are obtained. Consequently, the expressions for  $\frac{\hbar^2}{2m_q^*}$ ,  $U_q$  and  $W_q$  are obtained from Eqs. (2.10), (2.11) and (2.16) respectively. Putting those values in Eq. (2.19) the next guess for  $R_\alpha$  is obtained. In case of presence of a pairing interaction, the occupation probability distribution of the single particle levels are calculated satisfying the number of particle for a nucleus. This process iterated until a consistent solution is obtained.

## 2.2.2 Relativistic Mean Field formalism

The effective Lagrangian for the relativistic mean field (RMF) model employed in the present thesis work is similar to that of the FSU one [50]. The system contains the nucleonic field  $\psi$  and three different types of mesons, which mediate the force, namely, isoscalar-scalar  $\sigma$ , isoscalar-vector  $\omega$  and isovector-vector  $\rho$  (field denoted by  $\mathbf{R}_\mu$ ) [23, 51–53]. The protons also interact through an electromagnetic field  $A^\mu$ . The total Lagrangian can be decomposed into different components as,

$$\mathcal{L} = \int d^3\mathbf{r} \left\{ \mathcal{L}_{\text{BM}} + \mathcal{L}_\sigma + \mathcal{L}_\omega + \mathcal{L}_\rho + \mathcal{L}_{\omega\rho} + \mathcal{L}_{\text{em}} \right\}. \quad (2.20)$$

The baryonic-mesonic Lagrangian containing the Yukawa couplings between the nucleon and the mesons is given by,

$$\mathcal{L}_{\text{BM}} = \bar{\psi} \left[ i\gamma^\mu \partial_\mu - (M - g_\sigma \sigma) - \gamma^\mu \left( g_\omega \omega_\mu + \frac{1}{2} g_\rho \boldsymbol{\tau} \cdot \mathbf{R}_\mu \right) \right] \psi. \quad (2.21)$$

The parameters  $g_\sigma$ ,  $g_\omega$  and  $g_\rho$  describe the strength of the couplings of  $\psi$  with  $\sigma$ ,  $\omega$  and  $\rho$  mesons respectively.  $M$  is the free nucleon mass and the Dirac effective mass is denoted by  $M_{\text{Dir}}^* = (M - g_\sigma \sigma)$ . The Lagrangian for the mesons including the self-interaction terms



are given by,

$$\begin{aligned}
\mathcal{L}_\sigma &= \frac{1}{2} (\partial_\mu \sigma \partial^\mu \sigma - m_\sigma^2 \sigma^2) - \frac{\kappa_3}{3! M} g_\sigma m_\sigma^2 \sigma^3 - \frac{\kappa_4}{4! M^2} g_\sigma^2 m_\sigma^2 \sigma^4, \\
\mathcal{L}_\omega &= -\frac{1}{4} \omega_{\mu\nu} \omega^{\mu\nu} + \frac{1}{2} m_\omega^2 \omega_\mu \omega^\mu + \frac{1}{4!} \zeta_0 g_\omega^2 (\omega_\mu \omega^\mu)^2, \\
\mathcal{L}_\rho &= -\frac{1}{4} \mathbf{R}_{\mu\nu} \mathbf{R}^{\mu\nu} + \frac{1}{2} m_\rho^2 \mathbf{R}_\mu \mathbf{R}^\mu.
\end{aligned} \tag{2.22}$$

Field tensors for  $\omega$  and  $\rho$  mesons are given by,  $\omega_{\mu\nu} = \partial_\mu \omega_\nu - \partial_\nu \omega_\mu$  and  $\mathbf{R}_{\mu\nu} = \partial_\mu \mathbf{R}_\nu - \partial_\nu \mathbf{R}_\mu$ . The cross-coupling between the  $\omega$  and the  $\rho$  mesons is given by,

$$\mathcal{L}_{\omega\rho} = \frac{\eta_{2\rho}}{4M^2} g_\omega^2 m_\rho^2 \omega_\mu \omega^\mu \mathbf{R}_\nu \mathbf{R}^\nu. \tag{2.23}$$

The electromagnetic interaction between the protons is given by,

$$\mathcal{L}_{\text{em}} = -\frac{1}{4} F_{\mu\nu} F^{\mu\nu} - e \bar{\psi} \gamma^\mu \frac{1 + \tau_0}{2} A_\mu \psi, \tag{2.24}$$

where  $F_{\mu\nu} = \partial_\mu A_\nu - \partial_\nu A_\mu$ ,  $e$  is the charge of proton and  $\tau_0 = 1$  for protons and  $= -1$  for neutrons.

In the covariant formalism the Euler-Lagrange equation for a field  $\varphi$  is given by,

$$\partial_\mu \left( \frac{\partial \mathcal{L}}{\partial (\partial_\mu \varphi)} \right) = \frac{\partial \mathcal{L}}{\partial \varphi}. \tag{2.25}$$

Immediately the equation of motion of the single particle wave-functions  $\phi$  for the nucleons is given by the Dirac equation as,

$$i \frac{\partial}{\partial t} \phi_\alpha = \gamma^0 \left[ -i \boldsymbol{\gamma} \cdot \boldsymbol{\nabla} + \gamma^\mu \left( g_\omega \omega_\mu + \frac{1}{2} g_\rho \tau_i \cdot R_{i,\mu} + e \frac{1 + \tau_0}{2} A_\mu \right) + (M - g_\sigma \sigma) \right] \phi_\alpha. \tag{2.26}$$

Here the nucleon field operator  $\hat{\psi}$  is already expanded over the single particle states  $\phi$  by the relation,  $\hat{\psi} = \sum_{\alpha} \phi_{\alpha} a_{\alpha}$ . The quantity  $|a_{\alpha}|^2$  determines the probability of finding a particle in single particle state  $\phi_{\alpha}$ . Similarly, Euler-Lagrange equations for the mesons and the electromagnetic field  $A^{\mu}$  are given by,

$$\begin{aligned}
\frac{\partial^2}{\partial t^2} \sigma &= (\Delta - m_{\sigma}^2) \sigma + g_{\sigma} \rho_s - \frac{\kappa_3}{2M} g_{\sigma} m_{\sigma}^2 \sigma^2 - \frac{\kappa_4}{3! M^2} g_{\sigma}^2 m_{\sigma}^2 \sigma^3, \\
\frac{\partial^2}{\partial t^2} \omega_{\mu} &= (\Delta - m_{\omega}^2) \omega_{\mu} + g_{\omega} \rho_{\mu} - \frac{1}{3!} \zeta_0 g_{\omega}^2 \omega_{\nu} \omega^{\nu} \omega_{\mu} - \frac{\eta_{2\rho}}{2M^2} g_{\omega}^2 m_{\rho}^2 R_{i,\nu} R_i^{\nu} \omega_{\mu}, \\
\frac{\partial^2}{\partial t^2} R_{i,\mu} &= (\Delta - m_{\rho}^2) R_{i,\mu} + \frac{1}{2} g_{\rho} \rho_{i,\mu} - \frac{\eta_{2\rho}}{2M^2} g_{\omega}^2 m_{\rho}^2 \omega_{\nu} \omega^{\nu} R_{i,\mu}, \\
\frac{\partial^2}{\partial t^2} A_{\mu} &= \Delta A_{\mu} + e \rho_{p,\mu},
\end{aligned} \tag{2.27}$$

where the different densities are given by,

$$\begin{aligned}
\rho_s &= \sum_{\alpha=-\infty}^{\infty} w_{\alpha} \bar{\phi}_{\alpha} \phi_{\alpha}, \\
\rho_{\mu} &= \sum_{\alpha=-\infty}^{\infty} w_{\alpha} \bar{\phi}_{\alpha} \gamma_{\mu} \phi_{\alpha}, \\
\rho_{i,\mu} &= \sum_{\alpha=-\infty}^{\infty} w_{\alpha} \bar{\phi}_{\alpha} \tau_i \gamma_{\mu} \phi_{\alpha}, \\
\rho_{p,\mu} &= \sum_{\alpha=-\infty}^{\infty} w_{\alpha} \bar{\phi}_{\alpha} \frac{1 + \tau_0}{2} \gamma_{\mu} \phi_{\alpha},
\end{aligned} \tag{2.28}$$

where,  $w_{\alpha} = 1$  for levels below Fermi surface including both the positive and negative energy states and  $w_{\alpha} = 0$  for levels above Fermi surface.

For ground state properties of finite nuclei, only the static solutions are relevant. Due to this reason all the mesonic fields are time-independent and the nucleon wave-function is determined by the single particle energies  $\epsilon_{\alpha}$ . Moreover,  $\psi$  is even under time reversal, meaning the vector currents e.g.  $\rho_{\mu}$  or  $\rho_{i,\mu}$  only survive by their  $\mu = 0$  components.

Further due to isospin symmetry, only the component  $\rho_{0,0}$  survives in the current  $\rho_{i,0}$ . So the equation of motion for the nucleons, mesons and the electromagnetic field take the form,

$$\begin{aligned}
\epsilon_\alpha \phi_\alpha &= \gamma^0 \left[ -i\boldsymbol{\gamma} \cdot \boldsymbol{\nabla} + \gamma^0 \left( g_\omega \omega_0 + \frac{1}{2} g_\rho \boldsymbol{\tau}_0 \cdot \mathbf{R}_{0,0} + e \frac{1 + \tau_0}{2} A_0 \right) + (M - g_\sigma \sigma) \right] \phi_\alpha, \\
(-\Delta + m_\sigma^2) \sigma &= g_\sigma \rho_s - \frac{\kappa_3}{2M} g_\sigma m_\sigma^2 \sigma^2 - \frac{\kappa_4}{3! M^2} g_\sigma^2 m_\sigma^2 \sigma^3, \\
(-\Delta + m_\omega^2) \omega_0 &= g_\omega \rho_0 - \frac{1}{3!} \zeta_0 g_\omega^2 \omega_0^3 - \frac{\eta_{2\rho}}{2M^2} g_\omega^2 m_\rho^2 R_{0,0}^2 \omega_0, \\
(-\Delta + m_\rho^2) R_{0,0} &= \frac{1}{2} g_\rho \rho_{0,0} - \frac{\eta_{2\rho}}{2M^2} g_\omega^2 m_\rho^2 \omega_0^2 R_{0,0}, \\
-\Delta A_0 &= e \rho_{p,0}.
\end{aligned} \tag{2.29}$$

The sum for all the densities given in Eq. (2.28) still runs over both the positive and negative energy spectrum of the Dirac equation. The full summation is too difficult to handle numerically. In "No-Sea" approximation the sum runs over few positive energy bound state or so to say the number of shell model states ( $= \Omega$ ) included in the numerical calculation, where,

$$\sum_{\alpha=1}^{\Omega} w_\alpha = \begin{cases} N \\ Z \end{cases} . \tag{2.30}$$

Depending on the neutron or proton occupation probability, the summation gives the total number of particles i.e.  $N$  for neutrons and  $Z$  for protons. In these set of approximations the different densities take the form,

$$\rho_s = \sum_{\alpha=1}^{\Omega} w_\alpha \bar{\phi}_\alpha \phi_\alpha,$$

$$\begin{aligned}
\rho_0 &= \sum_{\alpha=1}^{\Omega} w_{\alpha} \bar{\phi}_{\alpha} \gamma_0 \phi_{\alpha}, \\
\rho_{0,0} &= \sum_{\alpha=1}^{\Omega} w_{\alpha} \bar{\phi}_{\alpha} \tau_i \gamma_0 \phi_{\alpha}, \\
\rho_{p,0} &= \sum_{\alpha=1}^{\Omega} w_{\alpha} \bar{\phi}_{\alpha} \frac{1 + \tau_0}{2} \gamma_0 \phi_{\alpha}.
\end{aligned} \tag{2.31}$$

In the covariant formalism the stress-energy tensor  $T^{\mu\nu}$  for a field  $\varphi$  is given by,

$$T^{\mu\nu} = \frac{\partial \mathcal{L}}{\partial (\partial_{\mu} \varphi)} \partial^{\nu} \varphi - g^{\mu\nu} \mathcal{L}, \tag{2.32}$$

where  $g^{\mu\nu}$  are the components of metric tensor given by  $g^{\mu\nu} = \text{Diag}[1 \ -1 \ -1 \ -1]$ . The component  $T^{00}$  gives the energy of the system. So, the mean-field energy is then given by,

$$\begin{aligned}
E &= \int d^3r \left\{ \sum_{\alpha} w_{\alpha} \bar{\phi}_{\alpha} \left[ -i\boldsymbol{\gamma} \cdot \boldsymbol{\nabla} + \gamma_0 \left( g_{\omega} \omega_0 + \frac{1}{2} g_{\rho} \tau_0 \cdot R_{0,0} + e \frac{1 + \tau_0}{2} A_0 \right) + (M - g_{\sigma} \sigma) \right] \phi_{\alpha} \right. \\
&\quad + \frac{1}{2} [(\boldsymbol{\nabla} \sigma)^2 + m_{\sigma}^2 \sigma^2] + \frac{\kappa_3}{3!M} g_{\sigma} m_{\sigma}^2 \sigma^3 + \frac{\kappa_4}{4!M^2} g_{\sigma}^2 m_{\sigma}^2 \sigma^4 \\
&\quad \left. - \frac{1}{2} [(\boldsymbol{\nabla} \omega_0)^2 + m_{\omega}^2 \omega_0^2 + (\boldsymbol{\nabla} R_{0,0})^2 + m_{\rho}^2 R_{0,0}^2 + (\boldsymbol{\nabla} A_0)^2] - \frac{1}{4!} \zeta_0 g_{\omega}^2 \omega_0^4 - \frac{\eta_{2\rho}}{4M^2} g_{\omega}^2 m_{\rho}^2 \omega_0^2 R_{0,0}^2 \right\} \\
&= \sum_{\alpha} w_{\alpha} \epsilon_{\alpha} + \int d^3r \frac{1}{2} \left[ g_{\sigma} \rho_s \sigma - \frac{\kappa_3}{6M} g_{\sigma} m_{\sigma}^2 \sigma^3 - \frac{\kappa_4}{6M^2} g_{\sigma}^2 m_{\sigma}^2 \sigma^4 \right. \\
&\quad \left. - g_{\omega} \rho_0 \omega_0 + \frac{1}{6} \zeta_0 g_{\omega}^2 \omega_0^4 - \frac{1}{2} g_{\rho} \rho_{0,0} R_{0,0} + \frac{\eta_{2\rho}}{2M^2} g_{\omega}^2 m_{\rho}^2 \omega_0^2 R_{0,0}^2 - e \rho_{p,0} A_0 \right].
\end{aligned} \tag{2.33}$$

For spherically symmetric mean-fields i.e.  $\sigma = \sigma(|r|)$ ,  $\omega_0 = \omega_0(|r|)$  and so on the two component nucleon wave-function can be expressed as,

$$\phi_{\alpha} = \begin{pmatrix} i \frac{G_{\alpha}(r)}{r} \mathcal{Y}_{j_{\alpha} l_{\alpha} m_{\alpha}} \\ \frac{F_{\alpha}(r)}{r} \frac{\boldsymbol{\sigma} \cdot \mathbf{p}}{r} \mathcal{Y}_{j_{\alpha} l_{\alpha} m_{\alpha}} \end{pmatrix}, \tag{2.34}$$

where  $\mathcal{Y}_{jlm}$  denotes the spinor spherical harmonics and  $G_\alpha$  and  $F_\alpha$  are the radial parts of the two component nuclear wave-function (similar to Eq. (2.14)).  $G_\alpha$  and  $F_\alpha$  are further subject to normalization,

$$\int_0^\infty dr \{ |G_\alpha|^2 + |F_\alpha|^2 \} = 1. \quad (2.35)$$

Here, both  $G_\alpha$  and  $F_\alpha$  can be considered as real. Then the densities in Eq. (2.31) take the form,

$$\begin{aligned} \rho_s &= \frac{1}{4\pi r^2} \sum_\alpha w_\alpha (2j_\alpha + 1) (G_\alpha^2 - F_\alpha^2), \\ \rho_0 &= \frac{1}{4\pi r^2} \sum_\alpha w_\alpha (2j_\alpha + 1) (G_\alpha^2 + F_\alpha^2), \\ \rho_{0,0} &= \frac{1}{4\pi r^2} \sum_\alpha w_\alpha (2j_\alpha + 1) \tau_{0\alpha} (G_\alpha^2 + F_\alpha^2), \\ \rho_{p,0} &= \frac{1}{2} (\rho_0 + \rho_{0,0}). \end{aligned} \quad (2.36)$$

With these form of the densities, the Euler-Lagrange equations for the mesons and the electromagnetic field look like Laplace equations,

$$\begin{aligned} \left( -\frac{d^2}{dr^2} + m_\sigma^2 \right) \sigma &= \left\{ g_\sigma \rho_s - \frac{\kappa_3}{2M} g_\sigma m_\sigma^2 \sigma^2 - \frac{\kappa_4}{3! M^2} g_\sigma^2 m_\sigma^2 \sigma^3 \right\}, \\ \left( -\frac{d^2}{dr^2} + m_\omega^2 \right) \omega_0 &= \left\{ g_\omega \rho_0 - \frac{1}{3!} \zeta_0 g_\omega^2 \omega_0^3 - \frac{\eta_{2\rho}}{2M^2} g_\omega^2 m_\rho^2 R_{0,0}^2 \omega_0 \right\}, \\ \left( -\frac{d^2}{dr^2} + m_\rho^2 \right) R_{0,0} &= \left\{ \frac{1}{2} g_\rho \rho_{0,0} - \frac{\eta_{2\rho}}{2M^2} g_\omega^2 m_\rho^2 \omega_0^2 R_{0,0} \right\}, \\ -\frac{d^2}{dr^2} A_0 &= e \rho_{p,0}. \end{aligned} \quad (2.37)$$

Similarly, the coupled Dirac equation for the radial wave-functions are given by,

$$\begin{aligned}\epsilon_\alpha G_\alpha &= \left(-\frac{d}{dr} + \frac{a_\alpha}{r}\right) F_\alpha + \left(M - g_\sigma \sigma + g_\omega \omega_0 + \frac{1}{2} g_\rho \tau_{0\alpha} \cdot R_{0,0} + e \frac{1 + \tau_{0\alpha}}{2} A_0\right) G_\alpha, \\ \epsilon_\alpha F_\alpha &= \left(\frac{d}{dr} + \frac{a_\alpha}{r}\right) G_\alpha - \left(M - g_\sigma \sigma - g_\omega \omega_0 - \frac{1}{2} g_\rho \tau_{0\alpha} \cdot R_{0,0} - e \frac{1 + \tau_{0\alpha}}{2} A_0\right) F_\alpha,\end{aligned}\tag{2.38}$$

where

$$a_\alpha = \begin{cases} -(j_\alpha + \frac{1}{2}) & \text{for } j = l + \frac{1}{2} \\ +(j_\alpha + \frac{1}{2}) & \text{for } j = l - \frac{1}{2} \end{cases} .\tag{2.39}$$

One can eliminate  $F_\alpha$  in Eq. (2.38) and expression for  $G_\alpha$  can be obtained as,

$$\begin{aligned}\epsilon_\alpha G_\alpha &= -\left(\frac{d}{dr} - \frac{a_\alpha}{r}\right) M_{\text{eff}}^{-1} \left(\frac{d}{dr} + \frac{a_\alpha}{r}\right) G_\alpha + U_{\text{eff}} G_\alpha, \\ \text{with, } M_{\text{eff}} &= \epsilon_\alpha + M - g_\sigma \sigma - g_\omega \omega_0 - \frac{1}{2} g_\rho \tau_{0\alpha} \cdot R_{0,0} - e \frac{1 + \tau_{0\alpha}}{2} A_0, \\ U_{\text{eff}} &= M - g_\sigma \sigma + g_\omega \omega_0 + \frac{1}{2} g_\rho \tau_{0\alpha} \cdot R_{0,0} + e \frac{1 + \tau_{0\alpha}}{2} A_0.\end{aligned}\tag{2.40}$$

Eq. (2.40) looks very similar to Eq. (2.19).  $F_\alpha$  in Eq. (2.38) is then reconstructed by,

$$F_\alpha = M_{\text{eff}}^{-1} \left(\frac{d}{dr} + \frac{a_\alpha}{r}\right) G_\alpha.\tag{2.41}$$

The solution for  $F_\alpha$  and  $G_\alpha$  can be obtained by the following way. First a guess solution, typically a Wood-Saxon or Harmonic oscillator function is taken for  $F_\alpha$  and  $G_\alpha$  with a corresponding set of  $w_\alpha$ 's. A guess solution for  $\sigma$  field is taken as a Fermi function. Now, the different densities are calculated accordingly following Eq. (2.36). Upon that, the solu-

tions for other mesons and electromagnetic field are found from Eq. (2.37). Consequently,  $M_{\text{eff}}$  and  $U_{\text{eff}}$  are calculated from Eq. (2.40). Then new solution of  $G_\alpha$  is found by using Eq. (2.40) subject to the normalization,

$$\int dr \{G_\alpha G_\beta + F_\alpha F_\beta\} = \delta_{\alpha\beta}, \quad (2.42)$$

where,  $F_\alpha$  is obtained by using Eq. (2.41). With these new  $G_\alpha$  and  $F_\alpha$ , new set of  $\epsilon_\alpha$ 's are obtained by solving the coupled Dirac equation as,

$$\epsilon_\alpha = \int_0^\infty dr \left\{ F_\alpha \left( \frac{d}{dr} + \frac{a_\alpha}{r} \right) G_\alpha + G_\alpha \left( -\frac{d}{dr} + \frac{a_\alpha}{r} \right) F_\alpha + G_\alpha U_{\text{eff}} G_\alpha - F_\alpha (M_{\text{eff}} - \epsilon_\alpha) F_\alpha \right\}. \quad (2.43)$$

In the right hand side of Eq. (2.43) old set of  $\epsilon_\alpha$ 's are used. In presence of pairing interaction, the  $w_\alpha$ 's calculated now using Eq. (2.30). This whole process is repeated until a self-consistent solution is obtained.

### 2.2.3 Pairing in BCS approximation

Pairing plays a very important role in the occupation probability of the single particle levels near the Fermi surface. Well below the Fermi surface the occupation probability of a single-particle state is unity and it becomes nearly zero well above the Fermi surface. However, near the Fermi surface it becomes a fractional number lying between zero and unity. It can be understood by means of a coupling between a single particle state with its time-reversed partner. In this thesis work pairing for finite nuclei is treated in BCS approximation which was originally given by Bardeen, Cooper, and Schrieffer [54, 55] for electronic systems. A more general version of the BCS pairing can be applied using Lipkin-Nogami pairing

model [56, 57]. However, here pairing is restricted to a constant gap model.

At second quantization Hamiltonian of nuclear system can be written as,

$$\hat{H} = \sum_{\alpha} \epsilon_{\alpha}^0 \hat{a}_{\alpha}^{\dagger} \hat{a}_{\alpha} + \sum_{\alpha, \alpha' > 0} \langle \alpha, -\alpha | v | \alpha', -\alpha' \rangle \hat{a}_{\alpha}^{\dagger} \hat{a}_{-\alpha}^{\dagger} \hat{a}_{-\alpha'} \hat{a}_{\alpha'}, \quad (2.44)$$

where  $\hat{a}_{\alpha}^{\dagger}$  creates a particle in single particle state  $|\alpha\rangle$  and  $\hat{a}_{\alpha}$  annihilates a particle in quantum state  $|\alpha\rangle$ .  $|-\alpha\rangle$  corresponds to a time reversed state of  $|\alpha\rangle$  with opposite spin. The first term in the right hand side of Eq. (2.44) represents the sum over all the occupied states below the Fermi surface. The second term represents the residual interaction essentially between a state with its time-reversed partner. Considering a constant matrix element  $-G$  for the interaction in the second term, the pairing Hamiltonian in Eq. (2.44) can be written as,

$$\hat{H} = \sum_{\alpha} \epsilon_{\alpha}^0 \hat{a}_{\alpha}^{\dagger} \hat{a}_{\alpha} - G \sum_{\alpha, \alpha' > 0} \hat{a}_{\alpha}^{\dagger} \hat{a}_{-\alpha}^{\dagger} \hat{a}_{-\alpha'} \hat{a}_{\alpha'}. \quad (2.45)$$

An analytic solution to this equation is not available. An approximate solution is provided by the BCS state which is given by,

$$|\varphi_{\text{BCS}}\rangle = \prod_{\alpha > 0}^{\infty} \left( u_{\alpha} + v_{\alpha} \hat{a}_{\alpha}^{\dagger} \hat{a}_{-\alpha}^{\dagger} \right) |0\rangle. \quad (2.46)$$

It signifies that the state  $(\alpha, -\alpha)$  is occupied with probability  $|v_{\alpha}|^2$  and is vacant with probability  $|u_{\alpha}|^2$ . In practical purpose  $u_{\alpha}$  and  $v_{\alpha}$  are considered to be real numbers. The normalization condition is given by,

$$\langle \varphi_{\text{BCS}} | \varphi_{\text{BCS}} \rangle = \prod_{\alpha > 0}^{\infty} (u_{\alpha}^2 + v_{\alpha}^2),$$



$$u_\alpha^2 + v_\alpha^2 = 1. \quad (2.47)$$

In Eq. (2.47), the quantity  $v_\alpha$  can be identified with  $w_\alpha$  in Eq. (2.30). The expectation value of the number operator is given by,

$$\begin{aligned} N = \langle \varphi_{\text{BCS}} | \hat{N} | \varphi_{\text{BCS}} \rangle &= \langle \varphi_{\text{BCS}} | \sum_{\alpha>0} \left( \hat{a}_\alpha^\dagger \hat{a}_\alpha + \hat{a}_{-\alpha}^\dagger \hat{a}_{-\alpha} \right) | \varphi_{\text{BCS}} \rangle \\ &= \sum_{\alpha>0} 2v_\alpha^2. \end{aligned} \quad (2.48)$$

Clearly,  $N$  is not a good quantum number for the Hamiltonian in Eq. (2.44), which can be understood by studying the particle number uncertainty as,

$$\begin{aligned} \Delta N^2 &= \langle \varphi_{\text{BCS}} | \hat{N}^2 | \varphi_{\text{BCS}} \rangle - \langle \varphi_{\text{BCS}} | \hat{N} | \varphi_{\text{BCS}} \rangle^2 \\ &= \left( 4 \sum_{\substack{\alpha \neq \alpha' \\ \alpha, \alpha' > 0}} v_\alpha^2 v_{\alpha'}^2 + 4 \sum_{\alpha>0} v_\alpha^2 \right) - \left( \sum_{\alpha>0} 2v_\alpha^2 \right)^2 \\ &= 4 \sum_{\alpha>0} u_\alpha^2 v_\alpha^2 \neq 0 \quad (\text{if } v_\alpha \neq 0 \text{ or } 1). \end{aligned} \quad (2.49)$$

Clearly,  $N$  becomes a good quantum number for  $v_\alpha = 0$  or  $1$ . For fractional occupation probability the values of  $u_\alpha$  and  $v_\alpha$  are found by solving a variational equation taking a product of Lagrange multiplier  $\lambda$  and  $N$  and subtracting it from the Hamiltonian in Eq. (2.44) as,

$$\begin{aligned} \delta \langle \varphi_{\text{BCS}} | \hat{H} - \lambda \hat{N} | \varphi_{\text{BCS}} \rangle &= 0 \\ \Rightarrow \frac{\partial}{\partial v_\alpha} \langle \varphi_{\text{BCS}} | \sum_{\alpha} (\epsilon_\alpha^0 - \lambda) \hat{a}_\alpha^\dagger \hat{a}_\alpha - G \sum_{\alpha, \alpha' > 0} \hat{a}_\alpha^\dagger \hat{a}_{-\alpha}^\dagger \hat{a}_{-\alpha'} \hat{a}_{\alpha'} | \varphi_{\text{BCS}} \rangle &= 0. \end{aligned} \quad (2.50)$$

Now, using the normalization condition  $u_\alpha^2 + v_\alpha^2 = 1$  one can write,

$$\frac{\partial}{\partial v_\alpha} = \frac{\partial}{\partial v_\alpha} \Big|_{u_\alpha} - \frac{v_\alpha}{u_\alpha} \frac{\partial}{\partial v_\alpha} \Big|_{v_\alpha}. \quad (2.51)$$

Further exploiting few expectation values,

$$\begin{aligned} \langle \varphi_{\text{BCS}} | \hat{a}_\alpha^\dagger \hat{a}_\alpha | \varphi_{\text{BCS}} \rangle &= v_\alpha^2, \\ \langle \varphi_{\text{BCS}} | \hat{a}_\alpha^\dagger \hat{a}_{-\alpha}^\dagger \hat{a}_{-\alpha'} \hat{a}_{\alpha'} | \varphi_{\text{BCS}} \rangle &= \begin{cases} u_\alpha v_\alpha u_{\alpha'} v_{\alpha'} & \text{for } \alpha \neq \alpha' \\ v_\alpha^2 & \text{for } \alpha = \alpha' \end{cases}, \end{aligned} \quad (2.52)$$

the second matrix element in Eq. (2.50) can be written as,

$$\begin{aligned} \langle \varphi_{\text{BCS}} | -G \sum_{\alpha, \alpha' > 0} \hat{a}_\alpha^\dagger \hat{a}_{-\alpha}^\dagger \hat{a}_{-\alpha'} \hat{a}_{\alpha'} | \varphi_{\text{BCS}} \rangle &= -G \sum_{\substack{\alpha \neq \alpha' \\ \alpha, \alpha' > 0}} u_\alpha v_\alpha u_{\alpha'} v_{\alpha'} - G \sum_{\alpha > 0} v_\alpha^2 \\ &= -G \left( \sum_{\alpha > 0} u_\alpha v_\alpha \right)^2 - G \sum_{\alpha > 0} v_\alpha^4. \end{aligned} \quad (2.53)$$

So implementing the variational equation in Eq. (2.50) and using the derivative in Eq. (2.51) one arrives at,

$$\begin{aligned} \frac{\partial}{\partial v_\alpha} \left[ 2 \sum_{\alpha > 0} (\epsilon_\alpha^0 - \lambda) v_\alpha^2 - G \left( \sum_{\alpha > 0} u_\alpha v_\alpha \right)^2 - G \sum_{\alpha > 0} v_\alpha^4 \right] &= 0 \\ 4 (\epsilon_\alpha^0 - \lambda) v_\alpha - 2G \left( \sum_{\alpha'} u_{\alpha'} v_{\alpha'} \right) u_\alpha - 4G v_\alpha^3 - \frac{v_\alpha}{u_\alpha} \left[ -2G \left( \sum_{\alpha' > 0} u_{\alpha'} v_{\alpha'} \right) v_\alpha \right] &= 0. \end{aligned} \quad (2.54)$$

Now with some definitions,

$$\begin{aligned}\Delta &= G \sum_{\alpha' > 0} u_{\alpha'} v_{\alpha'}, \\ \epsilon_{\alpha} &= \epsilon_{\alpha}^0 - \lambda - G v_{\alpha}^2,\end{aligned}\tag{2.55}$$

the variational equation [Eq. (2.50)] takes the form,

$$2\epsilon_{\alpha} v_{\alpha} u_{\alpha} + \Delta (v_{\alpha}^2 - u_{\alpha}^2) = 0.\tag{2.56}$$

In Eq. (2.55),  $\Delta$  is called as pairing gap and  $\lambda$  is identified as the chemical potential. Now, putting the condition  $\epsilon_{\alpha} \rightarrow \infty \Rightarrow v_{\alpha} = 0$  one gets,

$$\begin{aligned}v_{\alpha}^2 &= \frac{1}{2} \left( 1 - \frac{\epsilon_{\alpha}}{\sqrt{\epsilon_{\alpha}^2 + \Delta^2}} \right), \\ u_{\alpha}^2 &= \frac{1}{2} \left( 1 + \frac{\epsilon_{\alpha}}{\sqrt{\epsilon_{\alpha}^2 + \Delta^2}} \right).\end{aligned}\tag{2.57}$$

So the gap-equation is given by,

$$\begin{aligned}\Delta &= G \sum_{\alpha > 0} u_{\alpha} v_{\alpha} \\ &= \sum_{\alpha > 0} \frac{G}{2} \sqrt{1 - \frac{\epsilon_{\alpha}^2}{\epsilon_{\alpha}^2 + \Delta^2}} \\ \Rightarrow \Delta &= \frac{G}{2} \sum_{\alpha > 0} \frac{\Delta}{\sqrt{\epsilon_{\alpha}^2 + \Delta^2}}.\end{aligned}\tag{2.58}$$

In the present thesis work, constant gap (i.e.  $\Delta = \frac{11.2}{\sqrt{A}}$  MeV [51]) BCS approximation for the pairing is used. For the self-consistent determination of the radial wave functions in Skyrme or RMF formalism, first a set of single particle energies along with a guess value

of  $\lambda$  and  $G$  enter into the pairing calculation, separately for neutrons and protons. First value of  $\lambda$  is determined self-consistently by using equation for  $\epsilon_\alpha$  in Eq. (2.55) and  $v_\alpha^2$  in Eq. (2.57) fulfilling the number equation in Eq. (2.48).

Depending on the isospin of the particles concerned,  $N$  becomes number of neutrons or protons. Finally, the value of  $G$  is calculated from Eq. (2.58). The iteration to determine  $v_\alpha$  and pairing strength  $G$  runs inside the iteration process of Skyrme or RMF formalism. At the final step while determining the energy in Eq. (2.2) or (2.33), pairing energy is added separately as,

$$E_{q,\text{pair}} = \frac{-\Delta_q^2}{G_q}, \quad (2.59)$$

where,  $q$  is either neutron or proton.

## 2.3 Infinite Nuclear Matter

Infinite nuclear matter is a hypothetical isotropic system of infinite number of nucleons with no boundary and Coulomb interaction. The energy per nucleon for infinite nuclear matter with density  $\rho = (\rho_n + \rho_p)$  and isospin asymmetry  $\delta = \left(\frac{\rho_n - \rho_p}{\rho}\right)$  can be written as a Taylor's expansion as,

$$\begin{aligned} \mathcal{E}(\rho, \delta) &\approx \mathcal{E}(\rho, \delta = 0) + \frac{1}{2} \left( \frac{\partial^2 \mathcal{E}(\rho, \delta)}{\partial \delta^2} \right)_{\delta=0} \delta^2 + \frac{1}{4!} \left( \frac{\partial^4 \mathcal{E}(\rho, \delta)}{\partial \delta^4} \right)_{\delta=0} \delta^4 \\ &\approx \mathcal{E}(\rho, \delta = 0) + C_2(\rho) \delta^2 + C_4(\rho) \delta^4, \end{aligned} \quad (2.60)$$

where,  $\mathcal{E}(\rho, \delta = 0)$  represents the energy per nucleon for symmetric nuclear matter and  $C_2(\rho)$  is the symmetry energy. As the nuclear force symmetric under the exchange of neutrons and protons, the expansion contains only the even powers of  $\delta$ . For finite nuclear

systems the effect of asymmetry is quite less compared to the symmetric part. The maximum asymmetry associated with a nucleus is  $\delta \sim 0.33$ . So, the third term in the RHS of Eq. (2.60) has very less contribution to the binding energy of a nucleus. However, for dense asymmetric systems like neutron star, where the concerned asymmetry  $\delta \sim 0.7$ ,  $C_4(\rho)$  may contribute non-vanishingly to the system. Throughout this thesis work the expansion is thus restricted up to order of  $\delta^2$ . The symmetric nuclear matter attains a saturation where the energy minimizes. The corresponding density is coined as "saturation density" ( $= \rho_0$ ). At the center of the nuclei the density associated with finite nuclei is very close to this density. Thus, the saturation density is a very important quantity to estimate from theoretical models. All quantities characterizing infinite nuclear matter are evaluated at saturation density from a theoretical model, which are eventually used to construct the equation of state relevant for dense matter, subjected to heavy ion collision experiments or astrophysical observations.

Now, energy for symmetric matter  $\mathcal{E}(\rho, \delta = 0)$  or  $\mathcal{E}(\rho, 0)$  can be expanded around  $\rho_0$  as,

$$\begin{aligned} \mathcal{E}(\rho, 0) &\approx \mathcal{E}(\rho_0) + \frac{1}{2}K_0 \left( \frac{\rho_0 - \rho}{3\rho_0} \right)^2 - \frac{1}{6}Q_0 \left( \frac{\rho_0 - \rho}{3\rho_0} \right)^3, \\ \text{with, } K_0 &= 9\rho_0^2 \left( \frac{\partial^2 \mathcal{E}(\rho, 0)}{\partial \rho^2} \right)_{\rho_0}, \\ Q_0 &= 27\rho_0^3 \left( \frac{\partial^3 \mathcal{E}(\rho, 0)}{\partial \rho^3} \right)_{\rho_0}. \end{aligned} \quad (2.61)$$

In the right hand side of Eq. (2.61), the first derivative vanishes as the energy attains its minimum at  $\rho_0$ . The quantity  $K_0$  and  $Q_0$  are called the incompressibility and skewness parameter for symmetric matter. Similar to  $\mathcal{E}(\rho, 0)$  in Eq. (2.61), one can also expand

$C_2(\rho)$  in Eq. (2.60) around  $\rho_0$  as,

$$\begin{aligned}
C_2(\rho) &\approx C_2^0 - L_0 \left( \frac{\rho_0 - \rho}{3\rho_0} \right) + \frac{1}{2} K_{sym}^0 \left( \frac{\rho_0 - \rho}{3\rho_0} \right)^2 - \frac{1}{6} Q_{sym}^0 \left( \frac{\rho_0 - \rho}{3\rho_0} \right)^3, \\
\text{with, } C_2^0 &= C_2(\rho_0), \\
L_0 &= 3\rho_0 \left( \frac{\partial C_2(\rho)}{\partial \rho} \right)_{\rho_0}, \\
K_{sym}^0 &= 9\rho_0^2 \left( \frac{\partial^2 C_2(\rho)}{\partial \rho^2} \right)_{\rho_0}, \\
Q_{sym}^0 &= 27\rho_0^3 \left( \frac{\partial^3 C_2(\rho)}{\partial \rho^3} \right)_{\rho_0}. \tag{2.62}
\end{aligned}$$

Here,  $L_0$  is slope parameter of symmetry energy,  $K_{sym}^0$  the symmetry energy curvature parameter and  $Q_{sym}^0$  the symmetry energy skewness parameter. These quantities play very important roles in the study of asymmetric systems e.g. nuclei near drip line or astrophysical objects like neutron star.

For nuclear matter, single particle levels are of no interest. In mean-field formalism, with a given set of parameters, saturation density  $\rho_0$  can be determined by minimizing the energy for symmetric matter with respect to particle density  $\rho$ . To do so, different type of densities in Eq. (2.7) and (2.28) are taken to be equal for neutrons and protons. Moreover, infinite nuclear matter is uniform by definition. So gradients of all type of densities vanish identically inside nuclear matter. Other symmetric nuclear matter properties defined in Eq. (2.61) are then calculated accordingly by performing numerical derivatives of energy density with respect to  $\rho$ . For asymmetric nuclear matter, symmetry energy parameters defined in Eq. (2.62) can be calculated by taking numerical derivatives of energy with respect to corresponding powers of  $\delta$  and  $\rho$ .

---

## ERROR ANALYSIS

---

### 3.1 Introduction

In 1976, George E. P. Box commented on 'Science and statistics' as, "*Since all models are wrong the scientist can not obtain a "correct" one by excessive elaboration*" [58]. Probably, nothing can put more aptly the hazards of extrapolating theoretical models. Any experimental measurement is not acceptable without specification on the uncertainties. However, "*its all too often the case that the numerical results are presented without uncertainty estimates*"; as pointed out by the editors of Physical Review A [59]. More often than not, theoretical models involve prediction of observables beyond its domain of validity. For example, models based on non-relativistic Skyrme force or relativistic mean field (RMF) obtained by fitting experimental data on finite nuclei are often used to predict neutron-star properties. So, estimating the statistical uncertainties for nuclear models is inevitable.

As the basic nuclear interaction between two nucleons is not known exactly, uncertainties are bound to creep in for the nuclear models obtained by fitting properties of finite nuclei and neutron stars. If the models were exact, any prediction by the models would match

exactly with the experiment or observation, leaving no room for new measurements to help in any new understanding. On the contrary, for a model built without any preconceived fundamental knowledge, all the measured or observed quantities would be independent to each other, resulting in zero predictive power. The real scenario lies in between these two extreme situations. Few recent calculations [60–64] put forward an extensive importance on the error estimation in theoretical models, which includes error on the optimized parameters as well as on the predicted or estimated experimental and empirical observables. Moreover, statistical analyses address how fast the objective function (typically a  $\chi^2$  function) moves away from its minimum value when one perturbs the optimized parameter set. Depending on the set of observables one uses to optimize the parameter space, correlation may exist among different observables and parameters. Studying the correlations among different observables and parameters offers a load of information which can't be comprehended otherwise.

## 3.2 Covariance analysis

To obtain the optimized model parameters, a set of experimental data is fitted. First a suitable objective function is minimized, which is defined as [61, 62],

$$\chi^2(\mathbf{p}) = \sum_{i=1}^{N_d} \left( \frac{\mathcal{O}_i^{th} - \mathcal{O}_i^{exp}}{\Delta\mathcal{O}_i} \right)^2. \quad (3.1)$$

In Eq. (3.1),  $\mathbf{p}$  ( $p_1, p_2 \dots p_{N_p}$ ) is the parameters set with typically  $N_d \sim 10$  for nuclear models.  $N_d$  is the number of data used to fit the parameters.  $\mathcal{O}^{th}$  is the value of an observable calculated theoretically with the parameter set  $\mathbf{p}$ .  $\mathcal{O}^{exp}$  is experimental value of the corresponding observable. The quantity  $\Delta\mathcal{O}$  represents the adopted error on any observ-



able  $\mathcal{O}$  which is given by  $\Delta\mathcal{O}^2 = (\Delta\mathcal{O}^{th})^2 + (\Delta\mathcal{O}^{exp})^2 + (\Delta\mathcal{O}^{num})^2$ , where contributions come from theory, experiment as well as numerical methods associated with the analysis. Out of these three contributions the most undetermined one is the theoretical error. One needs to be very careful to estimate the adopted theoretical error. Often nuclear models miss certain many body correlations in its formulation. Demanding too much accuracy on certain channels may end up in erroneous optimizations. Following the definition of  $\chi^2$  in Eq. (3.1), one can also define the likelihood function of a parameter set by,

$$L(\mathbf{p}) = N \exp \left[ -\frac{1}{2} \chi^2(\mathbf{p}) \right]. \quad (3.2)$$

As the name suggests, it determines the likelihood of a parameter set  $\mathbf{p}$  to reproduce the experimental data. Immediately the average value of a quantity  $A(\mathbf{p})$  can be obtained as,

$$\bar{A} = \int L(\mathbf{p}) \cdot A(\mathbf{p}) d\mathbf{p}. \quad (3.3)$$

Using the likelihood function, variance on  $A$  and covariance between  $A$  and  $B$  can be expressed as,

$$\begin{aligned} \overline{(\Delta A)^2} &= \int L(\mathbf{p}) \cdot (A(\mathbf{p}) - \bar{A})^2 d\mathbf{p}, \\ \overline{(\Delta A \Delta B)} &= \int L(\mathbf{p}) \cdot (A(\mathbf{p}) - \bar{A}) (B(\mathbf{p}) - \bar{B}) d\mathbf{p}. \end{aligned} \quad (3.4)$$

The correlation coefficient between  $A$  and  $B$  can be obtained as [65],

$$C_{AB} = \frac{\overline{\Delta A \Delta B}}{\sqrt{\overline{\Delta A^2} \overline{\Delta B^2}}}. \quad (3.5)$$

The ideal way to obtain computationally the average or variance of any quantity and

covariance between two quantities would to make samples over the whole parameter space using a Metropolis-Monte-Carlo algorithm originally given by Metropolis et al [66]. In a Monte-Carlo approach over a huge sample parameter space the definitions of average, variance of a quantity and covariance between two quantities would be redefined as,

$$\begin{aligned}
\bar{A} &= \lim_{M \rightarrow \infty} \frac{1}{M} \sum_{m=1}^M A(\mathbf{p}_m) \\
\overline{(\Delta A)^2} &= \lim_{M \rightarrow \infty} \frac{1}{M} \sum_{m=1}^M (A(\mathbf{p}_m) - \bar{A})^2 \\
\overline{(\Delta A \Delta B)} &= \lim_{M \rightarrow \infty} \frac{1}{M} \sum_{m=1}^M (A(\mathbf{p}_m) - \bar{A})(B(\mathbf{p}_m) - \bar{B}) \quad (3.6)
\end{aligned}$$

Typical calculation of the objective function  $\chi^2$  with  $\sim 10$  parameters in a nuclear model takes few minutes of computation time. Sampling over several thousands of parameter sets would end up taking few months of computation time to estimate the uncertainties. So a more efficient method is essential to perform statistical error analysis involving nuclear models.

The most tractable method to calculate the statistical uncertainties is *covariance analysis* [65]. First the  $\chi^2$  function is minimized following a derivative method. A typical method would be Levenberg-Marquardt method. Once the minimum of the  $\chi^2$  function is obtained, it can be expanded around the minimum by Taylor's expansion. Keeping upto quadratic terms the expansion can be approximated as,

$$\begin{aligned}
\chi^2(\mathbf{p}) &\approx \chi^2(\mathbf{p}_0) + \sum_{i=1}^{N_p} (p - p_0)_i \left( \frac{\partial \chi^2(\mathbf{p})}{\partial p_i} \right)_{\mathbf{p}_0} + \frac{1}{2} \sum_{i,j=1}^{N_p} (p - p_0)_i \left( \frac{\partial^2 \chi^2(\mathbf{p})}{\partial p_i \partial p_j} \right)_{\mathbf{p}_0} (p - p_0)_j, \\
\chi^2(\mathbf{p}) &\approx \chi^2(\mathbf{p}_0) + 0 + \sum_{i,j=1}^{N_p} (p - p_0)_i \mathcal{M}_{ij} (p - p_0)_j \quad (3.7)
\end{aligned}$$

The first derivative of  $\chi^2$  vanishes as the objective function is at minimum. Here, Hessian matrix is given by,

$$\mathcal{M}_{ij} = \frac{1}{2} \left( \frac{\partial^2 \chi^2(\mathbf{p})}{\partial p_i \partial p_j} \right)_{\mathbf{p}_0}. \quad (3.8)$$

Now following Eq. (3.2), the likelihood function in quadratic approximation takes the form,

$$L(\mathbf{p}) = N \exp \left[ -\frac{1}{2} \chi^2(\mathbf{p}) \right] \approx N' \exp \left[ -\frac{1}{2} \sum_{i,j=1}^n (p - p_0)_i \mathcal{M}_{ij} (p - p_0)_j \right], \quad (3.9)$$

where, contribution of  $\chi^2(\mathbf{p}_0)$  is absorbed in the constant  $N'$ . In Eq. (3.9), if the quantity inside the exponential remains constant over a sample parameter sets, it forms an ellipsoid of constant probability surface over the multidimensional parameter space. It can also be understood from the the Eq. (3.7) by putting the first term in the right to the left hand side. Upon projecting this multidimensional ellipsoid along any two parameters, one can study correlation between two parameters. One can also explore correlation between a pair of observables by exploiting the covariance ellipsoid for parameters. For that one needs to calculate the values of the observables of interest using the parameters lying within the domain of covariance ellipsoid. A representative example of the covariance ellipsoid is depicted in Fig. 3.1 taken from Ref. [61], where neutron-skin thickness  $\Delta r_{\text{np}}$  of  $^{208}\text{Pb}$  is plotted against dipole polarizability and effective mass  $\frac{m^*}{m}$  of nucleon. The thinner shape of the ellipsoid in the “ $\Delta r_{\text{np}}$  - dipole polarizability” plane contrasting to that in the “ $\Delta r_{\text{np}}$  -  $\frac{m^*}{m}$ ” plane depicts stronger correlation in the former compared to the latter.

Now further, integration of the likelihood function over the whole parameter space

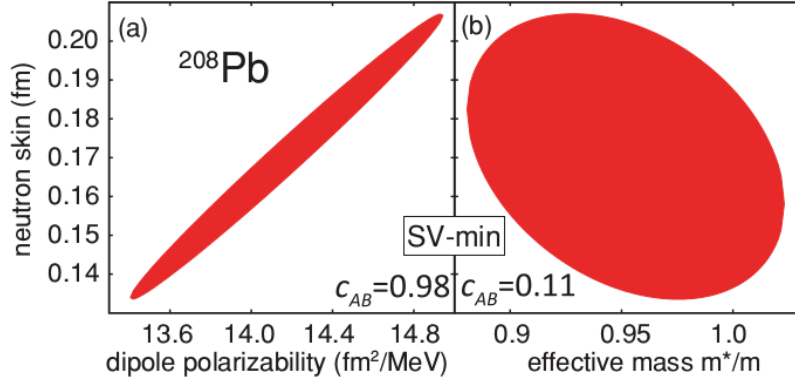


Figure 3.1: Covariance ellipsoids for two pairs of observables as given in Ref. [61]. See text for details.

gives unity,

$$\int_{-\infty}^{+\infty} L(\mathbf{p}) d\mathbf{p} = N' \int_{-\infty}^{+\infty} \exp \left[ -\frac{1}{2} (\mathbf{p} - \mathbf{p}_0)^T \mathcal{M} (\mathbf{p} - \mathbf{p}_0) \right] d\mathbf{p} = 1. \quad (3.10)$$

Here all the bold notations signify matrices. If there exists an orthogonal transformation so that,

$$\mathcal{M} = \mathbf{O}^T \tilde{\mathcal{M}} \mathbf{O}, \quad (3.11)$$

where,  $\tilde{\mathcal{M}} = \text{diag} [\tilde{\mathcal{M}}_1 \quad \tilde{\mathcal{M}}_2 \quad \dots \tilde{\mathcal{M}}_{N_p}]$ , multidimensional ellipsoid equation can be rewritten as,

$$\begin{aligned} (\mathbf{p} - \mathbf{p}_0)^T \mathcal{M} (\mathbf{p} - \mathbf{p}_0) &= (\mathbf{p} - \mathbf{p}_0)^T \mathbf{O}^T \tilde{\mathcal{M}} \mathbf{O} (\mathbf{p} - \mathbf{p}_0) \\ &= (\mathbf{O} (\mathbf{p} - \mathbf{p}_0))^T \tilde{\mathcal{M}} \mathbf{O} (\mathbf{p} - \mathbf{p}_0) \\ &= \tilde{\mathbf{p}}^T \tilde{\mathcal{M}} \tilde{\mathbf{p}} \\ &= \sum_{k=1}^{N_p} \tilde{p}_k \tilde{\mathcal{M}}_k \tilde{p}_k = \sum_{k=1}^{N_p} \tilde{\mathcal{M}}_k \tilde{p}_k^2. \end{aligned} \quad (3.12)$$

So, using Eq. (3.10) and (3.12) value of  $N'$  can be obtained as,

$$\begin{aligned}
\int_{-\infty}^{+\infty} L(\mathbf{p}) d\mathbf{p} &= N' \int_{-\infty}^{+\infty} \exp \left[ -\frac{1}{2} \sum_{k=1}^{N_p} \tilde{\mathcal{M}}_k \tilde{p}_k^2 d\tilde{p} \right] \\
&= N' \prod_{k=1}^{N_p} \int_{-\infty}^{+\infty} \exp \left[ -\frac{1}{2} \tilde{\mathcal{M}}_k \tilde{p}_k^2 \right] d\tilde{p}_k \\
&= N' \prod_{k=1}^{N_p} \left[ \frac{2\pi}{\tilde{\mathcal{M}}_k} \right]^{1/2} \\
\Rightarrow 1 &= N' (2\pi)^{\frac{N_p}{2}} \text{Det}^{-\frac{1}{2}}[\tilde{\mathcal{M}}] \\
\Rightarrow N' &= \left[ \frac{2\pi}{\tilde{\mathcal{M}}_k} \right]^{-\frac{N_p}{2}} = \left\{ \frac{(2\pi)^{N_p}}{\text{Det}[\tilde{\mathcal{M}}]} \right\}^{-\frac{1}{2}} .
\end{aligned} \tag{3.13}$$

Now,  $A(\mathbf{p})$  can be expanded around the optimal parameter set  $\mathbf{p}_0$  as in Eq. (3.7) by keeping only upto quadratic terms as,

$$\begin{aligned}
A(\mathbf{p}) &\approx A(\mathbf{p}_0) + \sum_{k=1}^{N_p} (\mathbf{p} - \mathbf{p}_0)_k \left( \frac{\partial A}{\partial p_k} \right)_{\mathbf{p}_0} + \frac{1}{2} \sum_{k,l=1}^{N_p} (\mathbf{p} - \mathbf{p}_0)_k \left( \frac{\partial^2 A}{\partial p_k \partial p_l} \right)_{\mathbf{p}_0} (\mathbf{p} - \mathbf{p}_0)_l \\
&= A_0 + (\mathbf{p} - \mathbf{p}_0)^T A'_0 + \frac{1}{2} (\mathbf{p} - \mathbf{p}_0)^T A''_0 (\mathbf{p} - \mathbf{p}_0) .
\end{aligned} \tag{3.14}$$

Upon using the expansion of  $A(\mathbf{p})$  around  $\mathbf{p}_0$  in Eq. (3.14) and taking help from Eq. (3.12), the average  $\bar{A}$  can be calculated as,

$$\begin{aligned}
\bar{A} &= \int_{-\infty}^{+\infty} L(\mathbf{p}) \cdot A(\mathbf{p}) d\mathbf{p} \\
&= N' \int_{-\infty}^{+\infty} A(\mathbf{p}) \exp \left[ -\frac{1}{2} (\mathbf{p} - \mathbf{p}_0)^T \tilde{\mathcal{M}} (\mathbf{p} - \mathbf{p}_0) \right] d\mathbf{p} \\
&= N' \int_{-\infty}^{+\infty} \left\{ A_0 + (\mathbf{p} - \mathbf{p}_0)^T A'_0 + \frac{1}{2} (\mathbf{p} - \mathbf{p}_0)^T A''_0 (\mathbf{p} - \mathbf{p}_0) \right\} \\
&\quad \exp \left[ -\frac{1}{2} (\mathbf{p} - \mathbf{p}_0)^T \tilde{\mathcal{M}} (\mathbf{p} - \mathbf{p}_0) \right] d\mathbf{p}
\end{aligned}$$

$$\begin{aligned}
&= A_0 + 0 + \frac{1}{2}N' \int_{-\infty}^{+\infty} \{(\mathbf{p} - \mathbf{p}_0)^T A_0''(\mathbf{p} - \mathbf{p}_0)\} \\
&\quad \exp \left[ -\frac{1}{2}(\mathbf{p} - \mathbf{p}_0)^T \mathcal{M}(\mathbf{p} - \mathbf{p}_0) \right] d\mathbf{p} \\
&= A_0 + \frac{1}{2}N' \int_{-\infty}^{+\infty} \{(\mathbf{p} - \mathbf{p}_0)^T \mathbf{O}\mathbf{O}^T A_0'' \mathbf{O}\mathbf{O}^T (\mathbf{p} - \mathbf{p}_0)\} \exp \left[ -\frac{1}{2}\tilde{\mathbf{p}}^T \tilde{\mathcal{M}}\tilde{\mathbf{p}} \right] d\tilde{\mathbf{p}} \\
&= A_0 + \frac{1}{2}N' \int_{-\infty}^{+\infty} \{ \tilde{\mathbf{p}}^T \tilde{A}_0'' \tilde{\mathbf{p}} \} \exp \left[ -\frac{1}{2}\tilde{\mathbf{p}}^T \tilde{\mathcal{M}}\tilde{\mathbf{p}} \right] d\tilde{\mathbf{p}}. \tag{3.15}
\end{aligned}$$

In the last step  $\tilde{A}_0'' = \mathbf{O}A_0''\mathbf{O}^T$  was used. So the expression for  $\bar{A}$  can be further simplified as,

$$\begin{aligned}
\bar{A} &= A_0 + \frac{1}{2}N' \int_{-\infty}^{+\infty} \left\{ \sum_{k',l'=1}^{N_p} \tilde{p}_{k'} \left( \tilde{A}_0'' \right)_{k'l'} \tilde{p}_{l'} \right\} \exp \left[ -\frac{1}{2} \sum_{k=1}^{N_p} \tilde{\mathcal{M}}_k \tilde{p}_k^2 \right] d\tilde{\mathbf{p}} \\
&= A_0 + \frac{1}{2}N' \int_{-\infty}^{+\infty} \left\{ \sum_{k',l'=1}^{N_p} \tilde{p}_{k'} \left( \tilde{A}_0'' \right)_{k'l'} \tilde{p}_{l'} \right\} \prod_{k=1}^{N_p} \exp \left[ -\frac{1}{2} \tilde{\mathcal{M}}_k \tilde{p}_k^2 \right] d\tilde{p}_k \\
&= A_0 + \frac{1}{2}N' \int_{-\infty}^{+\infty} \left\{ \sum_{k'=1}^{N_p} \tilde{p}_{k'} \left( \tilde{A}_0'' \right)_{k'k'} \tilde{p}_{k'} \right\} \prod_{k=1}^{N_p} \exp \left[ -\frac{1}{2} \tilde{\mathcal{M}}_k \tilde{p}_k^2 \right] d\tilde{p}_k. \tag{3.16}
\end{aligned}$$

For the last step the fact was used that any Gaussian integral with an odd power of variable multiplied to it vanishes. So the expression for  $\bar{A}$  can be further simplified as,

$$\begin{aligned}
\bar{A} &= A_0 + \frac{1}{2}N' \int_{-\infty}^{+\infty} \left\{ \sum_{k'=1}^{N_p} \left( \tilde{A}_0'' \right)_{k'k'} \tilde{p}_{k'}^2 \right\} \exp \left[ -\frac{1}{2} \tilde{\mathcal{M}}_{k'} \tilde{p}_{k'}^2 \right] d\tilde{p}_{k'} \\
&\quad \int_{-\infty}^{+\infty} \prod_{k \neq k', 1}^{N_p} \exp \left[ -\frac{1}{2} \tilde{\mathcal{M}}_k \tilde{p}_k^2 \right] d\tilde{p}_k \\
&= A_0 + \frac{1}{2} \sum_{k'=1}^{N_p} \left\{ \frac{\tilde{\mathcal{M}}_{k'}}{2\pi} \right\}^{\frac{N_p}{2}} \left\{ \frac{2\pi}{\tilde{\mathcal{M}}_{k'}} \right\}^{\frac{N_p-1}{2}} \left( \tilde{A}_0'' \right)_{k'k'} \int_{-\infty}^{+\infty} \tilde{p}_{k'}^2 \exp \left[ -\frac{1}{2} \tilde{\mathcal{M}}_{k'} \tilde{p}_{k'}^2 \right] d\tilde{p}_{k'} \\
&= A_0 + \frac{1}{2} \sum_{k'=1}^{N_p} \left\{ \frac{\tilde{\mathcal{M}}_{k'}}{2\pi} \right\}^{\frac{1}{2}} \left( \tilde{A}_0'' \right)_{k'k'} \left\{ \frac{2\pi}{\tilde{\mathcal{M}}_{k'}^3} \right\}^{\frac{1}{2}}
\end{aligned}$$

$$\begin{aligned}
&= A_0 + \frac{1}{2} \sum_{k'=1}^{N_p} \tilde{\mathcal{M}}_{k'}^{-1} \left( \tilde{A}_0'' \right)_{k'k'} \\
&= A_0 + \frac{1}{2} \text{Tr} \left[ \tilde{\mathcal{M}}^{-1} \tilde{A}_0'' \right] \\
\Rightarrow \bar{A} &= A_0 + \frac{1}{2} \text{Tr} \left[ \mathcal{M}^{-1} A_0'' \right] . \tag{3.17}
\end{aligned}$$

In the last step, simply the cyclic property during the matrix multiplication was used under the orthogonal transformation. The inverse of the Hessian matrix  $\mathcal{M}^{-1}$  is commonly known as the "curvature" matrix. Now the deviation in the observable  $A(\mathbf{p})$  from its average  $\bar{A}$  is given by,

$$\begin{aligned}
\Delta A &= A(\mathbf{p}) - \bar{A} \\
&= A_0 + (\mathbf{p} - \mathbf{p}_0)^T A'_0 + \frac{1}{2} (\mathbf{p} - \mathbf{p}_0)^T A_0'' (\mathbf{p} - \mathbf{p}_0) - A_0 - \frac{1}{2} \text{Tr} \left[ \mathcal{M}^{-1} A_0'' \right] \\
&= (\mathbf{p} - \mathbf{p}_0)^T A'_0 + \frac{1}{2} (\mathbf{p} - \mathbf{p}_0)^T A_0'' (\mathbf{p} - \mathbf{p}_0) - \frac{1}{2} \text{Tr} \left[ \mathcal{M}^{-1} A_0'' \right] . \tag{3.18}
\end{aligned}$$

Similarly, the deviation in a quantity  $B$  can be calculated following Eq. (3.18). So one can write now,

$$\begin{aligned}
\Delta A(\mathbf{p}) \Delta B(\mathbf{p}) &\approx \left\{ (\mathbf{p} - \mathbf{p}_0)^T A'_0 + \frac{1}{2} (\mathbf{p} - \mathbf{p}_0)^T A_0'' (\mathbf{p} - \mathbf{p}_0) - \frac{1}{2} \text{Tr} \left[ \mathcal{M}^{-1} A_0'' \right] \right\} \\
&\quad \left\{ B_0'^T (\mathbf{p} - \mathbf{p}_0) + \frac{1}{2} (\mathbf{p} - \mathbf{p}_0)^T B_0'' (\mathbf{p} - \mathbf{p}_0) - \frac{1}{2} \text{Tr} \left[ \mathcal{M}^{-1} B_0'' \right] \right\} \\
&\approx (\mathbf{p} - \mathbf{p}_0)^T A'_0 B_0'^T (\mathbf{p} - \mathbf{p}_0) + \mathcal{O}\{\Delta \mathbf{p}^3\} . \tag{3.19}
\end{aligned}$$

Neglecting the contribution from the terms containing beyond  $\mathcal{O}\{\Delta \mathbf{p}^2\}$  and calling  $A'_0 B_0'^T$  as  $(AB)'_0$ , covariance between  $A(\mathbf{p})$  and  $B(\mathbf{p})$  can be obtained following the definition in

Eq. (3.4) as,

$$\begin{aligned}
\overline{(\Delta A \Delta B)} &= N' \int_{-\infty}^{+\infty} \{(\mathbf{p} - \mathbf{p}_0)^T (AB)'_0 (\mathbf{p} - \mathbf{p}_0)\} \exp \left[ -\frac{1}{2} (\mathbf{p} - \mathbf{p}_0)^T \mathcal{M} (\mathbf{p} - \mathbf{p}_0) \right] d\mathbf{p} \\
&= N' \int_{-\infty}^{+\infty} \{(\mathbf{p} - \mathbf{p}_0)^T \mathbf{O}^T \mathbf{O} (AB)'_0 \mathbf{O} \mathbf{O}^T (\mathbf{p} - \mathbf{p}_0)\} \\
&\quad \exp \left[ -\frac{1}{2} (\mathbf{p} - \mathbf{p}_0)^T \mathcal{M} (\mathbf{p} - \mathbf{p}_0) \right] d\mathbf{p} \\
&= N' \int_{-\infty}^{+\infty} \{ \tilde{\mathbf{p}}^T (\tilde{A}\tilde{B})'_0 \tilde{\mathbf{p}} \} \exp \left[ -\frac{1}{2} \tilde{\mathbf{p}}^T \tilde{\mathcal{M}} \tilde{\mathbf{p}} \right] d\tilde{\mathbf{p}} \\
&= N' \int_{-\infty}^{+\infty} \left\{ \sum_{k',l'=1}^{N_p} \tilde{p}_{k'} \left( (\tilde{A}\tilde{B})'_0 \right)_{k'l'} \tilde{p}_{l'} \right\} \prod_{k=1}^{N_p} \exp \left[ -\frac{1}{2} \tilde{\mathcal{M}}_k \tilde{p}_k^2 \right] d\tilde{p}_k . \quad (3.20)
\end{aligned}$$

Now, following the same steps as  $\bar{A}$  in Eq. (3.17), the expression for covariance between  $A$  and  $B$  can be written as,

$$\begin{aligned}
\overline{(\Delta A \Delta B)} &= \text{Tr} [\mathcal{M}^{-1} (AB)'_0] \\
&= \sum_{k,l=1}^{N_p} \mathcal{M}_{k,l}^{-1} (A'_0 B'_0)^T_{l,k} \\
&= \sum_{k,l=1}^{N_p} \mathcal{M}_{k,l}^{-1} (A_0^T B_0')_{k,l} \\
&= \sum_{k,l=1}^{N_p} (A_0')_k \mathcal{M}_{k,l}^{-1} (B_0)_l \\
\overline{(\Delta A \Delta B)} &= \sum_{k,l=1}^{N_p} \left( \frac{\partial A}{\partial p_k} \right)_{\mathbf{p}_0} \mathcal{M}_{k,l}^{-1} \left( \frac{\partial B}{\partial p_l} \right)_{\mathbf{p}_0} . \quad (3.21)
\end{aligned}$$

Putting  $A = B$ , variance on any quantity  $A$  can be calculated as,

$$\overline{(\Delta A)^2} = \sum_{k,l=1}^{N_p} \left( \frac{\partial A}{\partial p_k} \right)_{\mathbf{p}_0} \mathcal{M}_{k,l}^{-1} \left( \frac{\partial A}{\partial p_l} \right)_{\mathbf{p}_0} . \quad (3.22)$$



As, the parameters of a model are considered to be independent to one another, one can write,

$$\begin{aligned} \frac{\partial p_k}{\partial p_{k'}} &= \delta_{kk'} \\ \Rightarrow \overline{(\Delta p_k \Delta p_{k'})} &= \mathcal{M}_{k,k'}^{-1} \quad \& \quad \overline{(\Delta p_k)^2} = \mathcal{M}_{k,k}^{-1}. \end{aligned} \quad (3.23)$$

So, the diagonal elements of the curvature matrix quantify the variance on the model parameters. Upon taking the square root of the diagonal elements, one can obtain the error on the parameters.

### 3.3 Minimization and Sensitivity analysis

In the present thesis work, parameters of a relativistic mean-field (RMF) model are optimized. A close variant of Levenberg-Marquardt [67] was employed to minimize the  $\chi^2$  function as defined in Eq. (3.1). The algorithm typically uses the inverse-Hessian or curvature matrix method. Using the definition of  $\chi^2$  in Eq. (3.1), Hessian matrix can be calculated as,

$$\begin{aligned} \mathcal{M}_{k,l} &= \frac{1}{2} \left( \frac{\partial^2 \chi^2(\mathbf{p}_0)}{\partial p_k \partial p_l} \right) = \frac{1}{2} \frac{\partial^2}{\partial p_k \partial p_l} \left\{ \sum_{i=1}^{N_d} \left( \frac{\mathcal{O}_i^{th} - \mathcal{O}_i^{exp}}{\Delta \mathcal{O}_i} \right)^2 \right\} \\ &= \sum_{i=1}^{N_d} \frac{1}{\Delta \mathcal{O}_i^2} \left[ \left( \frac{\partial \mathcal{O}_i^{th}}{\partial p_k} \right) \left( \frac{\partial \mathcal{O}_i^{th}}{\partial p_l} \right) + (\mathcal{O}_i^{th} - \mathcal{O}_i^{exp}) \left( \frac{\partial^2 \mathcal{O}_i^{th}}{\partial p_k \partial p_l} \right) \right]. \end{aligned} \quad (3.24)$$

Here,  $(\mathcal{O}_i^{th} - \mathcal{O}_i^{exp})$  is the residual error in  $\mathcal{O}_i$ . If the model space is reasonable, residual errors are small. Moreover, one can expect that they are random in sign. Then the Hessian

matrix is approximately obtained as [65]

$$\begin{aligned}
\mathcal{M}_{k,l} &\approx \sum_{i=1}^{N_d} \frac{1}{\Delta\mathcal{O}_i^2} \left( \frac{\partial\mathcal{O}_i^{th}}{\partial p_k} \right) \left( \frac{\partial\mathcal{O}_i^{th}}{\partial p_l} \right) \\
&= \sum_{i=1}^{N_d} \left( \frac{1}{\Delta\mathcal{O}_i} \frac{\partial\mathcal{O}_i^{th}}{\partial p_k} \right) \left( \frac{1}{\Delta\mathcal{O}_i} \frac{\partial\mathcal{O}_i^{th}}{\partial p_l} \right) \\
&= \sum_{i=1}^{N_d} J_{i,k} J_{i,l} .
\end{aligned} \tag{3.25}$$

So, the Hessian matrix and the corresponding curvature matrix can be obtained without ever calculating any double derivative of the observables with respect to the parameters. The  $\mathbf{J}$  matrix is called the "Jacobian" matrix which is nothing but the derivative of an observable with respect to parameters weighted by the corresponding adopted error. This approximation along with the Levenberg-Marquardt method provides a very efficient and stable minimization procedure.

It was mentioned in the previous section that proper estimation of the adopted errors i.e.  $\Delta\mathcal{O}_i$  are very important. As there is no proper prescription to estimate  $\Delta\mathcal{O}_i$ , some arbitrariness is inevitable. However, the arbitrariness can be reduced significantly by introducing a global 's' factor [62, 69],

$$s = \frac{\chi^2(\mathbf{p}_0)}{N_d - N_p}. \tag{3.26}$$

While performing the covariance analysis as described in the previous section, ultimately the curvature matrix  $\mathcal{M}^{-1}$  is replaced by  $(s\mathcal{M}^{-1})$  and rest of the procedure is followed.

To study the overall impact of each type of data on the optimized parameters a "sensi-

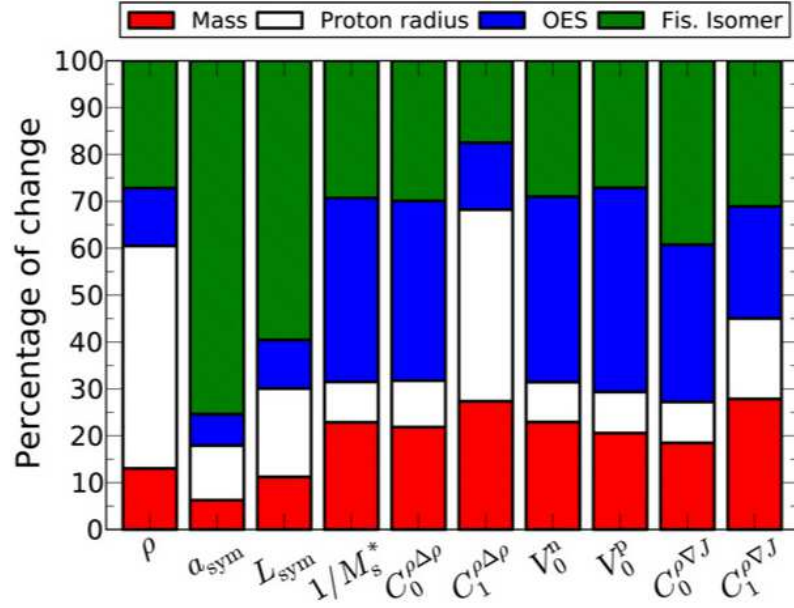


Figure 3.2: Relative Sensitivity of different parameters of UNEDF1 [68] to different type of data used in the fit, as given in Ref. [62].

tivity matrix”  $S$  is defined as [60, 62, 68],

$$S(\mathbf{p}) = [\mathbf{J}(\mathbf{p})\mathbf{J}^T(\mathbf{p})]^{-1} \mathbf{J}(\mathbf{p}). \quad (3.27)$$

For  $k$ -th row in the sensitivity matrix  $S_{i,k}$  corresponding to a single parameter, one can compute the partial sums over different type of data  $i_1, i_2, \dots$  where  $i = i_1 + i_2 + \dots$ . Consequently, a percentage contribution from each type of data  $i_1, i_2$  etc can be obtained by normalizing to the summation over all type of data as 100% i.e.  $\sum_i S_{i,k} = 100\%$  for the  $k$ -th parameter. A representative example is depicted in Fig. 3.2 as given in Ref. [62].

All the techniques described in Chapter 3 have been extensively used in Chapter 4 to test the merit of a relativistic mean field model. The numerical codes to perform the covariance and sensitivity analysis are also developed during the present thesis work.

---

# CONSTRAINING THE SYMMETRY ENERGY PARAMETERS USING A RELATIVISTIC MEAN FIELD MODEL

---

## 4.1 Introduction

The symmetry energy coefficient  $C_2^0$  (Eq. (2.62)) is well constrained from binding energies of finite nuclei with its mean value  $\sim 32$  MeV [1, 2, 70–73]. However, symmetry energy slope  $L_0$ , shows a wide variation  $\sim 20 - 120$  MeV [10, 13–15, 25–27, 29–38]. It can be realized by looking at the abscissa of Fig. (4.1), where neutron-skin thickness  $\Delta r_{np}$  of  $^{208}\text{Pb}$  is plotted as a function of  $L_0$  for a set of  $\sim 40$  mean-field models, which is taken from Ref. [15]. One can also observe a linear correlation between  $\Delta r_{np}$  of  $^{208}\text{Pb}$  and  $L_0$ . Thus, precise information of  $\Delta r_{np}$  of  $^{208}\text{Pb}$  can constrain the value of  $L_0$  tightly. From the analysis of data on the precisely known nuclear masses in macroscopic nuclear models,

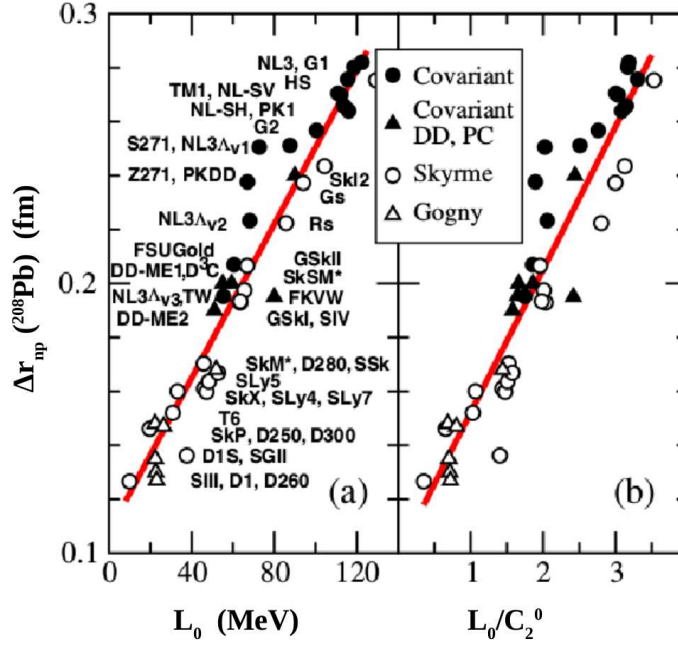


Figure 4.1:  $\Delta r_{np}$  of  $^{208}\text{Pb}$  plotted as a function of  $L_0$  (left panel) and  $\frac{L_0}{C_2^0}$  (right panel), for  $\sim 40$  mean-field models as given in Ref [15].

$L_0$  is known with a fair amount of accuracy,  $L_0 = 60 \pm 20$  MeV [1, 2, 74, 75]. Energy density functionals (EDF) in microscopic mean field models, parametrized to reproduce the binding energies of nuclei along with some other specific nuclear observables do not, however, display such constraints on  $L_0$ . Questions then arise how the information content of symmetry energy gets blurred in the exploration of nuclear masses in microscopic models. For example in Ref. [76], correlation between the binding energy difference  $\Delta B$  of  $^{132}\text{Sn}$  and  $^{100}\text{Sn}$  and the  $\Delta r_{np}$  of  $^{132}\text{Sn}$  for different sets of Skyrme EDFs were studied. In principle,  $\Delta B$  ( $^{132}\text{Sn}$ ,  $^{100}\text{Sn}$ ) should contain a major contribution coming from the asymmetric part of the  $^{132}\text{Sn}$ , which in return should be related to symmetry energy and consequently to  $\Delta r_{np}$ . However, no noticeable correlation between  $\Delta B$  ( $^{132}\text{Sn}$ ,  $^{100}\text{Sn}$ ) and  $\Delta r_{np}$  was found, which is depicted in Fig. (4.2). In the present thesis work, this lack of correlation was reconciled by studying the binding energy difference between four pairs of

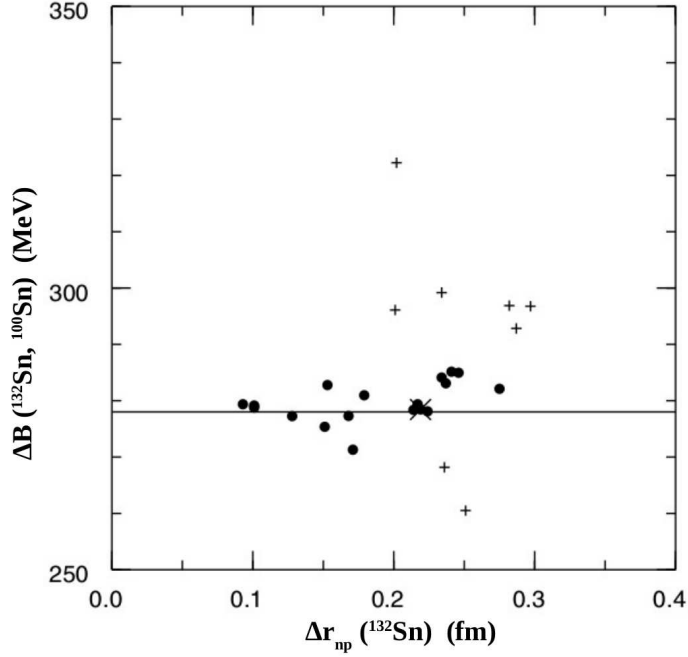


Figure 4.2: The binding energy difference  $\Delta B(^{132}\text{Sn}, ^{100}\text{Sn}) = BE(^{132}\text{Sn}) - BE(^{100}\text{Sn})$  plotted against neutron-skin thickness  $\Delta r_{np}$  of the  $^{132}\text{Sn}$  nucleus for different mean-field models as shown in Ref. [76].

nuclei in different RMF models with increasing asymmetry effects namely, ( $^{68}\text{Ni} - ^{56}\text{Ni}$ ), ( $^{132}\text{Sn} - ^{100}\text{Sn}$ ), ( $^{24}\text{O} - ^{16}\text{O}$ ) and ( $^{30}\text{Ne} - ^{18}\text{Ne}$ ). The neutron rich  $^{68}\text{Ni}$  and  $^{132}\text{Sn}$  nuclei have asymmetries  $\delta = 0.176$  and  $0.242$  respectively ( $\delta$  is the isospin asymmetry parameter  $(N - Z)/A$ );  $^{24}\text{O}$  and  $^{30}\text{Ne}$  have  $\delta \approx 0.33$  i.e.  $N/Z \approx 2$ . The Ni and Sn isotopes are doubly closed shell nuclei. So also the O-nuclei,  $^{24}\text{O}$  is recently seen to be an unexpectedly stable doubly magic nucleus [77, 78]. The Ne-nuclei have their neutron shells closed but have valence protons. The binding energy difference between the two Ne-nuclei is expected to cancel the pairing and the possible core-polarization effects arising from the two valence protons partially. In Fig.4.3 the binding energy difference between the four pairs of nuclei are plotted against  $\Delta r_{np}$  of  $^{208}\text{Pb}$ , the  $\Delta r_{np}$  and the binding energies being calculated for seven models of BSR family [49, 79], NL3 [80], FSU [50] and for seven models of

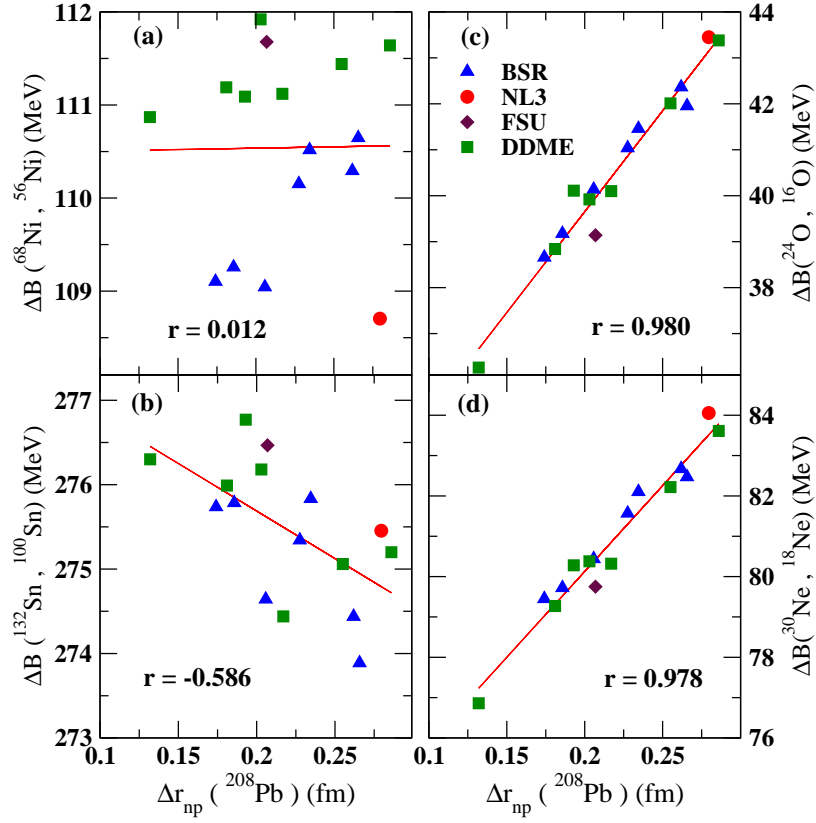


Figure 4.3: The binding energy difference  $\Delta BE(X, Y) = BE(X) - BE(Y)$  for four different pairs of isotopes are plotted against neutron-skin thickness  $\Delta r_{np}$  in the  $^{208}\text{Pb}$  nucleus for 16 different RMF models (See text for details). The values of correlation coefficients  $r$  are also displayed.

Density Dependent Meson Exchange (DDME) family [81]. The correlation coefficient for the Ni-pair is seen to be only 0.012, for the Sn-pair, it has increased to 0.586. For the O and Ne pairs, they are quite high, 0.980 and 0.978, respectively. One can not fail to notice the increasingly high correlation with increasing asymmetry, particularly for the latter two cases.

## 4.2 A Covariance analysis

The method of Covariance analysis as described in Chapter 3 provides the perfect tool to unveil the effect of extremely asymmetric nuclei to construct the model parameters of a RMF model.

### 4.2.1 Fit data and model parameters

The occurrence of strong correlation for the case of O and Ne pairs probably suggest that selective combination of suitable binding energies of nuclei of low and high isospin may be ideally suited to better constrain the isovector part of the nuclear interaction. To explore this idea, two RMF models (model-I and model-II) corresponding to different sets of fit-data are constructed. The observables explored are the symmetry energy  $C_2^0$ , symmetry energy slope  $L_0$  along with the  $\Delta r_{np}$  of  $^{208}\text{Pb}$ . The effective Lagrangian density for the RMF model employed in the present work is similar to that of the FSU one [46, 50, 82, 83] (see Chapter 2). The values of the parameters entering the EDF of the RMF model are obtained from an optimal  $\chi^2$  fit of the experimental observables with the theoretically calculated values, as described in Chapter 3. In model-I the binding energies and charge radii of some standard set of nuclei ( $^{16}\text{O}$ ,  $^{40}\text{Ca}$ ,  $^{48}\text{Ca}$ ,  $^{56}\text{Ni}$ ,  $^{68}\text{Ni}$ ,  $^{90}\text{Zr}$ ,  $^{100}\text{Sn}$ ,  $^{116}\text{Sn}$ ,  $^{132}\text{Sn}$ ,  $^{144}\text{Sm}$  and  $^{208}\text{Pb}$ ) spanning the entire periodic table are taken as fit-data. In model-II, we have the same set of experimental observables, but with the addition of the binding energy difference  $\Delta B$  of ( $^{24}\text{O}, ^{16}\text{O}$ ) and of ( $^{30}\text{Ne}, ^{18}\text{Ne}$ ). The parameters of model-I and model-II are obtained by optimizing [84] the objective function  $\chi^2(\mathbf{p})$  as described in Chapter 3.

Once the optimized parameter set is obtained the correlation coefficient between two quantities  $\mathcal{A}$  and  $\mathcal{B}$ , which may be a parameter as well as an observable, can be evaluated within the covariance analysis as described in Chapter 3. The parameters for model-I and II



Table 4.1: The best fit values for the parameters of model-I and model-II.  $m_\sigma$  is the mass of  $\sigma$  meson given in units of MeV. The masses of  $\omega$  and  $\rho$  mesons are kept fixed to  $m_\omega=782.5$  MeV and  $m_\rho=763$  MeV and nucleon mass is taken to be  $M=939$  MeV. Statistical errors on the fitted parameters are also given for both the models.

Name	$g_\sigma$	$g_\omega$	$g_\rho$	$\kappa_3$	$\kappa_4$	$\eta_{2\rho}$	$\zeta_0$	$m_\sigma$
model-I	-10.6246	13.8585	12.077	1.46285	-0.9673	28.33	5.2056	496.007
(Error)	0.246	0.662	2.60	0.275	3.66	29.9	3.21	12.2
model-II	-10.6212	13.8599	12.436	1.46223	-0.8566	32.50	5.3220	495.815
(Error)	0.149	0.262	1.54	0.290	1.53	18.1	0.099	8.23

corresponding to minimum value of the objective function  $\chi^2(\mathbf{p})$  ( $=\chi^2(\mathbf{p}_0)$ ) along with their statistical errors are listed in Table 4.1. Overall, the errors on the parameters for the case of model-II are smaller than those obtained for the model-I indicating that the inclusion of the fit data on the binding energy differences constrain the model parameters better. In particular, the errors on the parameters  $g_\rho$  and  $\eta_{2\rho}$ , which govern the isovector part of the effective Lagrangian, are smaller for the model-II. The large error on the parameters  $\kappa_3$  and  $\kappa_4$  for both the models may be due to the fact that the fit data does not include any observable which could constrain the value of the nuclear matter incompressibility coefficient [83]. In Table 4.2 different observables  $\mathcal{O}_i$ , adopted errors on them  $\Delta\mathcal{O}_i$ , their experimental values along with the results obtained for model-I and model-II using the corresponding best fit parameters are listed. The values of  $\mathcal{O}_i$  and  $\Delta\mathcal{O}_i$ , except for the  $\Delta B$  of ( $^{24}\text{O}, ^{16}\text{O}$ ) and ( $^{30}\text{Ne}, ^{18}\text{Ne}$ ) and  $r_{ch}$  of  $^{132}\text{Sn}$ , are exactly same as used in Ref. [85]. The experimental data for  $\Delta B$  of ( $^{24}\text{O}, ^{16}\text{O}$ ) and ( $^{30}\text{Ne}, ^{18}\text{Ne}$ ) are taken from [86] and that for the  $r_{ch}$  of  $^{132}\text{Sn}$  from [87].

Table 4.2: Observables  $\mathcal{O}$  of different nuclei, adopted errors on them  $\Delta\mathcal{O}$ , their experimental values and the ones obtained for model-I and II.  $BE$  and  $r_{ch}$  refers to binding energy and charge radius of a nucleus respectively, and  $\Delta B$  is binding energy difference of two isotopes of a nucleus as indicated.  $BE$  and  $\Delta B$  are in units of MeV and  $r_{ch}$  in fm.

Nucleus	$\mathcal{O}$	$\Delta\mathcal{O}$	Expt.	model-I	model-II
$^{16}\text{O}$	$BE$	4.0	127.62	$127.781\pm 0.990$	$127.783\pm 0.576$
	$r_{ch}$	0.04	2.701	$2.700\pm 0.017$	$2.699\pm 0.013$
$^{16}\text{O}, ^{24}\text{O}$	$\Delta B$	2.0	41.34	-	$40.995\pm 1.046$
$^{18}\text{Ne}, ^{30}\text{Ne}$	$\Delta B$	2.0	79.147	-	$79.149\pm 1.296$
$^{40}\text{Ca}$	$BE$	3.0	342.051	$342.929\pm 1.064$	$342.927\pm 0.927$
	$r_{ch}$	0.02	3.478	$3.457\pm 0.013$	$3.455\pm 0.010$
$^{48}\text{Ca}$	$BE$	1.0	415.99	$414.883\pm 0.720$	$414.751\pm 0.541$
	$r_{ch}$	0.04	3.479	$3.439\pm 0.007$	$3.439\pm 0.006$
$^{56}\text{Ni}$	$BE$	5.0	483.99	$483.752\pm 2.495$	$483.619\pm 1.646$
	$r_{ch}$	0.18	3.750	$3.695\pm 0.025$	$3.693\pm 0.020$
$^{68}\text{Ni}$	$BE$	1.0	590.43	$592.294\pm 0.784$	$592.162\pm 0.736$
$^{90}\text{Zr}$	$BE$	1.0	783.893	$782.855\pm 4.833$	$782.776\pm 1.621$
	$r_{ch}$	0.02	4.269	$4.267\pm 0.009$	$4.267\pm 0.034$
$^{100}\text{Sn}$	$BE$	2.0	825.8	$827.987\pm 1.753$	$827.757\pm 1.534$
$^{116}\text{Sn}$	$BE$	2.0	988.32	$987.169\pm 0.946$	$987.072\pm 0.760$
	$r_{ch}$	0.18	4.626	$4.623\pm 0.009$	$4.623\pm 0.008$
$^{132}\text{Sn}$	$BE$	1.0	1102.9	$1102.851\pm 1.146$	$1102.631\pm 0.856$
	$r_{ch}$	0.02	4.71	$4.711\pm 0.011$	$4.712\pm 0.010$
$^{144}\text{Sm}$	$BE$	2.0	1195.74	$1195.834\pm 1.240$	$1195.736\pm 1.287$
	$r_{ch}$	0.02	4.96	$4.956\pm 0.009$	$4.956\pm 0.009$
$^{208}\text{Pb}$	$BE$	1.0	1636.446	$1636.457\pm 4.301$	$1636.383\pm 0.917$
	$r_{ch}$	0.02	5.504	$5.530\pm 0.012$	$5.531\pm 0.010$

## 4.2.2 Results

The results obtained for the model-I and model-II are compared to see up to what extent the inclusion of the experimental data on the binding energy differences between the pair of O and Ne nuclei can constrain the iso-vector part of the effective Lagrangian. In Fig. 4.4(a) the covariance ellipsoids for the parameters  $g_\rho$  and  $\eta_{2\rho}$  are displayed (see Chapter 3). For these sets of parameters, the values of the symmetry energy slope parameter  $L_0$  and the  $\Delta r_{np}$  in the  $^{208}\text{Pb}$  nucleus are displayed in Fig. 4.4(b). The inclined and elongated shapes

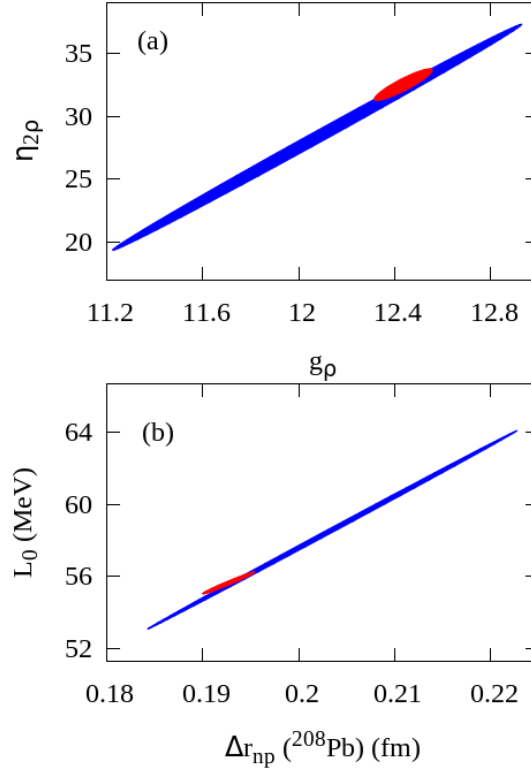


Figure 4.4: The covariance ellipsoids for the parameters  $g_\rho - \eta_{2\rho}$  (upper panel) and the corresponding  $L_0 - \Delta r_{np}$  (lower panel) for the model I (blue) and model II (red). The area inside the ellipsoids indicate the reasonable domain of the parameters.

of the ellipsoids indicate that the correlations amongst  $g_\rho - \eta_{2\rho}$  and  $L_0 - \Delta r_{np}$  are strong. In fact, the values of the correlation coefficients (Eq. (3.5)) for these pairs of quantities for both the models turn out to be  $\sim 0.95$ . It is evident that the ellipsoids depicting the results for the model-II (red) are narrower in comparison to those for the model-I (blue). This is suggestive of the fact that the inclusion of the binding energies for the  $^{24}\text{O}$  and  $^{30}\text{Ne}$  put tighter constraints on the isovector part of the effective Lagrangian density.

Nuclear matter properties for model-I and model-II are compared in Table 4.3. Errors on the entities describing the isoscalar behavior of nuclear matter ( $\mathcal{E}_0$ ,  $K_0$ ,  $\rho_0$  and  $M^*/M$ ) are pretty much the same for both the models concerned. For model-II, however, a signif-

Table 4.3: The values for the binding energy per nucleon  $\mathcal{E}_0$ , incompressibility coefficient  $K_0$ , Dirac effective mass of nucleon  $M^*/M$ , symmetry energy coefficient  $C_2^0$  and density slope parameter of symmetry energy  $L_0$  for the nuclear matter evaluated at saturation density  $\rho_0$  along with the correlated errors on them obtained within the covariance analysis for the models I and II. The results for neutron-skin thickness  $\Delta r_{np}$  in  $^{48}\text{Ca}$ ,  $^{132}\text{Sn}$  and  $^{208}\text{Pb}$  are also presented.

Observable	model-I	model-II
$\mathcal{E}_0$ (MeV)	$-16.036 \pm 0.070$	$-16.036 \pm 0.051$
$K_0$ (MeV)	$210.12 \pm 27.87$	$209.64 \pm 28.52$
$\rho_0$ ( $\text{fm}^{-3}$ )	$0.150 \pm 0.003$	$0.150 \pm 0.003$
$M^*/M$	$0.585 \pm 0.012$	$0.585 \pm 0.010$
$C_2^0$ (MeV)	$32.03 \pm 3.08$	$31.69 \pm 1.51$
$L_0$ (MeV)	$57.62 \pm 17.08$	$55.63 \pm 7.00$
$\Delta r_{np}$ ( $^{48}\text{Ca}$ ) (fm)	$0.191 \pm 0.036$	$0.187 \pm 0.016$
$\Delta r_{np}$ ( $^{132}\text{Sn}$ ) (fm)	$0.266 \pm 0.070$	$0.257 \pm 0.031$
$\Delta r_{np}$ ( $^{208}\text{Pb}$ ) (fm)	$0.201 \pm 0.065$	$0.193 \pm 0.030$

icant improvement (by a factor  $\sim 2$ ) on the spread of parameters like  $C_2^0$  and  $L_0$ , which describe the symmetry behavior of nuclear matter, is achieved over model-I. Strikingly, the errors on  $C_2^0$  and  $L_0$  for the model-II agree very well with the ones obtained for the SAMi Skyrme force [37] which includes the variational EoS for the pure neutron matter as pseudo data in the fitting protocol. We also provide the values of  $\Delta r_{np}$  for  $^{48}\text{Ca}$ ,  $^{132}\text{Sn}$  and  $^{208}\text{Pb}$  nuclei in Table 4.3. The reduction in the errors on  $\Delta r_{np}$  for the model-II in comparison to those for the model-I are in harmony with the results depicted in Fig. 4.4.

In Fig. 4.5 correlation between  $\Delta r_{np}$  of  $^{208}\text{Pb}$  and fit-data on binding energies for model-II are plotted. The stronger correlation for the data on  $\Delta B$  involving highly asymmetric nuclei ( $\delta \sim 0.33$ ) compared to others reproduces the similar features of Fig. 4.3, however, analysis being done within a single model using covariance analysis. One can notice that these correlation coefficients between  $\Delta r_{np}$  of  $^{208}\text{Pb}$  and data on  $\Delta B$  are not as high as compared to those obtained from the analysis involving several models in Fig. 4.3. Incidentally, these correlations obtained from a single model using covariance analysis and

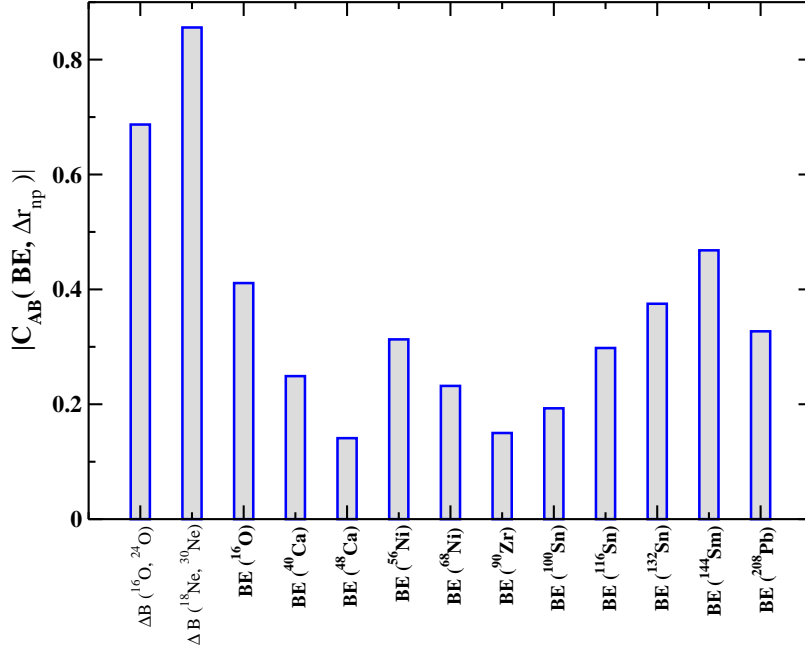


Figure 4.5: The correlation between  $\Delta r_{np}$  of  $^{208}\text{Pb}$  and different fit-data on binding energies used to obtain the model parameters of model-II.

using several models should not be compared directly. The correlation in the covariance analysis may depend on the set of data and the model parameters chosen for an analysis. The correlations depicted in Fig. 4.5 is more of an indicator that  $\Delta B$  of Oxygen and Neon pair are more sensitive to the  $\Delta r_{np}$  of  $^{208}\text{Pb}$  compared to other binding energy data used to optimize the parameters of model-II.

### 4.3 A sensitivity analysis

To analyze the sensitivity of the symmetry energy elements of nuclear matter to highly neutron rich systems as obtained in the previous section, a systematic analysis is essential. For this purpose Sensitivity analysis was employed as described in Ref. [62] (see also Chapter 3).

Table 4.4: Optimum values of the parameters for the models SINPB and SINPA, statistical errors on them are given. Mass of the  $\sigma$  meson ( $m_\sigma$ ) is given in units of MeV. The masses of  $\omega$  and  $\rho$  mesons are kept fixed to  $m_\omega=782.5$  MeV and  $m_\rho=763$  MeV and nucleon mass is taken to be  $M=939$  MeV.

Name	$g_\sigma$	$g_\omega$	$g_\rho$	$\kappa_3$	$\kappa_4$	$\eta_{2\rho}$	$\zeta_0$	$m_\sigma$
SINPB	-10.6007	13.8767	10.613	1.4868	-0.802	13.487	5.467	493.850
(Error)	0.14	0.24	1.29	0.19	1.15	12.26	0.45	4.98
SINPA	-10.6292	13.8532	12.831	1.5375	-1.190	38.179	5.363	495.394
(Error)	0.16	0.33	0.82	0.06	0.47	11.92	0.45	3.86

### 4.3.1 The RMF models SINPB and SINPA

Two different RMF models are constructed namely, SINPB and SINPA with an expanded data set compared to those in model-I and model-II in the previous section. A comparative study on the nuclear matter properties of these two models is executed in detail. In SINPB binding energies ( $BE$ ) and charge radii ( $r_{ch}$ ) of some standard set of nuclei across the whole nuclear chart are taken as fit-data (see Tab. 4.5). The binding energies of  $^{54}\text{Ca}$ ,  $^{78}\text{Ni}$  and  $^{138}\text{Sn}$  nuclei having somewhat larger asymmetry ( $\delta \sim 0.26 - 0.28$ ) are also included in the fitting protocol. The model SINPA includes some highly asymmetric nuclei, namely,  $^{24}\text{O}$ ,  $^{30}\text{Ne}$ ,  $^{36}\text{Mg}$  and  $^{58}\text{Ca}$  ( $\delta > 0.3$ ) in addition to the data set used in the base model SINPB. SINPA also contains the symmetric  $^{20}\text{Ne}$  and  $^{24}\text{Mg}$  nuclei and the observed maximum mass of neutron star  $M_{max}^{NS}$  as fit-data.

In Table 4.4, the optimal values of the parameters  $\mathbf{p}_0$  for SINPB and SINPA are given along with the errors on them. respectively. One can observe that the errors on the parameters  $g_\rho$ ,  $\kappa_3$ ,  $\kappa_4$  and  $m_\sigma$  decreased by a noticeable amount in SINPA in comparison to SINPB. For the parameters  $g_\sigma$ ,  $\zeta_0$  and  $\eta_{2\rho}$  the errors are almost the same for both the models and for the case of  $g_\omega$  its value is slightly higher in SINPA than in SINPB. The pairing is treated within the BCS approximation with cut-off energy in pairing space taken

as  $\hbar\omega_0 = 41A^{-1/3}$  MeV. The BCS pairing strengths for neutron and proton for the models SINPB and SINPA were kept fixed to  $G_n = 20/A$  and  $G_p = 25/A$ . The neutron and proton pairing gaps ( $\Delta_n, \Delta_p$ ) in MeV for the neutron rich nuclei are  $^{30}\text{Ne}$  (0.0, 2.3),  $^{36}\text{Mg}$  (2.5, 2.0),  $^{54}\text{Ca}$  (1.1, 0.0),  $^{58}\text{Ca}$  (1.0, 0.0),  $^{138}\text{Sn}$  (1.3, 0.0). The pairing gaps for other non-magic nuclei are close to  $12/\sqrt{A}$  MeV. The neutron pairing gap for  $^{24}\text{O}$  practically vanishes, since, the first unoccupied  $1d_{3/2}$  orbit is about 4.5 MeV above the completely filled  $2s_{1/2}$  orbit [88].

In Table 4.5 different observables  $\mathcal{O}$  pertaining to finite nuclei and neutron star, their experimental values, their obtained values from SINPB and SINPA along with  $\Delta\mathcal{O}$ , the adopted errors on them are listed. The experimental values of binding energies of all the nuclei except for  $^{54}\text{Ca}$  used in the fit are taken from the latest compilation AME-2012 [89]. Recently, binding energy of  $^{54}\text{Ca}$  was measured very accurately at TRIUMF [90] and CERN [91]. For this present calculation, the experimental value of the binding energy for  $^{54}\text{Ca}$  is taken from Ref. [91]. Experimental values for the charge radii used in the fit are obtained from the compilation by Angeli and Marinova [87]. For the optimization of SINPA, observed maximum mass of neutron star  $M_{max}^{NS}$  is taken from Ref. [19, 20]. It may be pointed out that, experimental value for some of the fit data are little different in the present calculation in comparison to the previous section. Except for  $^{68}\text{Ni}$ ,  $\Delta\mathcal{O}$  for all the fit-data common to both the models SINPB and SINPA are taken from Ref. [85]. As the obtained value of binding energy of  $^{68}\text{Ni}$  from both the models SINPB and SINPA deviate by more than 2 MeV from its experimental value, demanding too much accuracy on that particular datum costs a larger amount in total  $\chi^2$  compared to other data points. For this reason  $\Delta\mathcal{O} = 2$  was taken MeV for the binding energy of  $^{68}\text{Ni}$  unlike in Ref.[85], where  $\Delta\mathcal{O} = 1$  MeV. Calculated errors on the binding energies and charge radii due to uncertainties in the model parameters for the fitted nuclei for both the models SINPB and

Table 4.5: Various observables  $\mathcal{O}$ , adopted errors on them  $\Delta\mathcal{O}$ , corresponding experimental data (Expt.) and their best-fit values for SINPB and SINPA.  $BE$  and  $r_{ch}$  corresponds to binding energy and charge radius of a nucleus, respectively and  $M_{max}^{NS}$  is the maximum mass of neutron star (NS). Values of  $BE$  are given in units of MeV and  $r_{ch}$  in fm.  $M_{max}^{NS}$  is in units of Solar Mass ( $M_{\odot}$ ).

	$\mathcal{O}$	$\Delta\mathcal{O}$	Expt.	SINPB	SINPA
$^{16}\text{O}$	$BE$	4.0	127.62	127.78	128.35
	$r_{ch}$	0.04	2.699	2.704	2.696
$^{24}\text{O}$	$BE$	2.0	168.96	-	169.28
$^{20}\text{Ne}$	$BE$	4.0	160.64	-	155.89
$^{30}\text{Ne}$	$BE$	3.0	211.29	-	214.37
$^{24}\text{Mg}$	$BE$	3.0	198.26	-	195.87
$^{36}\text{Mg}$	$BE$	2.0	260.78	-	261.68
$^{40}\text{Ca}$	$BE$	3.0	342.05	343.19	343.66
	$r_{ch}$	0.02	3.478	3.460	3.452
$^{48}\text{Ca}$	$BE$	1.0	416.00	415.27	415.47
	$r_{ch}$	0.04	3.477	3.437	3.437
$^{54}\text{Ca}$	$BE$	2.0	445.37	445.63	443.79
$^{58}\text{Ca}$	$BE$	2.0	454.43	-	456.33
$^{56}\text{Ni}$	$BE$	5.0	483.99	483.38	484.34
	$r_{ch}$	0.18	3.750	3.700	3.686
$^{68}\text{Ni}$	$BE$	2.0	590.41	592.86	592.97
$^{78}\text{Ni}$	$BE$	2.0	641.78	642.10	641.59
$^{90}\text{Zr}$	$BE$	1.0	783.90	783.02	783.20
	$r_{ch}$	0.02	4.269	4.266	4.264
$^{100}\text{Sn}$	$BE$	2.0	825.30	828.11	827.93
$^{116}\text{Sn}$	$BE$	2.0	988.68	987.45	987.32
	$r_{ch}$	0.18	4.625	4.620	4.622
$^{132}\text{Sn}$	$BE$	1.0	1102.84	1103.28	1103.40
	$r_{ch}$	0.02	4.709	4.706	4.710
$^{138}\text{Sn}$	$BE$	2.0	1119.59	1118.65	1117.05
$^{144}\text{Sm}$	$BE$	2.0	1195.73	1196.00	1195.67
	$r_{ch}$	0.02	4.952	4.955	4.955
$^{208}\text{Pb}$	$BE$	1.0	1636.43	1636.38	1636.57
	$r_{ch}$	0.02	5.501	5.528	5.530
NS	$M_{max}^{NS}$	0.04	2.01	-	1.98



SINPA lie within the range from 0.51 - 1.89 MeV and 0.005 - 0.016 fm, respectively. In model SINPA the obtained maximum neutron star mass  $M_{max}^{NS}$  ( $1.98 \pm 0.03 M_{\odot}$ ) compares well with the observed value. It should be noted that the two isotopes of Mg nuclei used in the optimization of SINPA are deformed. The numerical computation is done with 20 oscillator shells being taken as the basis states for the nucleons. The quadrupole deformation parameter  $\beta_2$  calculated from SINPA for  $^{24}\text{Mg}$  and  $^{36}\text{Mg}$  nuclei are found to be 0.47 and 0.37, respectively.

### 4.3.2 Results for SINPB and SINPA

Energy per nucleon  $\mathcal{E}(\rho, 0)$  for symmetric nuclear matter (SNM) can be expressed in terms of model parameters as (see Chapter 2),

$$\begin{aligned} \mathcal{E}(\rho, 0) = & \frac{2}{\pi^2} \int_0^{k_F} dk k^2 \sqrt{k^2 + M^{*2}} \\ & + \frac{1}{2} m_{\sigma}^2 \sigma^2 + \frac{\kappa_3}{6M} g_{\sigma} m_{\sigma}^2 \sigma^3 + \frac{\kappa_4}{24M^2} g_{\sigma}^2 m_{\sigma}^2 \sigma^4 \\ & - \frac{1}{2} m_{\omega}^2 \omega^2 - \frac{1}{24} \zeta_0 g_{\omega}^2 \omega^4, \end{aligned} \quad (4.1)$$

and,  $C_2(\rho)$  is expressed as,

$$C_2(\rho) = \frac{k_F^2}{6(k_F^2 + M^{*2})^{1/2}} + \frac{g_{\rho}^2}{12\pi^2} \frac{k_F^3}{m_{\rho}^{*2}}. \quad (4.2)$$

Here,  $k_F$  is the nucleon Fermi momentum in symmetric nuclear matter at density  $\rho$  ( $= \frac{2k_F^3}{3\pi^2}$ ). The Dirac effective mass of nucleon  $M^*$  is given by  $M^* = M - g_{\sigma}\sigma$  and, the effective

Table 4.6: Different nuclear matter properties: the binding energy per nucleon for symmetric matter  $\mathcal{E}_0$ , incompressibility coefficient  $K_0$ , Dirac effective mass of nucleon  $M_0^*$  (scaled by nucleon mass  $M$ ), symmetry energy coefficient  $C_2^0$  and density slope parameter of symmetry energy  $L_0$  for the nuclear matter evaluated at saturation density  $\rho_0$  along with the correlated errors on them for the models SINPB and SINPA. The values of  $C_2(\rho_c)$  and  $L(\rho_c)$  calculated at crossing density  $\rho_c$  along with the neutron skin  $\Delta r_{np}$  in  $^{208}\text{Pb}$  are also presented for these two models.

Observable	SINPB	SINPA
$\mathcal{E}_0$ (MeV)	$-16.04 \pm 0.06$	$-16.00 \pm 0.05$
$K_0$ (MeV)	$206 \pm 20$	$203 \pm 6$
$\rho_0$ ( $\text{fm}^{-3}$ )	$0.150 \pm 0.002$	$0.151 \pm 0.001$
$M_0^*/M$	$0.59 \pm 0.01$	$0.58 \pm 0.01$
$C_2^0$ (MeV)	$33.95 \pm 2.41$	$31.20 \pm 1.11$
$C_2(\rho_c)$ (MeV)	$26.08 \pm 0.41$	$25.60 \pm 0.51$
$L_0$ (MeV)	$71.55 \pm 18.89$	$53.86 \pm 4.66$
$L(\rho_c)$ (MeV)	$55.98 \pm 13.78$	$38.47 \pm 5.43$
$\Delta r_{np}$ ( $^{208}\text{Pb}$ ) (fm)	$0.241 \pm 0.040$	$0.183 \pm 0.022$

mass of  $\rho$  meson,  $m_\rho^*$  is expressed as [92],

$$m_\rho^{*2} = m_\rho^2 \left( 1 + \frac{1}{2M^2} \eta_{2\rho} g_\omega^2 \omega^2 \right). \quad (4.3)$$

From Eq. (4.2) one can see that, the kinetic part of  $C_2(\rho)$  depends on the effective mass of nucleon  $M^*$ , which has dependence on the parameter  $g_\sigma$  and the field value of  $\sigma$ . However, the interaction part of  $C_2(\rho)$  mainly depends on the isovector parameters  $g_\rho$  and  $\eta_{2\rho}$ .

Once the objective functions for the models SINPB and SINPA are optimized, different nuclear matter properties can be extracted from them and compared. In Table 4.6 values of different nuclear matter parameters along with the corresponding errors evaluated within the covariance analysis are listed for SINPB and SINPA. The properties associated with symmetric nuclear matter are evaluated at the saturation density  $\rho_0$ , while, those characterizing the asymmetric nuclear matter are evaluated at  $\rho_0$  and the crossing-density  $\rho_c$  which

is taken as  $\frac{0.11}{0.16} \times \rho_0$  [93]. Errors on binding energy per nucleon  $\mathcal{E}_0 (= \mathcal{E}(\rho_0, 0))$ , saturation density  $\rho_0$  and Dirac effective mass of nucleon  $M_0^*/M (=M^*(\rho_0)/M)$  are pretty much the same for both the models concerned. However, a noticeable improvement is observed for the model SINPA over SINPB for the calculated errors on the symmetry energy parameters  $C_2^0 (=C_2(\rho_0))$ ,  $L_0 (=L(\rho_0))$  and  $L(\rho_c)$ . The refinement in the error in SINPA in comparison to SINPB is also to be noted for the incompressibility coefficient at saturation density,  $K_0$ . Error on the neutron-skin  $\Delta r_{np}$  in  $^{208}\text{Pb}$  also reduces by almost a factor of 2 in SINPA in comparison to SINPB. The central values of  $L_0$  and  $\Delta r_{np}$  of  $^{208}\text{Pb}$  obtained for the model SINPB are seen to differ from those obtained from the model-I of previous section; this can be attributed to the differences in the adopted error on the binding energy of  $^{68}\text{Ni}$  and to the differences in some of the experimental fit data.

The observation of improved constraint in the symmetry elements calculated from model SINPA over those from SINPB clearly indicates that the additional data of four highly asymmetric nuclei ( $^{24}\text{O}$ ,  $^{30}\text{Ne}$ ,  $^{36}\text{Mg}$  and  $^{58}\text{Ca}$ ) with  $\delta > 0.3$  and the observed maximum mass of neutron star  $M_{max}^{NS}$  contain more distilled information on isovector elements in the nuclear interaction. It is striking to note that the addition of the binding energies of  $^{54}\text{Ca}$ ,  $^{78}\text{Ni}$  and  $^{138}\text{Sn}$  ( $\delta \sim 0.26-0.28$ ) as fit data in the optimization of the model SINPB did not improve the uncertainties in the symmetry energy parameters as compared to those for the model-I in the previous section. On the other hand, inclusion of highly asymmetric ( $\delta > 0.3$ )  $^{36}\text{Mg}$  and  $^{58}\text{Ca}$  nuclei in the fitting protocol of the model SINPA yields smaller uncertainties in the symmetry energy parameters in comparison to the model-II of previous section which does not include these nuclei. This clearly emphasizes that the binding energies of nuclei with  $\delta > 0.3$  play a crucial role in constraining the symmetry energy parameters and is thus a pointer to the necessity of taking data for very asymmetric nuclei in the optimization of the RMF model. In the next section we are going to analyze this

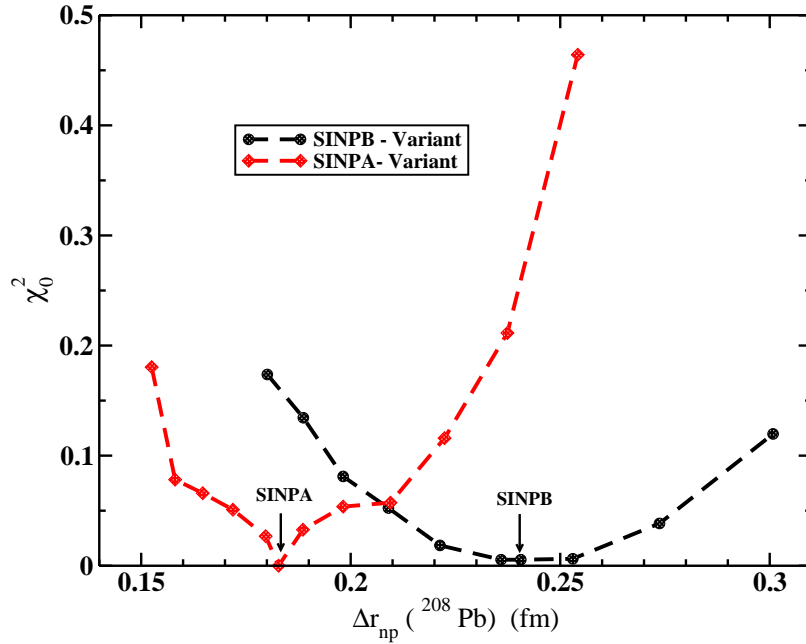


Figure 4.6: Optimum values of the objective function ( $\chi_0^2$ ) are plotted as a function of  $\Delta r_{np}$  (neutron skin of  $^{208}\text{Pb}$ ) for two families of models, namely, SINPB-Variant and SINPA-Variant (see text for details).

more critically.

Now the sensitivity of symmetry energy parameters to the properties of the neutron rich systems are discussed in detail. Before embarking on the analysis in terms of sensitivity matrix (see Chapter 3), we make a simple examination of the results. We look into the dependence of the optimal value of the objective function on the neutron skin of  $^{208}\text{Pb}$ . Fixing  $\eta_{2\rho}$  to a preset value and optimizing the  $\chi^2$  function by adjusting the rest of the model parameters, one can get a particular value of  $\Delta r_{np}$  of  $^{208}\text{Pb}$  for the models SINPB and SINPA [94]. Two families of RMF models so constructed are called SINPB-Variant and SINPA-Variant. Different input values of  $\eta_{2\rho}$  would yield different  $\Delta r_{np}$  in both these models. In Fig. 4.6 optimal values of the objective function  $\chi^2$  (i.e.  $\chi_0^2$ ) for these two models are displayed as a function of  $\Delta r_{np}$  of  $^{208}\text{Pb}$ ; the values of  $\chi_0^2$  are so adjusted that their minimum value within a family vanishes. Visual comparison of results from the two

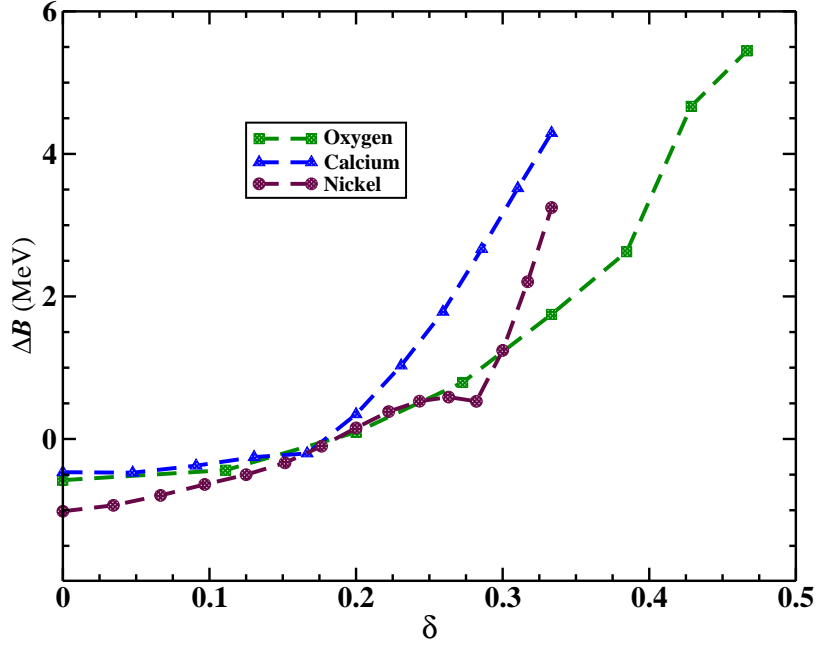


Figure 4.7: Binding energy differences  $\Delta B (=BE(\text{SINPB}) - BE(\text{SINPA}))$  extracted using models SINPB and SINPA for even isotopes of O, Ca and Ni nuclei plotted as a function of asymmetry  $\delta$ .

families of models shows that there is a stronger preference to a particular value of  $\Delta r_{np}$  of  $^{208}\text{Pb}$  in the SINPA-Variant family. It is worthwhile to mention that, SINPB-Variant family has  $^{54}\text{Ca}$ ,  $^{78}\text{Ni}$  and  $^{138}\text{Sn}$  in the fitted data set where asymmetry  $\delta \sim 0.26 - 0.28$ . The  $\chi_0^2$  function is still rather flat, making it tenuous to give a reasonable bound on the value of  $\Delta r_{np}$  of  $^{208}\text{Pb}$ . The role of ultra neutron-rich nuclei in the SINPA-Variant family where nuclei with  $\delta > 0.3$  (e.g.  $^{24}\text{O}$ ,  $^{30}\text{Ne}$ ,  $^{36}\text{Mg}$ ,  $^{58}\text{Ca}$ ) are further included in the fitting protocol are eminently evident in Fig 4.6. As  $\Delta r_{np}$  of  $^{208}\text{Pb}$  is correlated to  $L_0$  [12, 15], one finds a tighter constraint on  $L_0$  as well from SINPA as compared to SINPB (see Tab. 4.6).

The two Variant families so constructed from selective optimization of the parameter set  $\mathbf{p}_0$  keeping  $\Delta r_{np}$  of  $^{208}\text{Pb}$  fixed should affect the calculated binding energies. In Fig. 4.7 binding energy differences of three isotopic chains of O, Ca and Ni extracted from models SINPB and SINPA ( $\Delta r_{np}(^{208}\text{Pb}) = 0.241$  fm and 0.183 fm, respectively at absolute

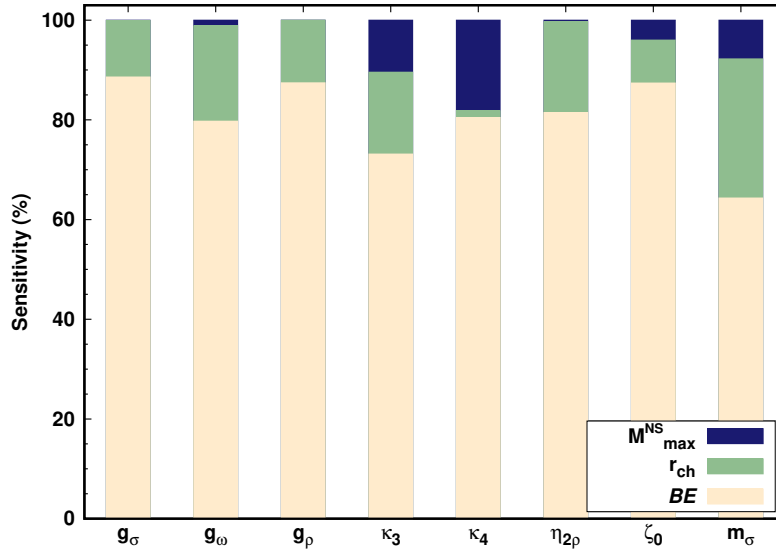


Figure 4.8: Relative sensitivity of different parameters of the effective Lagrangian density to three groups of fit data used in optimization of SINPA. These groups are nuclear binding energies ( $BE$ ), charge radii ( $r_{ch}$ ) and maximum mass of neutron star ( $M_{max}^{NS}$ ).

minima of  $\chi_0^2$ , see Fig. 4.6) are plotted as a function of asymmetry  $\delta$ . The differences in the binding energies so calculated for all the isotopic chains show significant enhancement when one goes from  $\delta$  just below 0.3 to higher values [88]. Nuclei beyond  $\delta = 0.3$  thus show a high sensitivity towards  $\Delta r_{np}$  of  $^{208}\text{Pb}$ . Several experimental efforts are being made to accurately measure binding energies of these exotic nuclei. These measurements may impose very tight constraint on the value of  $\Delta r_{np}$  of  $^{208}\text{Pb}$ .

Further, the sensitivity analysis based on a sensitivity matrix was employed in model SINPA to understand the impact of the new fit-data considered to optimize it (see Chapter 3). In Fig. 4.8 the relative sensitivity of different parameters of the effective Lagrangian density to three broad data-types (binding energies  $BE$ , charge radii  $r_{ch}$  of finite nuclei and maximum mass of neutron star  $M_{max}^{NS}$ ) are displayed. It is evident that all the parameters are maximally sensitive ( $>65\%$ ) to the binding energies of nuclei. The higher relative sensitivity of the parameters to the binding energies of nuclei can be attributed partly to

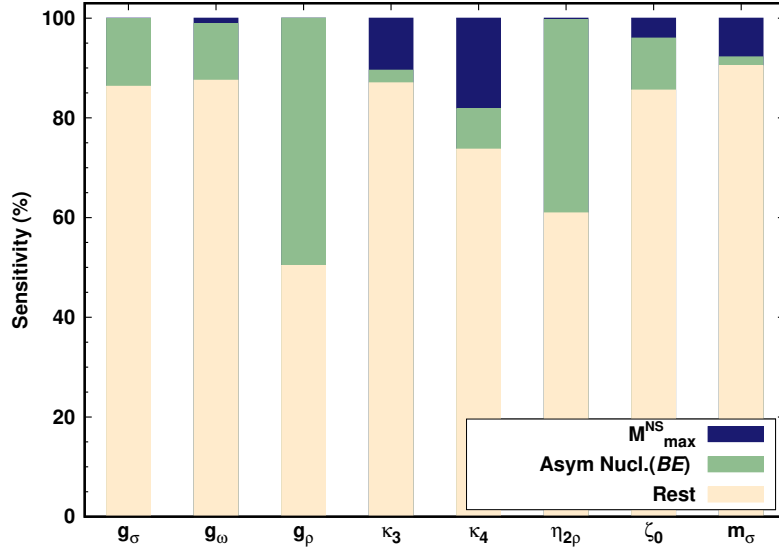


Figure 4.9: Same as Fig. 4.8, but, with different grouping of the fit data of finite nuclei. One group contains binding energies of highly asymmetric nuclei ( $^{24}\text{O}$ ,  $^{30}\text{Ne}$ ,  $^{36}\text{Mg}$  and  $^{58}\text{Ca}$ ) and another contains remaining fit data on the finite nuclei.

their large number used in the fit. The parameter  $\kappa_4$  shows almost no sensitivity towards the charge radii. The parameters  $\kappa_3$ ,  $\kappa_4$  and  $m_\sigma$  are seen to be appreciably sensitive to the single data of neutron star  $M_{max}^{NS}$  as they have a crucial role in the determination of the high density behavior of the nuclear EoS which in turn governs the value of  $M_{max}^{NS}$ .

In Fig. 4.9 the analysis was performed by regrouping the data on binding energies and charge radii so that the sensitivity of the RMF model parameters to the binding energies of highly asymmetric nuclei can be assessed. One of the group consists of only the binding energies of  $^{24}\text{O}$ ,  $^{30}\text{Ne}$ ,  $^{36}\text{Mg}$  and  $^{58}\text{Ca}$  nuclei, while the other group contains the remaining data on the finite nuclei. One can not fail to notice that, the parameters  $g_\rho$  and  $\eta_{2\rho}$ , which control the isovector part of the effective Lagrangian, are relatively more sensitive ( $\sim 40\%$ ) to the binding energies of highly asymmetric nuclei. The sensitivity of  $g_\rho$  and  $\eta_{2\rho}$  to the value of  $M_{max}^{NS}$  is not observed in Figs. 4.8 and 4.9 partly because  $M_{max}^{NS}$  is a single datum, but mainly because it is overshadowed by the relative contributions to the sensitivity from

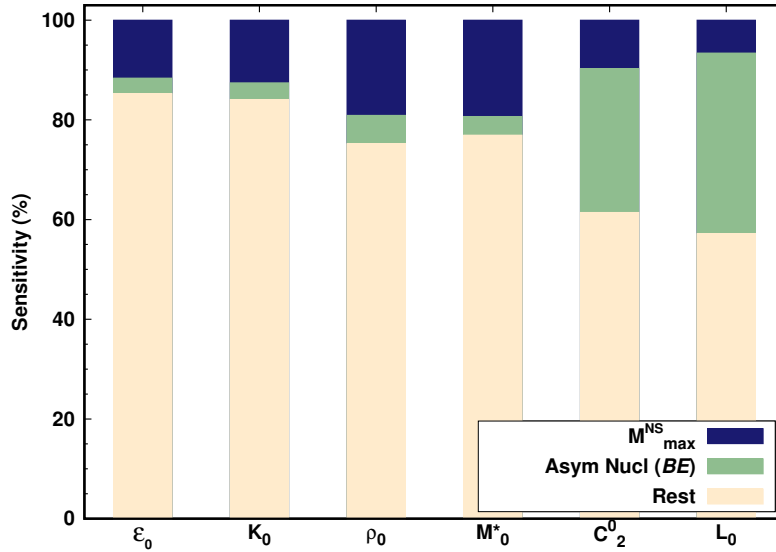


Figure 4.10: Relative sensitivity of the nuclear matter properties at saturation density to the fit data of SINPA with the same grouping as in Fig. 4.9.

the binding energies of asymmetric nuclei.

In Fig. 4.10 the sensitivity of different empirical data pertaining to the saturation density  $\rho_0$  of nuclear matter are displayed to the data-set used in the optimization of the model SINPA. To do so, the same grouping of data was used as in Fig. 4.9. Since the parameters  $g_\sigma$ ,  $g_\omega$  etc. of the effective Lagrangian are optimally determined from the full data set, it is no wonder that the empirical nuclear matter data obtained from the energy density functional are maximally sensitive to the group of fit data "Rest", as it contains the largest number of data elements. The high sensitivity of  $C^0_2$  ( $\sim 30\%$ ) and  $L_0$  ( $\sim 40\%$ ) to the binding energies of the highly asymmetric  $^{24}\text{O}$ ,  $^{30}\text{Ne}$ ,  $^{36}\text{Mg}$  and  $^{58}\text{Ca}$  nuclei, which form a very small subset of the data-set used in the optimization of SINPA (4 out of 30) is a reflection of the high sensitivity of the model parameters  $g_\rho$  and  $\eta_{2\rho}$  to the masses of these highly asymmetric nuclei as seen earlier in Fig. 4.9. Appreciable sensitivity of all the nuclear matter properties to the single data on neutron star  $M_{max}^{NS}$  can not also be missed either. Accurate



knowledge of  $M_{max}^{NS}$  is required for the precision determination of the EDF involving high densities beyond saturation, any small change in it thus may result in large change in the value of the nuclear matter properties ( $\mathcal{E}_0, K_0, \rho_0, M_0^*$ ) calculated from the EDF. This can be appreciated from the sensitivity of  $\kappa_3, \kappa_4$  and partly  $\zeta_0$  (governing the scalar mass and the number density) on  $M_{max}^{NS}$  displayed in Fig. 4.9. The not-too-insignificant sensitivity of  $C_2^0$  and  $L_0$  to  $M_{max}^{NS}$  demands attention. It stems from the dependence of the kinetic part of  $C_2(\rho)$  on  $M^*$  (Eq. (4.2)) whose value at saturation density is found appreciably sensitive to the maximum mass of neutron star. The value of  $\sigma$ -field determining the effective mass of nucleon depends on the coupling constants  $g_\sigma, \kappa_3, \kappa_4$  and the value of  $m_\sigma$ . High sensitivity of these coupling constants to  $M_{max}^{NS}$  (see Figs. 4.8 and 4.9) gets reflected in the sensitivity analysis of the symmetry energy parameters to  $M_{max}^{NS}$ .

### 4.3.3 Nuclear Matter properties at high density

The calculation of nuclear matter properties with both the models SINPB and SINPA were extended for densities beyond saturation. This provides valuable informations to construct theories for dense nuclear systems viz. neutron star and several other astrophysical objects from EoS so constrained at saturation density. In Fig. 4.11 different nuclear matter properties, e.g. binding energy per nucleon for symmetric matter  $\mathcal{E}$  (Fig. 4.11(a)), symmetry energy coefficient  $C_2$  (Fig 4.11(b)) and its density derivative  $L$  (Fig. 4.11(c)) were plotted as a function of density  $\rho/\rho_0$  for the models SINPB (turquoise) and SINPA (black-pattern) along with their associated errors. The errors are calculated within the covariance analysis. The energy per nucleon  $\mathcal{E}$  in the explored density region for SINPB and SINPA are almost identical as seen from Fig. 4.11(a). Most stringent constraint on the values of  $\mathcal{E}$  appear at  $\rho \sim \rho_0$  for both the models and they grow as one moves away from  $\rho_0$  [95]. In Fig. 4.11(b)

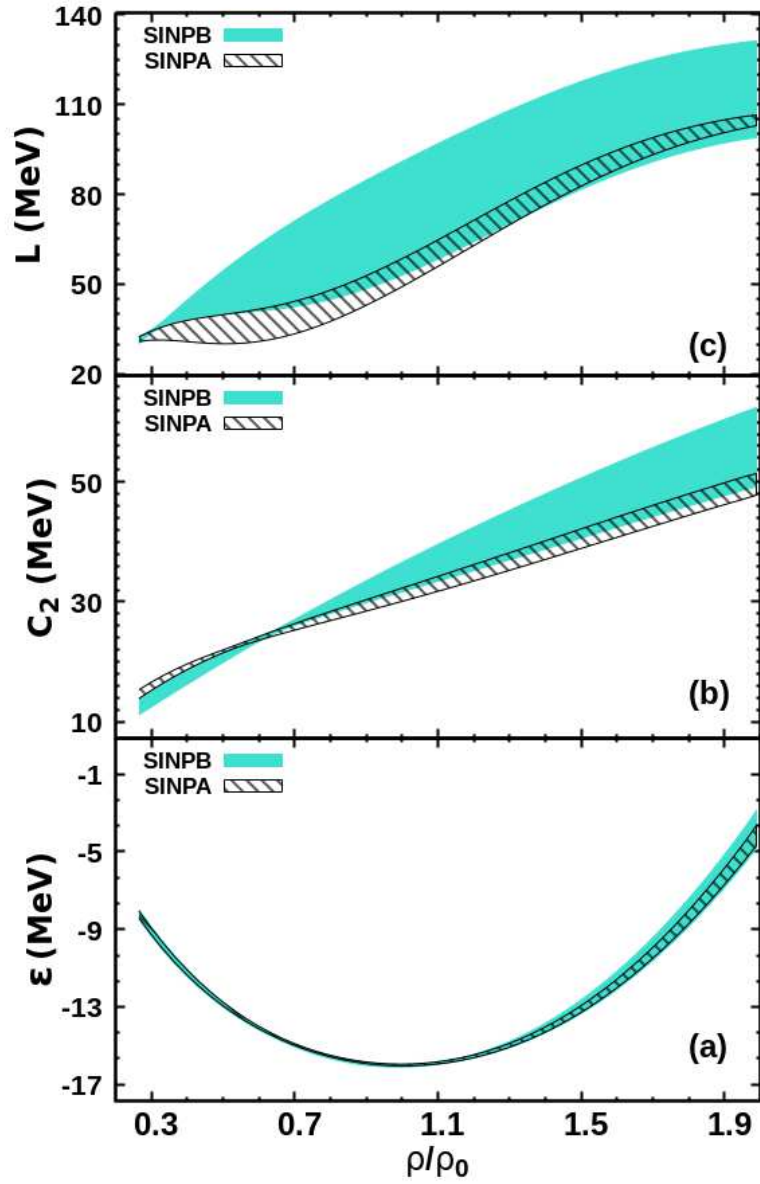


Figure 4.11: Binding energy per nucleon for symmetric matter  $\mathcal{E}$ , symmetry energy parameter  $C_2$  and its density derivative  $L$  along with their errors as a function of density  $\rho/\rho_0$  for SINPB and SINPA.

allowed regions of  $C_2$  show similar trend for SINPB and SINPA, both of them having their minimum variance at  $\rho \sim 0.7\rho_0$  [96]. However, a significant improvement is observed over the errors on  $C_2$  for SINPA in comparison to SINPB at higher densities. Comparison of calculated electric dipole polarizability of  $^{208}\text{Pb}$  from several Skyrme and RMF interactions with the corresponding experimental data recently yielded a very tightly constrained value of  $C_2$  at density  $\rho_0/3$ ,  $C_2(\rho_0/3) = 15.91 \pm 0.99$  MeV [97]. It is interesting to note that the model SINPB has overlap with this constraint at the lower end,  $C_2(\rho_0/3) = 13.69 - 16.31$  MeV, whereas SINPA agrees with this result at the higher end,  $C_2(\rho_0/3) = 16.41 - 17.67$  MeV.

In Fig. 4.11(c) a curious behavior in the variance of  $L$  with density was observed. For the model SINPB, the variance in  $L$  grows up to a certain density  $\sim \rho_0$  and from there onwards it remained almost constant all the way up to  $2\rho_0$ . In contrast, in SINPA error on  $L$  grows only up to  $\rho \sim 0.7\rho_0$  and shows a monotonically decreasing trend afterwards. This particular result may appear intriguing. A model primarily obtained by fitting some ground state properties of finite nuclei, where concerned central density is  $\sim \rho_0$  and average density is  $\sim 0.7\rho_0$  is not normally expected to show better constraint on nuclear matter properties at ultra-saturation densities. To investigate this, the expression of  $C_2$  as a function of density given in Eq. (4.2) was recalled.  $C_2$  has a dependence on  $m_\rho^{*2}$ , the square of the effective mass of  $\rho$  meson. The density variation of  $m_\rho^{*2}$  for both the models are displayed in Fig. 4.12. A rapid difference in the value of  $m_\rho^{*2}$  (scaled by  $10^5$ ) calculated in models SINPA and SINPB builds up with increasing density. As the value of the parameter  $\eta_{2\rho}$  is much larger in SINPA (38.18) compared to that in SINPB (13.49) [see Table 4.4], at high densities the second term in the expression of  $C_2$  (Eq. (4.2)) gets diluted due to  $m_\rho^{*2}$  (Eq. (4.3)) by a much greater rate for the model SINPA in comparison to SINPB. This explains why the error on  $C_2$  grows at much faster rate in SINPB than in SINPA. Now, if

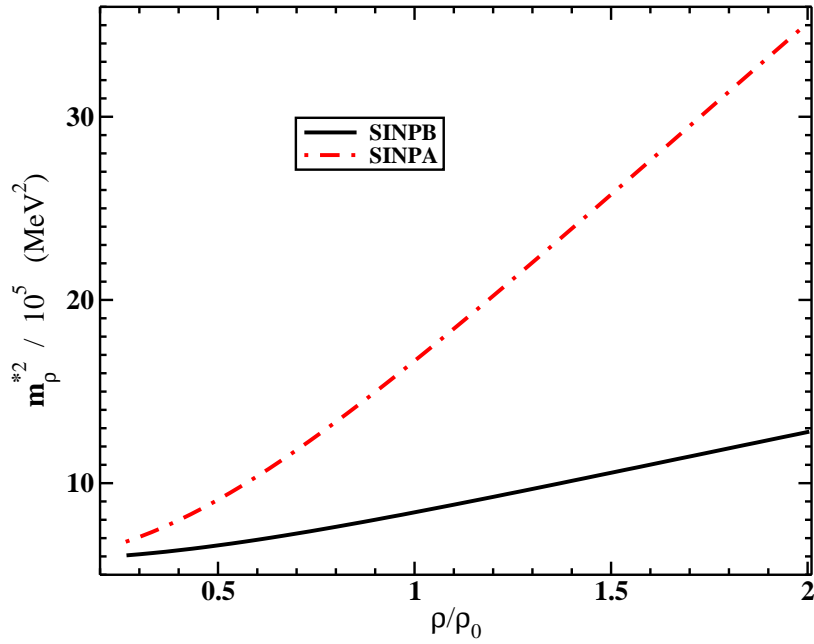


Figure 4.12: Square of the effective mass of  $\rho$  meson (scaled by  $10^5$ ) as a function of density  $\rho/\rho_0$  plotted for SINPB and SINPA.

one takes density derivative of  $C_2$ , the second term in Eq. (4.2) gives rise to two terms with  $\eta_{2\rho}$  in the denominator for the expression of  $L$  as a function of density due to varying  $\omega$  field value. That is why  $\eta_{2\rho}$  becomes a very crucial factor for the values of  $L$  at higher densities. This fact explains why in SINPA error on  $L$  decreases at higher densities, whereas in SINPB it remains almost constant as shown in Fig. 4.11(c).

## 4.4 Summary

To sum up, an investigation is made on the extraction of the precision information from experimental data on the isovector content of the nuclear interaction and their observable derivatives like the symmetry energy of nuclear matter and its density slope  $L_0$  at saturation density. The relativistic mean field model is chosen as the framework for the realization of this goal. A comparative study of the covariance analysis of the interaction strengths and

the symmetry observables ( $C_2^0$ ,  $L_0$ ,  $\Delta r_{np}$  of  $^{208}\text{Pb}$ ) made with two sets of models: (I) with model-I and SINPB (these included in the fit data observables from nearly symmetric and few asymmetric nuclei); (II) with model-II and SINPA (which included further data from extremely asymmetric nuclei right at the edge of neutron drip line with neutron to proton ratio  $\sim 2$  and the observed maximum mass  $M_{max}^{NS}$  of neutron star for SINPA) shows that the nuclear symmetry energy properties and the neutron skin thickness  $\Delta r_{np}$  of  $^{208}\text{Pb}$  are determined in much narrower constraints from the latter set of models. This is a pointer to the necessity of inclusion of extremely neutron-rich systems in any data analysis for filtering out information on isovector entities in the nuclear interaction. The conclusion is further reinforced from the sensitivity analysis of the different model parameters of SINPA entering the nuclear effective interaction to the experimental data set taken for such an analysis.

---

# MODEL DEPENDENCE IN THE SYMMETRY ENERGY PARAMETERS

---

## 5.1 Introduction

The macroscopic nuclear droplet model (DM) given by Myers and Swiatecki [3, 4] suggests that various symmetry energy parameters and the neutron-skin thickness in a heavy nucleus are related to one another. The neutron skin thickness is defined as the difference between the rms radii for the density distributions of the neutrons and protons in the nucleus:

$$\Delta r_{\text{np}} \equiv \langle r^2 \rangle_n^{1/2} - \langle r^2 \rangle_p^{1/2}. \quad (5.1)$$

Nuclear mean-field models predict a nearly linear correlation of  $\Delta r_{\text{np}}$  of a heavy nucleus such as  $^{208}\text{Pb}$  with the slope of the equation of state of neutron matter at a subsaturation density around  $0.1 \text{ fm}^{-3}$  [76, 98], with the density derivative of the symmetry energy  $L_0$  [12, 15, 99–103], and with the surface symmetry energy in a finite nucleus [15, 101, 104].

The correlation of a finite nucleus property such as  $\Delta r_{\text{np}}$  with a bulk property of infinite nuclear matter such as  $L_0$  can be interpreted as basically due to the dependence of  $\Delta r_{\text{np}}$  on the surface symmetry energy. In a local density approximation the surface symmetry energy can be correlated with  $L_0$ , and this fact therefore implies the correlation between  $\Delta r_{\text{np}}$  and  $L_0$ . Macroscopic approaches such as the DM [3, 4] often provide insightful guidance into the global features of many of these correlations [15, 100, 105].

Hadronic probes based on strong interaction, measure the  $\Delta r_{\text{np}}$  of  $^{208}\text{Pb}$  with fair accuracy [106–111]. However, being immensely dependent on the formulation of the strong interaction, these measurements are heavily model dependent. The Lead Radius Experiment (PREX) [5, 6] based on parity violating electron scattering [7], provides the most model independent measurement of  $\Delta r_{\text{np}}$  of  $^{208}\text{Pb}$  with fair accuracy. Ongoing efforts are underway to perform an accurate and model independent measurement of the neutron-skin thickness in the  $^{208}\text{Pb}$  nucleus [112]. At the same time, it may not be straightforward for theory to extract various symmetry energy parameters from the neutron-skin thickness in a model-independent fashion.  $\Delta r_{\text{np}}$  of  $^{208}\text{Pb}$  was extracted recently from comparison of theory with the measured electric dipole polarizability in  $^{208}\text{Pb}$  [8–11, 113]. However, the focus has mainly been on the linear correlation between the neutron-skin thickness and the slope parameter  $L_0$  of the symmetry energy [76, 98, 99, 114]. The correlation is satisfied to a large degree in the microscopic calculations with mean field models but it is not perfect and a certain model dependence appears in the results [15, 98–101, 105, 114]. In the present thesis work the correlations of  $\Delta r_{\text{np}}$  with various symmetry energy parameters were revisited to look for the plausible causes for the existence of a model dependence in these correlations. This complements the calculations done in Chapter 4, where the correlation between  $\Delta r_{\text{np}}$  of  $^{208}\text{Pb}$  and  $L_0$  was studied within a relativistic mean field model using covariance analysis.

## 5.2 Neutron-skin thickness and symmetry energy parameters in Droplet Model

From a geometrical point of view, the neutron skin thickness in a nucleus may be thought as originated by two different effects. One effect is due to the separation between the mean sharp surfaces of the neutron and proton density distributions. Since this effect corresponds to a different extent of the bulk region of the neutron and proton densities, it is referred as the bulk contribution to the neutron skin thickness. The other effect is due to the different surface widths of the neutron and proton densities, which is called the surface contribution to the neutron skin thickness. To compute the bulk and surface contributions to the neutron skin thickness in a nucleus requires a proper definition of these quantities based on the nuclear densities. In this respect the method described by Hasse and Myers [115] is closely followed.

In order to determine the position of the neutron and proton effective surfaces one can define different radii. In particular, one can define the central radius  $C$  as

$$C = \frac{1}{\rho(0)} \int_0^\infty \rho(r) dr. \quad (5.2)$$

Another option for the mean position of the surface is the equivalent radius  $R$ , which is the radius of a uniform sharp distribution whose density equals the bulk value of the actual density and has the same number of particles:

$$\frac{4}{3}\pi R^3 \rho(\text{bulk}) = 4\pi \int_0^\infty \rho(r) r^2 dr. \quad (5.3)$$

Finally, one can also define the equivalent rms radius  $Q$  that describes a uniform sharp



distribution with the same rms radius as the given density:

$$\frac{3}{5} Q^2 = \langle r^2 \rangle. \quad (5.4)$$

The radii  $C$ ,  $R$ , and  $Q$  are related by the expressions [115]

$$Q = R \left( 1 + \frac{5}{2} \frac{b^2}{R^2} + \dots \right) \quad C = R \left( 1 - \frac{b^2}{R^2} + \dots \right), \quad (5.5)$$

where  $b$  is the surface width of the density profile defined as

$$b^2 = -\frac{1}{\rho(0)} \int_0^\infty (r - C)^2 \frac{d\rho(r)}{dr} dr, \quad (5.6)$$

which provides a measure of the extent of the surface of the nucleus. The neutron skin thickness, which is defined through the rms radii, can be expressed by

$$\Delta r_{np} = \sqrt{\frac{3}{5}} (Q_n - Q_p), \quad (5.7)$$

and using Eq.(5.5) reads:

$$\Delta r_{np} = \sqrt{\frac{3}{5}} \left[ (R_n - R_p) + \frac{5}{2} \left( \frac{b_n^2}{R_n} - \frac{b_p^2}{R_p} \right) \right], \quad (5.8)$$

which clearly separates the bulk and surface contributions as

$$\Delta r_{np}^{\text{bulk}} \equiv \sqrt{\frac{3}{5}} (R_n - R_p), \quad (5.9)$$

and

$$\Delta r_{np}^{\text{surf}} \equiv \sqrt{\frac{3}{5}} \frac{5}{2} \left( \frac{b_n^2}{R_n} - \frac{b_p^2}{R_p} \right). \quad (5.10)$$

In Eqs. (5.8) and (5.10),  $\mathcal{O}[b^4/R^3]$  and higher-order terms are neglected since they represent a small correction [105] to  $\Delta r_{\text{np}}$  – of less or around a 1-2% – that will leave the conclusions unchanged.

The quantal proton and neutron densities obtained within the Skyrme Hartree-Fock or the relativistic mean-field models are described in Chapter 2. In order to extract the bulk and surface contributions to the neutron skin thickness from these distributions of neutrons and protons, the method which was followed closely resembles Refs. [105, 116]. The self-consistent quantal proton and neutron densities were fitted by two-parameter Fermi (2pF) distributions

$$\rho_q(r) = \frac{\rho_{0,q}}{1 + \exp[(r - C_q)/a_q]}, \quad (5.11)$$

where  $q = n, p$ . The parameters  $\rho_{0,q}$ ,  $C_q$  and  $a_q$  are adjusted to reproduce the nucleon numbers as well as the values for the second and fourth moments of the actual density distributions, i.e.,  $\langle r_q^2 \rangle$  and  $\langle r_q^4 \rangle$ . Once this fit is done, one can express Eqs. (5.8)–(5.10) for the neutron skin thickness in terms of the parameters  $C_q$  and  $a_q$  taking into account Eq.(5.5) and the fact that for a 2pF distribution  $b = \pi a/\sqrt{3}$ . Therefore, the bulk and surface contributions to the neutron skin thickness can be written as

$$\Delta r_{\text{np}}^{\text{bulk}} = \sqrt{\frac{3}{5}} \left[ (C_n - C_p) + \frac{\pi^2}{3} \left( \frac{a_n^2}{C_n} - \frac{a_p^2}{C_p} \right) \right], \quad (5.12)$$

$$\Delta r_{\text{np}}^{\text{surf}} = \sqrt{\frac{3}{5}} \frac{5\pi^2}{6} \left( \frac{a_n^2}{C_n} - \frac{a_p^2}{C_p} \right), \quad (5.13)$$

up to terms of order  $\mathcal{O}[a^4/C^3]$ . It should be mentioned that, the  $\Delta r_{\text{np}}$  values calculated from the actual densities obtained self consistently match very well with the ones calculated by summing Eqs. (5.12) and (5.13) after applying our prescription to determine the parameters of the Fermi function.

Some insight about possible correlations between the neutron skin thickness and different observables related to the symmetry energy is provided by the DM [4]. Within this model, which neglects shell correction effects, the neutron skin thickness is expressed by

$$\Delta r_{\text{np}} = \sqrt{\frac{3}{5}} \left[ t - \frac{e^2 Z}{70C_2^0} + \frac{5}{2R} (b_n^2 - b_p^2) \right], \quad (5.14)$$

where  $e^2 Z/70C_2^0$  is a correction due to the Coulomb interaction,  $R = r_0 A^{1/3}$  is the nuclear radius, and  $b_n$  and  $b_p$  are the surface widths of the neutron and proton density profiles. The quantity  $t$  in (5.14) represents the distance between the location of the neutron and proton mean surfaces and therefore is proportional to the bulk contribution to the neutron skin thickness. In the DM its value is given by

$$t = \frac{3}{2} r_0 \frac{C_2^0}{Q_{\text{stiff}}} \frac{I - I_C}{1 + x_A}, \quad (5.15)$$

with

$$I_C = \frac{3e^2}{5r_0} \frac{Z}{12C_2^0} A^{-1/3} \quad \text{and} \quad x_A = \frac{9C_2^0}{4Q_{\text{stiff}}} A^{-1/3}, \quad (5.16)$$

where  $I = (N - Z)/A$ ,  $C_2^0$  is the bulk symmetry energy at saturation, and  $Q_{\text{stiff}}$  is the surface stiffness. For each mean field model, the parameters  $r_0$  and  $C_2^0$  can be obtained from calculations in infinite nuclear matter and  $Q_{\text{stiff}}$  from calculations performed in semi-infinite nuclear matter [100, 117, 118].

Within the DM, the symmetry energy coefficient of a finite nucleus of mass number  $A$  is given by

$$a_{\text{sym}}(A) = \frac{C_2^0}{1 + x_A}. \quad (5.17)$$

Replacing  $a_{\text{sym}}(A)$  in Eq. (5.15), the separation distance between the mean surfaces of

neutrons and protons can be recast as

$$t = \frac{2r_0}{3C_2^0} [C_2^0 - a_{sym}(A)] A^{1/3} (I - I_C). \quad (5.18)$$

The link between a property in finite nuclei such as  $a_{sym}(A)$  and some symmetry energy parameters in infinite nuclear matter may be obtained from the observation [15] that for a heavy nucleus there is a subsaturation density, which for  $^{208}\text{Pb}$  is around  $0.1 \text{ fm}^{-3}$ , such that the symmetry energy coefficient in the finite nucleus  $a_{sym}(A)$  equals the symmetry energy in nuclear matter  $C_2(\rho)$  computed at that density. This relation is roughly independent of the mean field model used to compute it. Around the saturation density  $\rho_0$  the symmetry energy can be expanded as

$$C_2(\rho) \simeq C_2^0 - L_0 \left( \frac{\rho_0 - \rho}{3\rho_0} \right) + \frac{1}{2} K_{sym} \left( \frac{\rho_0 - \rho}{3\rho_0} \right)^2. \quad (5.19)$$

Consequently, the distance  $t$  can be finally expressed approximately as [15]

$$t = \frac{2r_0}{3C_2^0} L_0 \left( \frac{\rho - \rho_0}{3\rho_0} \right) \left[ 1 - \frac{K_{sym}}{2L_0} \left( \frac{\rho - \rho_0}{3\rho_0} \right) \right] A^{1/3} (I - I_C). \quad (5.20)$$

Equations (5.18) and (5.20) suggest correlations between the bulk neutron skin thickness in finite nuclei and some isovector indicators such as  $C_2^0 - a_{sym}(A)$ ,  $a_{sym}(A)/C_2^0$  and  $L_0$ . To compute the average symmetry energy of a finite nucleus with the DM (Eq. (5.17)) requires the knowledge of the surface stiffness  $Q_{\text{stiff}}$ , which in turn requires semi-infinite nuclear matter calculations [100]. An efficient procedure to circumvent this, is to evaluate  $a_{sym}(A)$  within a local density approximation as [74]

$$a_{sym}(A) = \frac{4\pi}{AI^2} \int [r^2 \rho(r) I^2(r)] C_2(\rho(r)) dr, \quad (5.21)$$

where  $I(r) = \frac{\rho_n(r) - \rho_p(r)}{\rho(r)}$  is the local isospin asymmetry and  $\rho(r)$  is the sum of the neutron and proton densities. This approximation works very well for medium heavy  $^{132}\text{Sn}$  or heavy  $^{208}\text{Pb}$  nuclei [119].

### 5.3 Results and discussions

The neutron-skin thickness and several symmetry energy parameters are calculated using five different families of systematically varied models, namely, the SAMi-J [10, 37], DDME [81], FSV, TSV and KDE0-J models. The energy density functional associated with DDME, FSV, and TSV corresponds to an effective Lagrangian density typical of the relativistic mean-field models, whereas SAMi-J and KDE0-J are based on the standard form of the Skyrme force (see Chapter 2).

The different families of systematically varied parameter sets were obtained so that they explore different values of the symmetry energy parameters around an optimal value, while reasonably keeping the quality of the best fit. The values of the neutron-skin thickness in a heavy nucleus like  $^{208}\text{Pb}$  vary over a wide range within the families due to the variations of the symmetry energy parameters. The parameter sets for the FSV, TSV and KDE0-J families were obtained in the present thesis work. The effective Lagrangian density employed for the FSV family is similar to that for the FSU model [50]. In addition to the coupling of  $\rho$  meson to the nucleons as conventionally employed, the presence of a cross-coupling between the  $\omega$  and  $\rho$  mesons in the FSU model enables one to vary the symmetry energy, and accordingly the symmetry energy slope parameter  $L_0$ , over a wide range without significantly affecting the quality of the fit to the bulk properties of the finite nuclei. The TSV family is obtained using the effective Lagrangian density as introduced in Ref. [53] in which the  $\rho$ -meson and its coupling to the  $\sigma$ -meson govern the isovector

part of the interactions between the nucleons. The  $\omega - \rho$  cross coupling in the FSV family and the  $\sigma - \rho$  cross coupling in the TSV family produce different behaviors in the density dependence of the symmetry energy, because the source term for the  $\omega$ -field is governed by the baryon density and that for the  $\sigma$ -field is governed by the scalar density. The experimental data employed to determine the TSV and FSV families are the total binding energies for the  $^{16}\text{O}$ ,  $^{40,48}\text{Ca}$ ,  $^{68}\text{Ni}$ ,  $^{90}\text{Zr}$ ,  $^{100,132}\text{Sn}$ ,  $^{208}\text{Pb}$  nuclei, and the root mean square charge radii for the  $^{16}\text{O}$ ,  $^{40,48}\text{Ca}$ ,  $^{90}\text{Zr}$ ,  $^{208}\text{Pb}$  nuclei. The energy density functional for the KDE0-J family calculated within the Skyrme ansatz is taken from the KDE0 force of Ref. [120]. The model parameters are constrained to yield the nuclear matter incompressibility coefficient in the range of 225–250 MeV. The calculated values of the total binding energy and the charge radius for the  $^{208}\text{Pb}$  nucleus obtained for all the models considered deviate from the experimental data only within 0.25% and 0.8%, respectively.

### 5.3.1 Correlation plots associated with isovector indicators

The DM provides a useful guideline to suggest the kind of correlations that one can expect between the neutron skin thickness and the symmetry energy parameters. As shown in Ref. [105], these correlations are mainly due to the bulk term of Eq.(5.14) rather than to the surface contribution to  $\Delta r_{\text{np}}$ . In the bulk part of  $\Delta r_{\text{np}}$ , the quantity  $(C_2^0 - a_{\text{sym}}(A)) / C_2^0$  determines the ratio of the surface symmetry to volume symmetry energies, see Eq.(5.18); the close relation of different isovector observables in finite nuclei with the ratio of the surface and volume symmetry energies has been observed in several studies [30, 104]. The values of  $r_0$  for the various models considered in the present thesis work display only a small variation indicating that the total neutron-skin thickness  $\Delta r_{\text{np}}$  of a given heavy nucleus may

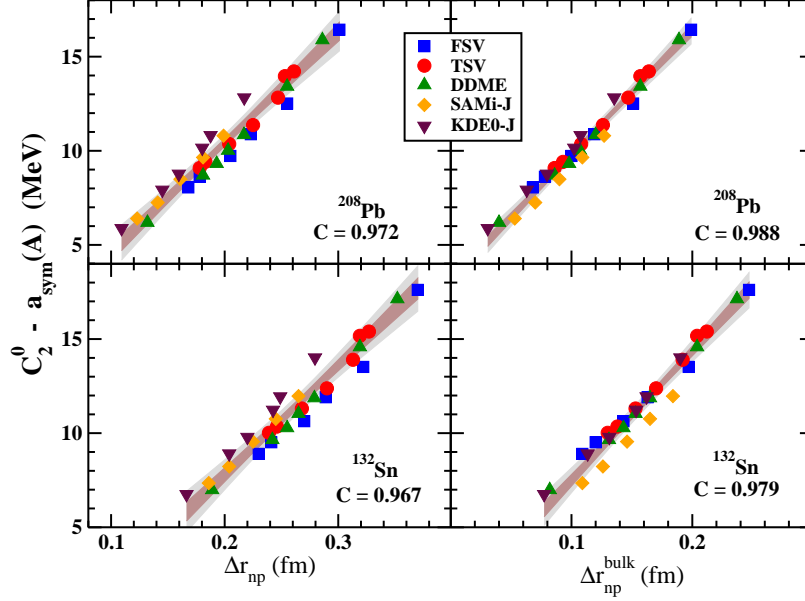


Figure 5.1: Plots for the difference between the symmetry energy coefficient for infinite nuclear matter  $C_2^0$  and that for finite nuclei  $a_{\text{sym}}(A)$  as a function of the neutron-skin thickness (left panels) and of the bulk part of the neutron-skin thickness (right panels). The results are obtained using five different families of mean-field models, namely, FSV (blue squares), TSV (red circles), DDME (green triangles), SAMi-J (orange diamonds) and KDE0-J (maroon inverted triangles). The correlation coefficients are:  $C(C_2^0 - a_{\text{sym}}(A), \Delta r_{\text{np}}) = 0.972$  ( $0.967$ ) and  $C(C_2^0 - a_{\text{sym}}(A), \Delta r_{\text{np}}^{\text{bulk}}) = 0.988$  ( $0.979$ ) for  $^{208}\text{Pb}$  ( $^{132}\text{Sn}$ ) nuclei. The inner (outer) colored regions depict the loci of the 95% confidence (prediction) bands of the regression [121].

be correlated to the ratio  $(C_2^0 - a_{\text{sym}}(A)) / C_2^0$ , or also to the difference  $(C_2^0 - a_{\text{sym}}(A))$  provided the value of  $C_2^0$  does not show a large variation as compared to  $(C_2^0 - a_{\text{sym}}(A))$ .

In Fig. 5.1, the values of  $C_2^0 - a_{\text{sym}}(A)$  are plotted as a function of  $\Delta r_{\text{np}}$  in the left panel, and as a function of the bulk part of the neutron-skin thickness  $\Delta r_{\text{np}}^{\text{bulk}}$  in the right panel, for  $^{208}\text{Pb}$  and  $^{132}\text{Sn}$  nuclei. The results are reported for the five different families of systematically varied models, namely, FSV, TSV, SAMi-J, DDME and KDE0-J as indicated in the figure. Fairly evident linear correlations are observed between  $C_2^0 - a_{\text{sym}}(A)$  and both  $\Delta r_{\text{np}}$  and  $\Delta r_{\text{np}}^{\text{bulk}}$ . More quantitatively, the Pearson's correlation coefficients  $C(X, Y)$  [65] are calculated, their values are  $C(C_2^0 - a_{\text{sym}}(A), \Delta r_{\text{np}}) = 0.972$  ( $0.967$ ) and

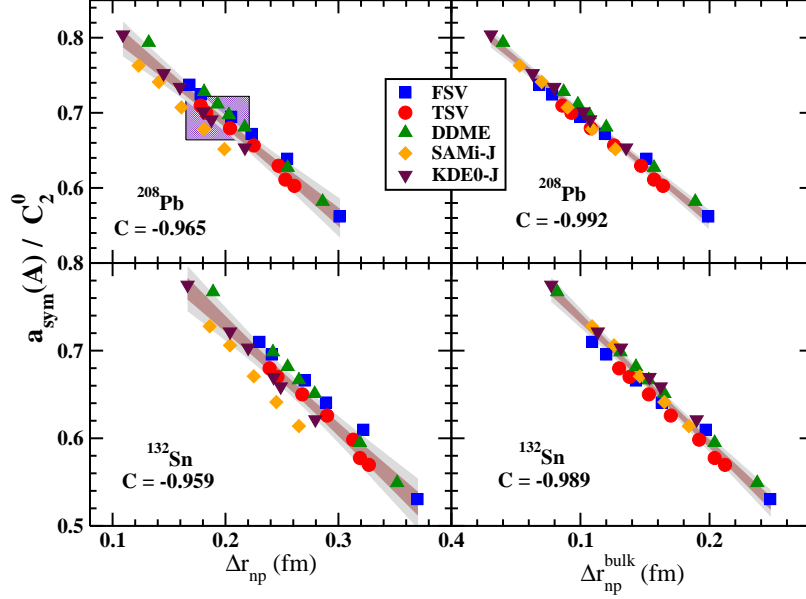


Figure 5.2: Plots for the ratio of the nuclear symmetry energy coefficient for finite nuclei  $a_{\text{sym}}(A)$  to that for infinite nuclear matter  $C_2^0$ , as a function of the neutron-skin thickness (left panels) and of the bulk part of the neutron-skin thickness (right panels). The square shaded region in the upper-left panel corresponds to  $a_{\text{sym}}(A) = 22.4 \pm 0.3$  [122] MeV and  $C_2^0 = 32.3 \pm 1.3$  MeV [31]. The correlation coefficients are  $|C(a_{\text{sym}}(A)/C_2^0, \Delta r_{\text{np}})| = 0.965$  (0.959) and  $|C(a_{\text{sym}}(A)/C_2^0, \Delta r_{\text{np}}^{\text{bulk}})| = 0.992$  (0.989) for  $^{208}\text{Pb}$  ( $^{132}\text{Sn}$ ) nuclei. The inner (outer) colored regions depict the loci of the 95% confidence (prediction) bands of the regression [121].

$C(C_2^0 - a_{\text{sym}}(A), \Delta r_{\text{np}}^{\text{bulk}}) = 0.988$  (0.979) for the  $^{208}\text{Pb}$  ( $^{132}\text{Sn}$ ) nuclei, respectively. Thus, the correlation of  $C_2^0 - a_{\text{sym}}(A)$  with  $\Delta r_{\text{np}}^{\text{bulk}}$  is a little higher than with  $\Delta r_{\text{np}}$  for both  $^{208}\text{Pb}$  and  $^{132}\text{Sn}$  nuclei.

Following Eq. (5.18) one can directly correlate  $(C_2^0 - a_{\text{sym}}(A))/C_2^0$  (or equivalently  $a_{\text{sym}}(A)/C_2^0$ ) with  $\Delta r_{\text{np}}$  of a heavy nucleus. In Fig. 5.2 the ratio  $a_{\text{sym}}(A)/C_2^0$  as a function of  $\Delta r_{\text{np}}$  and of  $\Delta r_{\text{np}}^{\text{bulk}}$  are displayed for the  $^{208}\text{Pb}$  and  $^{132}\text{Sn}$  nuclei. The correlations of  $a_{\text{sym}}(A)/C_2^0$  with  $\Delta r_{\text{np}}$  are relatively weaker in comparison to those with  $\Delta r_{\text{np}}^{\text{bulk}}$ . In the case of  $a_{\text{sym}}(A)/C_2^0$  and  $\Delta r_{\text{np}}$  the correlation coefficient is  $|C(a_{\text{sym}}(A)/C_2^0, \Delta r_{\text{np}})| = 0.965$  (0.959) for  $^{208}\text{Pb}$  ( $^{132}\text{Sn}$ ), whereas in the case of  $a_{\text{sym}}(A)/C_2^0$  and  $\Delta r_{\text{np}}^{\text{bulk}}$  the correla-



tion coefficient increases up to high values  $|C(a_{\text{sym}}(A)/C_2^0, \Delta r_{\text{np}}^{\text{bulk}})| = 0.992$  (0.989) for  $^{208}\text{Pb}$  ( $^{132}\text{Sn}$ ).

It is interesting to address the constraints on the neutron-skin thickness that may be deduced from the present study. The rectangular shaded region in the upper-left panel of Fig. 5.2 corresponds to  $a_{\text{sym}}(A) = 22.4 \pm 0.3$  MeV for  $^{208}\text{Pb}$  [122] and  $C_2^0 = 32.3 \pm 1.3$  MeV [31], which yields  $\Delta r_{\text{np}} = 0.193 \pm 0.028$  fm in the  $^{208}\text{Pb}$  nucleus. This value is compatible with the recent constraints on the the neutron skin thickness of  $^{208}\text{Pb}$  derived from the measured electric dipole polarizability in  $^{68}\text{Ni}$ ,  $^{120}\text{Sn}$  and  $^{208}\text{Pb}$  [11]. The constraint  $a_{\text{sym}}(A) = 22.4 \pm 0.3$  MeV was evaluated in Ref. [122] using the experimental binding energy differences. Furthermore, the effect of the Coulomb interaction on the surface asymmetry and the effect of the surface diffuseness on the Coulomb energy were taken into account. The value of  $C_2^0 = 32.3 \pm 1.3$  MeV [31], as obtained by analyzing the experimental data on the pygmy dipole resonance combined with the correlation between  $L_0$  and  $C_2^0$ , has a quite reasonable overlap with the values of  $C_2^0$  that have been extracted either from a version of the finite-range droplet model (FRDM) that performs very well in reproducing the experimental mass systematics [1], or from specific manipulation of the semi-empirical mass formula [2], or through analysis of the properties of semi-infinite nuclear matter [123]. This value of  $C_2^0$  also overlaps with the conclusions provided in recent papers [11, 33, 124].

It is desirable to check the degree of consistency between the results for different heavy nuclei, in particular between  $^{208}\text{Pb}$  and  $^{132}\text{Sn}$  which would allow to predict the neutron skin thickness of the nucleus  $^{132}\text{Sn}$  assumed that the one of  $^{208}\text{Pb}$  is known. In the left panel of Fig. 5.3, we plot  $\Delta r_{\text{np}}$  for the  $^{132}\text{Sn}$  nucleus against that for the  $^{208}\text{Pb}$  nucleus. Similarly, the results for  $\Delta r_{\text{np}}^{\text{bulk}}$  and  $\Delta r_{\text{np}}^{\text{surf}}$  are plotted in the middle and right panels of Fig. 5.3, respectively. It is observed that the values of  $\Delta r_{\text{np}}$ ,  $\Delta r_{\text{np}}^{\text{bulk}}$  and  $\Delta r_{\text{np}}^{\text{surf}}$  for the  $^{132}\text{Sn}$  nucleus

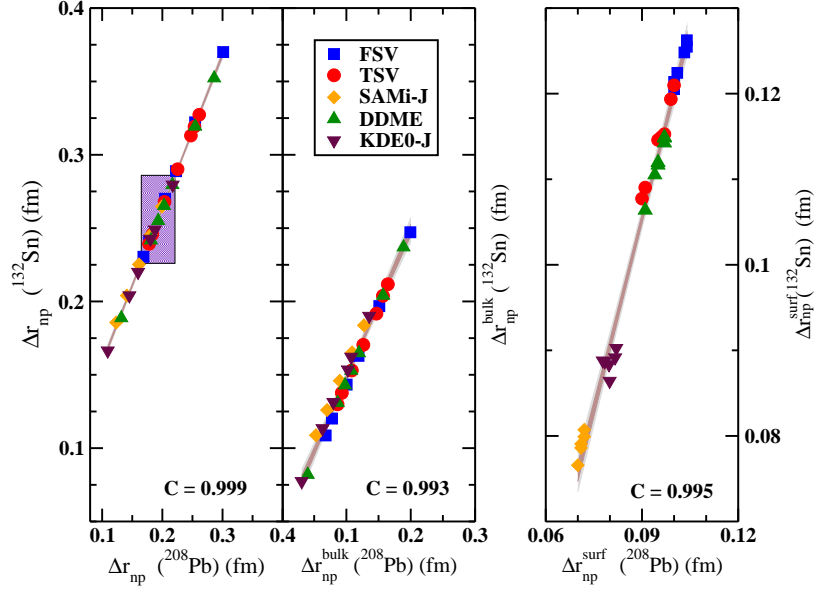


Figure 5.3: Neutron-skin thickness (left) and its bulk (middle) and surface (right) contributions for the  $^{132}\text{Sn}$  nucleus plotted against the same quantities for the  $^{208}\text{Pb}$  nucleus. The shaded region corresponds to the values of the neutron-skin thickness in  $^{132}\text{Sn}$  determined from the ones estimated for the  $^{208}\text{Pb}$  nucleus (see also Fig. 5.2). The correlation coefficients obtained for the results presented in the left, middle and right panels are 0.999, 0.993 and 0.995, respectively. The inner (outer) colored regions depict the loci of the 95% confidence (prediction) bands of the regression [121].

are very well correlated with the corresponding values in the  $^{208}\text{Pb}$  nucleus. This is in harmony with earlier work [125]. Hence, the information provided by the neutron skin of two heavy nuclei on the isovector channel of the nuclear effective interaction is mutually inclusive. Such an observation allows one to predict  $\Delta r_{\text{np}} = 0.256 \pm 0.030$  fm for  $^{132}\text{Sn}$  nucleus by using the above estimated value for  $^{208}\text{Pb}$  of  $\Delta r_{\text{np}} = 0.193 \pm 0.028$  fm.

As discussed in the literature [105], the correlation between the neutron-skin thickness and  $(C_2^0 - a_{\text{sym}}(A))/C_2^0$  leads to a correlation between the neutron-skin thickness and the symmetry energy slope parameter  $L_0$ . In Fig. 5.4, the variation of  $L_0$  as a function of  $\Delta r_{\text{np}}$  (left),  $\Delta r_{\text{np}}^{\text{bulk}}$  (middle) and  $\Delta r_{\text{np}}^{\text{surf}}$  (right panel) are depicted for the  $^{208}\text{Pb}$  nucleus for the four families of models obtained in this present thesis work. Using the constraint on  $\Delta r_{\text{np}}$

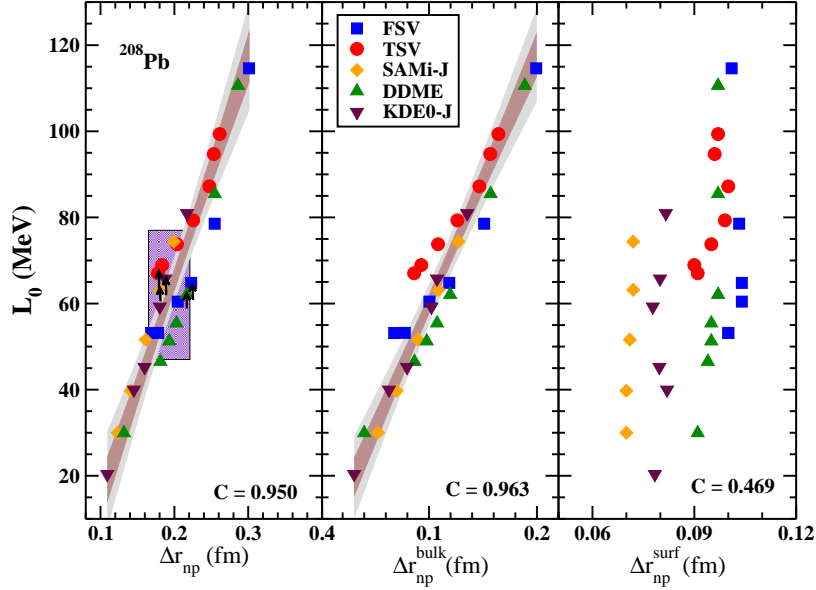


Figure 5.4: Plots for the symmetry energy slope parameter  $L_0$  as a function of the neutron-skin thickness (left), its bulk part (middle) and its surface part (right) for the  $^{208}\text{Pb}$  nucleus. The shaded region in the left panel projects out the values of  $L_0 = 62 \pm 15$  MeV obtained from  $\Delta r_{\text{np}} = 0.193 \pm 0.028$  fm which, in turn, is obtained by using the empirical values of  $C_2^0$  and  $a_{\text{sym}}(A)$  (see also Fig. 5.2). The arrow marks in the left panel indicate the points with the slope parameter  $L_0 \sim 65$  MeV. The values of the correlation coefficients are  $C(L_0, \Delta r_{\text{np}}) = 0.950$ ,  $C(L_0, \Delta r_{\text{np}}^{\text{bulk}}) = 0.963$  and  $C(L_0, \Delta r_{\text{np}}^{\text{surf}}) = 0.469$ . The inner (outer) colored regions depict the loci of the 95% confidence (prediction) bands of the regression [121].

( $^{208}\text{Pb}$ ) obtained in Fig. 5.2, the bound on the value of  $L_0$  comes out to be  $L_0 = 62 \pm 15$  MeV; displayed as the shaded region of left panel in Fig. 5.4. The correlation coefficients of  $L_0$  with  $\Delta r_{\text{np}}$  and with  $\Delta r_{\text{np}}^{\text{bulk}}$  are lower than in the case of the correlations displayed in Figs. 5.1 and 5.2, suggesting that the neutron-skin thickness is slightly better correlated with  $C_2^0 - a_{\text{sym}}(A)$  or the ratio  $a_{\text{sym}}(A)/C_2^0$  than with the slope parameter  $L_0$ . This might be a feature of the families chosen in the present thesis and does not necessarily apply to the situation in which one employs a large set of unbiasedly selected models [105].

The “arrow” marks in Fig. 5.4 indicate the five models, each from a different family, with  $L_0$  varying in a narrow range of 62.1 MeV to 67.0 MeV. For these five models, there

happens to be a spread in  $\Delta r_{\text{np}}$  of almost 0.05 fm which is larger than expected. In comparison, the equation of the linear fit of the results of all models in the left panel of Fig. 5.4 gives a variation in the value of  $\Delta r_{\text{np}}(^{208}\text{Pb})$  with the change of  $L_0$  as,  $\delta(\Delta r_{\text{np}}) \simeq 0.002 \delta L_0$ , so that a change in  $L_0$  of 5 MeV implies an average change in  $\Delta r_{\text{np}}$  of about 0.01 fm only, which is smaller than the observed spread of 0.05 fm in the five models mentioned above. The DM supports a similar conclusion, as it can be seen from Eq. (5.20) that the DM predicts an average variation of  $\Delta r_{\text{np}}(^{208}\text{Pb})$  with  $L_0$  approximately as,  $\delta(\Delta r_{\text{np}}) \simeq 0.003 \delta L_0$ . The two mentioned models from the TSV and SAMi-J families have  $L_0 = 67$  MeV and  $L_0 = 63.2$  MeV, respectively, and yield in  $^{208}\text{Pb}$  smaller values of  $\Delta r_{\text{np}} \simeq 0.18$  fm, whereas the two models from the FSV and DDME families have  $L_0 = 64.8$  MeV and  $L_0 = 62.1$  MeV, respectively, and give rise to larger values of  $\Delta r_{\text{np}} \simeq 0.22$  fm. The model from KDE0-J family with  $L_0 = 65.7$  MeV yields an intermediate value of  $\Delta r_{\text{np}}(^{208}\text{Pb}) \simeq 0.19$  fm. Actually, it comes as an intriguing fact that the extracted values of  $\Delta r_{\text{np}}$  differ by  $\sim 0.05$  fm for the two models of the FSV and TSV families with similar  $L_0$ , although the parameters for these two families are obtained by using exactly the same kind of fitting protocol. In the next subsection, the plausible interpretations for such differences in the neutron skin thickness corresponding to models with similar  $L_0$  values are investigated.

### 5.3.2 Systematic differences between the families of functionals

In an attempt to understand the issues raised at the end of the previous subsection, a detailed comparison is made between the results for the five models belonging to different families but yielding almost the same values for  $L_0$ . First a closer look is given in Fig. 5.5 into the values of the symmetry energy  $C_2(\rho)$  (lower panel) and its density derivative  $3\rho_0 C_2'(\rho)$

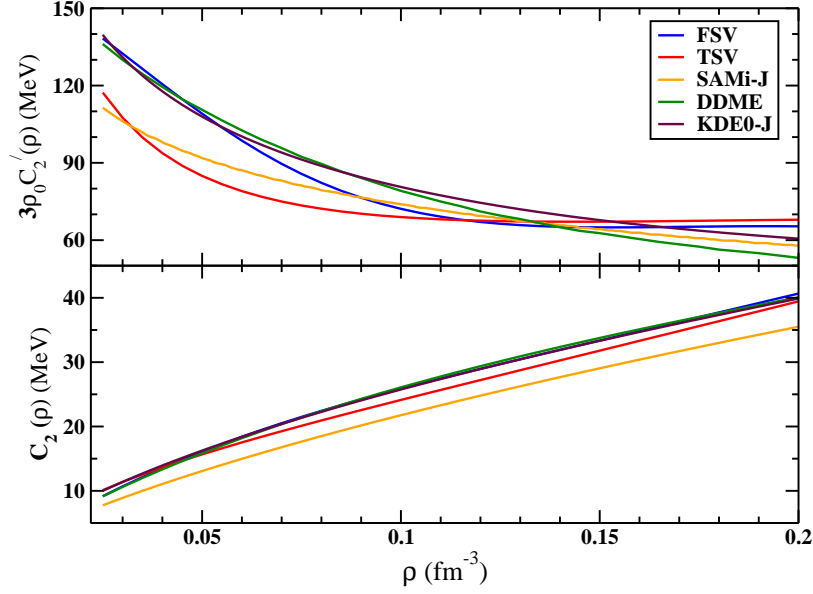


Figure 5.5: The nuclear symmetry energy  $C_2$  (lower panel) and its density derivative  $C_2'$  multiplied by  $3\rho_0$  (upper panel) as a function of density for the five different models associated with the slope parameter for nuclear matter  $L_0 \sim 65$  MeV. Each of these models belongs to a different family (see also Table 5.1).

(upper panel) as a function of density for these models. The behavior of  $C_2(\rho)$  as a function of density seemingly appears to be similar for the five models. But the values of  $3\rho_0 C_2'(\rho)$  show significant differences in the low density region ( $\rho < 0.10 \text{ fm}^{-3}$ ). Furthermore, one may note that the TSV and SAMi-J models corresponding to  $\Delta r_{\text{np}}(^{208}\text{Pb}) \sim 0.18$  fm and the KDE0-J model with  $\Delta r_{\text{np}}(^{208}\text{Pb}) \sim 0.19$  fm display a relatively similar behavior in the density dependence of  $C_2'(\rho)$ . The same is true for the FSV and DDME models corresponding to  $\Delta r_{\text{np}}(^{208}\text{Pb}) \sim 0.22$  fm.

To investigate whether such differences in the values of the density derivative of the symmetry energy at lower densities have an influence in the finite nuclei calculations, and motivated by Eq. (5.21), an effective value of the slope parameter  $L_{\text{eff}}$  is defined, which might be more sensitive to the relative distributions of neutrons with respect to protons in

finite nuclei, as follows:

$$L_{\text{eff}} = \frac{3\rho_0 \int [r^2 \rho(r) I^2(r)] C_2'(\rho(r)) dr}{\int [r^2 \rho(r) I^2(r)] dr}. \quad (5.22)$$

Here,  $I(r)$  is the local asymmetry parameter defined as,  $I(r) \equiv (\rho_n(r) - \rho_p(r))/\rho(r)$ . If one assumes  $C_2(\rho)$  to be linear in density, the  $L_{\text{eff}}$  parameter coincides with  $L_0$  (see Eq. (5.19)). However, one can see in Fig. 5.5 that  $C_2(\rho)$  can depart significantly from linearity at low densities. Therefore, the  $L_{\text{eff}}$  parameter as defined in Eq. (5.22) tries to take into account this effect. At very low densities ( $\rho < 0.01 \text{ fm}^{-3}$ )  $C_2(\rho)$  deviates largely from linearity. The integrals in the numerator and denominator of Eq. (5.22) are thus evaluated by integrating from the center of the nucleus, where the density  $\rho(r)$  is of the order of  $\rho_0$ , up to the point where the density of the nucleus falls to  $0.01 \text{ fm}^{-3}$ , which corresponds to a radial coordinate  $r$  of about 9 fm. It is worthwhile to mention that here the goal was to study the effect of  $C_2'(\rho)$  but not the quantity  $L(\rho)$  ( $\equiv 3\rho C_2'(\rho)$ ) on the  $\Delta r_{\text{np}}$  of a heavy nucleus. That is why  $\rho_0$  was kept outside the integral of the numerator in Eq. (5.22). The values of  $L_{\text{eff}}$  along with various other properties evaluated for the five models corresponding to  $L_0 \sim 65 \text{ MeV}$  are compared in Table 5.1.

It can be easily observed in Table 5.1 that though the values of  $L_0$  for these models vary only by  $\sim 5 \text{ MeV}$ , the values of  $\Delta r_{\text{np}}$  of heavy nuclei calculated from the same models can differ by  $\sim 0.05 \text{ fm}$ , which is larger than the average spread of the correlation between  $\Delta r_{\text{np}}$  and  $L_0$ . Interestingly, when one looks at the extracted  $L_{\text{eff}}$  parameter, the models from SAMi-J and TSV families those predict  $\Delta r_{\text{np}}(^{208}\text{Pb}) \sim 0.18 \text{ fm}$  give similar  $L_{\text{eff}} \sim 82 \text{ MeV}$ , and the models from FSV and DDME families those predict  $\Delta r_{\text{np}}(^{208}\text{Pb}) \sim 0.22 \text{ fm}$  give similar  $L_{\text{eff}} \sim 96 \text{ MeV}$ . The model from the KDE0-J family with  $\Delta r_{\text{np}}(^{208}\text{Pb}) \sim 0.19 \text{ fm}$  predicts  $L_{\text{eff}} \sim 91 \text{ MeV}$ . That is, the models with larger  $L_{\text{eff}}$  give larger  $\Delta r_{\text{np}}$  and vice

Table 5.1: Comparison of the properties of infinite nuclear matter (NM) and of the  $^{208}\text{Pb}$  and  $^{132}\text{Sn}$  nuclei for the five different models that yield a value of  $L_0$  around 65 MeV.

		SAMi-J	TSV	FSV	DDME	KDE0-J
NM	$\rho_0(\text{fm}^{-3})$	0.157	0.147	0.149	0.152	0.162
	$L_0(\text{MeV})$	63.2	67.0	64.8	62.1	65.7
	$C_2^0(\text{MeV})$	30.00	31.29	33.16	34.00	35.00
$^{208}\text{Pb}$	$a_{\text{sym}}(A)(\text{MeV})$	20.35	22.20	22.28	23.15	24.18
	$\Delta r_{\text{np}}(\text{fm})$	0.181	0.178	0.223	0.217	0.188
	$\Delta r_{\text{np}}^{\text{bulk}}(\text{fm})$	0.109	0.086	0.119	0.120	0.108
	$L_{\text{eff}}(\text{MeV})$	81.2	82.7	95.7	96.5	90.8
$^{132}\text{Sn}$	$a_{\text{sym}}(A)(\text{MeV})$	19.24	21.27	21.25	22.13	23.06
	$\Delta r_{\text{np}}(\text{fm})$	0.245	0.239	0.289	0.279	0.249
	$\Delta r_{\text{np}}^{\text{bulk}}(\text{fm})$	0.165	0.130	0.163	0.165	0.163
	$L_{\text{eff}}(\text{MeV})$	84.3	85.7	101.2	98.0	97.8

versa. In fact, further inspection of Fig. 5.4 reveals that two members of the FSV and DDME families with  $\Delta r_{\text{np}}(^{208}\text{Pb}) \sim 0.18$  fm, same as the SAMi-J and TSV models in Table 5.1, predict departing  $L_0$  values ( $L_0 = 53.2$  MeV in the FSV model and  $L_0 = 46.5$  MeV in the DDME model). It turns out that these FSV and DDME models also explore similar values of  $L_{\text{eff}}$  (83.9 MeV in FSV and 86.6 MeV in DDME) as done by the models from the SAMi-J and TSV families displayed in Table 5.1 with  $\Delta r_{\text{np}} \sim 0.18$  fm. In principle, one can also define  $L_{\text{eff}}$  without the  $I^2(r)$  terms in Eq. (5.22). That is why, the calculations of  $L_{\text{eff}}$  were repeated by taking  $I^2(r)$  to be unity in Eq. (5.22) and similar trends were found as explained above. In Table 5.1, concerning the properties of uniform matter, it is also noticeable that the models do not display the same value of the saturation density. For the non-relativistic functionals belonging to the SAMi-J and KDE0-J family this value is about 5–10% larger than the values explored by the relativistic functionals. This fact has some impact on the extracted values of  $L_{\text{eff}}$  for these models (see Eq. (5.22)).

To have a better insight into the source of the differences between the values of  $L_{\text{eff}}$  for the models with similar values of  $L_0$  at  $\rho_0$ , in Fig. 5.6 the total density distribution

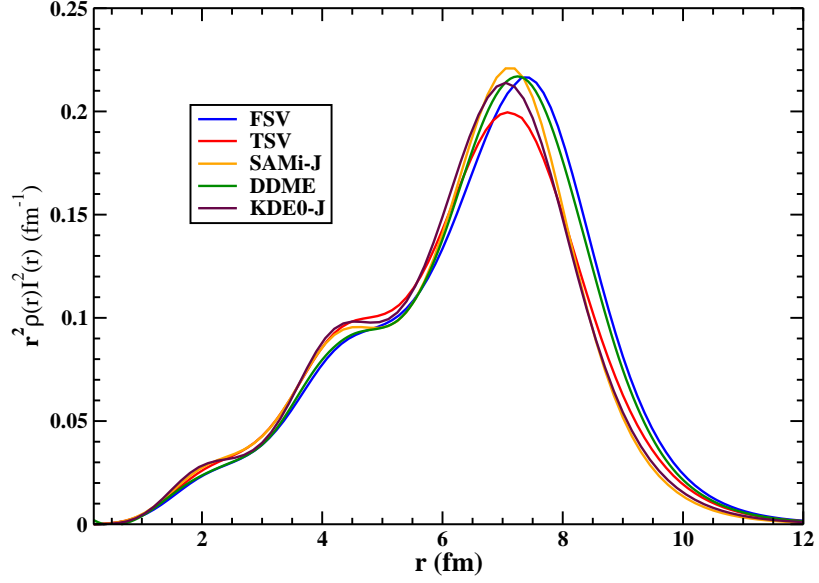


Figure 5.6: The variation of  $r^2\rho(r)I^2(r)$  as a function of the radial coordinate  $r$  in  $^{208}\text{Pb}$  for the five models that yield a symmetry energy slope parameter  $L_0 \sim 65$  MeV.

$\rho(r)$  of  $^{208}\text{Pb}$  multiplied by  $r^2I^2(r)$  is plotted for the models with  $L_0 \sim 65$  MeV. The values of  $r^2\rho(r)I^2(r)$  for all the different cases are close to each other up to  $r \sim 6$  fm, in this region  $\rho(r) \geq 0.1 \text{ fm}^{-3}$ . With further increase in  $r$ , the differences in the values of  $r^2\rho(r)I^2(r)$  gradually become noticeable. One can argue that different behaviors in the surface region may be responsible for different values of  $L_{\text{eff}}$  and consequently lead to different values of  $\Delta r_{\text{np}}$  in heavy nuclei like  $^{208}\text{Pb}$  or  $^{132}\text{Sn}$ . The question still remains whether  $L_{\text{eff}}$  is more sensitive to the density dependence of  $C'_2(\rho)$  (upper panel of Fig. 5.5) or to the density distributions of nucleons inside the nucleus (Fig. 5.6). To unmask this, the values of  $L_{\text{eff}}$  were calculated using  $C'_2(\rho)$  of a given model, but with the density distributions of nucleons from the five models that have  $L_0 \sim 65$  MeV. This calculation was repeated for the different choices of  $C'_2(\rho)$  of these five models. The values of  $L_{\text{eff}}$  so obtained did not show the trend as observed in Table 5.1, where  $C'_2(\rho)$  and the density distributions of nucleons used correspond to the same model consistently. Thus, the values



of  $L_{\text{eff}}$  are sensitive to both the density dependence of the symmetry energy and the density distributions of nucleons inside the nucleus. It should be pointed out that the differences in the values of  $L_{\text{eff}}$  for the models with similar  $L_0$  parameter are mainly due to the differences in the low density behavior of  $C_2'(\rho)$  and the distributions of nucleons in the surface region of the nucleus.

## 5.4 Summary

To summarize, the correlations of the neutron-skin thickness in finite nuclei with various symmetry energy parameters pertaining to infinite nuclear matter were revisited. Particular attention is paid to the model dependence in such correlations that can play a role in understanding the density dependence of the nuclear symmetry energy. The finite nuclei analyzed are  $^{208}\text{Pb}$  and  $^{132}\text{Sn}$ . The symmetry energy parameters considered are  $C_2^0 - a_{\text{sym}}(A)$ ,  $a_{\text{sym}}(A)/C_2^0$  and  $L_0$ , where  $C_2^0$  and  $L_0$  are the symmetry energy and the symmetry energy slope associated with infinite nuclear matter at the saturation density, and  $a_{\text{sym}}(A)$  corresponds to the symmetry energy parameter in finite nuclei. Five different families of systematically varied mean-field models corresponding to different energy density functionals are employed to calculate the relevant quantities for the finite nuclei and those for the infinite nuclear matter.

In general, the correlations of the neutron-skin thickness with the different symmetry energy parameters are strong within the individual families of the models. Once the results for all the different families are combined, the correlation coefficients become smaller, indicating a model dependence. The correlations of the symmetry energy parameters with the bulk part  $\Delta r_{\text{np}}^{\text{bulk}}$  of the neutron-skin thickness are less model dependent than with the total neutron-skin thickness  $\Delta r_{\text{np}}$ . Exceptionally, the bulk part of the neutron-skin

thickness is found to be correlated with  $C_2^0 - a_{\text{sym}}(A)$  and  $a_{\text{sym}}(A)/C_2^0$  in an almost model independent manner.

To understand better the model dependence in the various correlations considered, the results are compared for the models belonging to different families, but yielding similar values of  $L_0$ . An effective value of the symmetry energy slope parameter  $L_{\text{eff}}$  was determined using the density distributions of nucleons and the density derivative of the symmetry energy for these models. It is found that the values of  $\Delta r_{\text{np}}$ , which differ for the models with the same  $L_0 \sim 65$  MeV, are in harmony with the values of  $L_{\text{eff}}$ . Differences in the values of  $L_{\text{eff}}$  are caused by differences in the density distributions of nucleons in the surface region and the derivative of the symmetry energy at subsaturation densities.

# INTERDEPENDENCE AMONG THE SYMMETRY ENERGY PARAMETERS

---

## 6.1 Introduction

The symmetry energy coefficient  $C_2(\rho)$  is now known in tighter bounds at the saturation density  $\rho_0$  [1, 2] of symmetric nuclear matter (SNM). From analysis of the giant dipole resonance (GDR) of  $^{208}\text{Pb}$  nucleus, a well-constrained estimate of  $C_2(\rho)$  at a somewhat lesser density ( $\rho = 0.1 \text{ fm}^{-3}$ ) [29] is also known. The value of the density slope of the symmetry energy  $L_0$  is less certain [15, 74, 126]. Tremendous amount of efforts are being made over last decade or so to constrain the value of  $L_0$ . In chapter (4) a stringent constraint on the value of  $L_0$  is obtained in a relativistic mean-field (RMF) framework by incorporating binding energies of highly asymmetric nuclei (number of neutrons is twice to that of protons i.e.  $N \approx 2Z$ ) in the fitting protocol to obtain the parameters of the model. The currently accepted value of  $L_0$  is lying between 50 and 60 MeV. However, this is not the case for even higher order derivatives of the symmetry energy [e.g.  $K_{sym}^0$

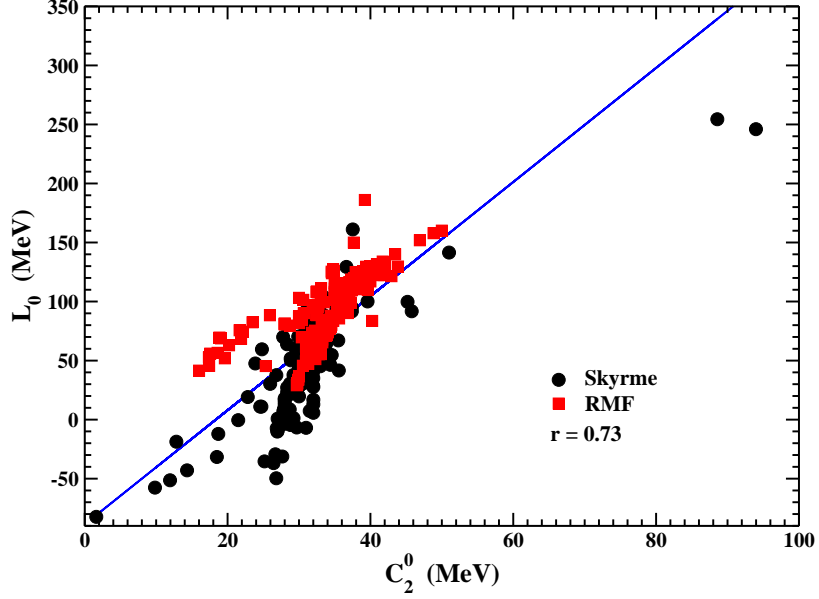


Figure 6.1: Values of  $L_0$  plotted against  $C_2^0$  as obtained from 500 EDFs based on both relativistic and non-relativistic mean-field [13, 14]. The black circles correspond to the non-relativistic Skyrme-inspired EDFs and the red squares refer to those obtained from relativistic mean field (RMF) models.

( $= K_{sym}(\rho_0) = 9\rho_0^2 \left( \frac{\partial^2 C_2}{\partial \rho^2} \right)_{\rho_0}$ ) or  $Q_{sym}^0$  ( $= Q_{sym}(\rho_0) = 27\rho_0^3 \left( \frac{\partial^3 C_2}{\partial \rho^3} \right)_{\rho_0}$ )] and on the difference between the neutron and proton effective masses  $\Delta m_0^* [= (m_n^* - m_p^*)/m]$  in neutron-rich matter at  $\rho_0$ . The values of  $K_{sym}^0$  and  $Q_{sym}^0$ , in different parametrizations of the Skyrme energy density functional (EDF) lie in very wide ranges [ $-700 \text{ MeV} < K_{sym}^0 < 400 \text{ MeV}$ ;  $-800 \text{ MeV} < Q_{sym}^0 < 1500 \text{ MeV}$ ] [13, 14] whereas there are divergent predictions on the value of  $\Delta m_0^*$  from theoretical studies based on microscopic many-body theories [127, 128] or phenomenological approaches [129–132]. Such large uncertainties belie a satisfactory understanding of the isovector part of the nuclear interaction.

There is a sliver of expectation that the entities  $C_2^0$  ( $= C_2(\rho_0)$ ),  $L_0$ ,  $K_{sym}^0$ , etc. may have an intrinsic correlation among them. Finding a correlated structure for these symmetry energy elements helps in making a somewhat more precise statement on an otherwise uncertain isovector indicator as it may be tied up to other quantities known with more certainty.

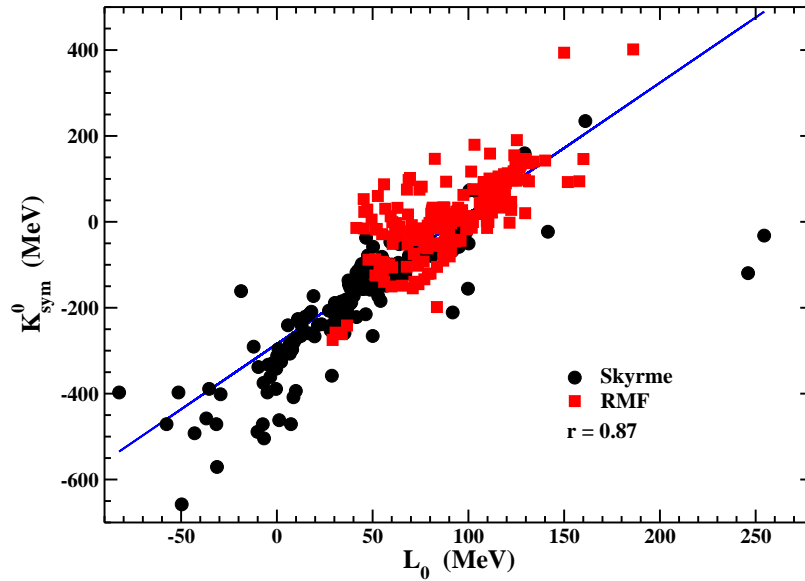


Figure 6.2: The correlation between  $L_0$  and  $K_{sym}^0$  is plotted for 500 relativistic and non-relativistic EDFs [13, 14]. The black circles correspond to the non-relativistic Skyrme-inspired EDFs, the red squares refer to those obtained from relativistic mean field (RMF) models.

The correlations need to be really strong so that one can extract meaningful constraints regarding the uncertain symmetry energy parameters. Moreover, the correlations should not depend on the choice of models. In Fig. (6.1) values of  $C_2^0$  are plotted against  $L_0$  using 500 mean-field models from the literature both relativistic and non-relativistic [13, 14]. Only a weak positive correlation was observed with correlation coefficient  $r = 0.73$ . With this degree of correlation, even with the precise information on  $C_2^0$ , one can not infer about the value of  $L_0$  with good precision.

From observation of the computed values of  $L_0$  and  $K_{sym}^0$  with selected sets of non-relativistic and relativistic EDFs, an empirical linear relationship between  $K_{sym}^0$  and  $L_0$  is also suggested [41, 103, 123, 131, 133–135]. For example, in Ref. [103], using a selective set of mean-field models the correlation coefficient was found to be  $r = 0.87$ . In Ref. [41], using a different set of mean-field models the correlation coefficient between the same

quantities was found to be  $r = 0.97$ . Clearly the correlation between  $K_{sym}^0$  and  $L_0$  has dependence on the choice of set of models. To understand the degree of model dependence in the correlation between  $K_{sym}^0$  and  $L_0$ , in Fig. (6.2)  $K_{sym}^0$  versus  $L_0$  is plotted for a diverse set of 500 relativistic and non-relativistic mean-field models as compiled by Dutra et al [13, 14]. The correlation coefficient was found to be  $r = 0.87$ , which is certainly not as high as it was found in [41]. To constrain the value  $K_{sym}^0$  from the better known nuclear matter properties, search for a universal correlation is thus called for.

## 6.2 Theoretical Framework

Using few basic equations of statistical mechanics, a theoretical framework to calculate the properties of nuclear matter is given in the following.

### 6.2.1 Symmetric Nuclear Matter

For symmetric nuclear matter at density  $\rho$ , with energy density  $\mathcal{H}$ , and at zero temperature ( $T = 0$ ), the chemical potential of the nucleon is given by

$$\mu = \mathcal{E}_F = \frac{P_F^2}{2m^*} + V = \frac{P_F^2}{2m} + U, \quad (6.1)$$

where  $\mathcal{E}_F$  is the Fermi energy,  $P_F$  is the Fermi momentum, the effective mass  $m^*$  and the single-particle potential  $V$  are given by  $\hbar^2/2m^* = \delta\mathcal{H}/\delta\mathcal{K}$  and  $V = \delta\mathcal{H}/\delta\rho$ , where  $\frac{\hbar^2}{2m}\mathcal{K}$  is the kinetic energy density. One also can redefine the single-particle potential as  $U$  by including within it the effective mass contribution, as done in the r.h.s. of Eq. (6.1). No special assumption about the nucleonic interaction is made except that it is density dependent to simulate many-body forces and that it depends quadratically on the momentum;

thus, the single-particle potential  $U$  separates into three parts,

$$U = V_0 + P_F^2 V_1 + V_2. \quad (6.2)$$

The term  $(V_0 + P_F^2 V_1)$  on the right is the Hartree-Fock potential and the last term  $V_2$  is the rearrangement potential that arises from the density dependence of the interaction. The term  $V_1$  comes from the momentum dependence:

$$\begin{aligned} \frac{P_F^2}{2m^*} &= \frac{P_F^2}{2m} + P_F^2 V_1 \\ \Rightarrow \frac{1}{m^*} &= \frac{1}{m} + 2V_1 \end{aligned} \quad (6.3)$$

In general,  $m^*$  is momentum and energy dependent, in the mean-field level the energy dependence is ignored and the momentum dependence is taken at the Fermi surface. The rearrangement energy does not enter explicitly in the energy expression when written in terms of the mean-field potential [136, 137], the energy per nucleon for SNM at density  $\rho$  is then given by,

$$\begin{aligned} e &= \frac{1}{2m} \langle p^2 \rangle + \frac{1}{2} \langle p^2 \rangle V_1 + \frac{1}{2} V_0 \\ &= \frac{\langle p^2 \rangle}{2m^*} \left( \frac{m^*}{m} + m^* V_1 \right) + \frac{1}{2} V_0 \\ &= \frac{\langle p^2 \rangle}{2m^*} \left( \frac{m^*}{m} + \frac{1}{2} - \frac{1}{2} \frac{m^*}{m} \right) + \frac{1}{2} V_0 \\ &= \frac{\langle p^2 \rangle}{2m^*} \frac{1}{2} \left( 1 + \frac{m^*}{m} \right) + \frac{1}{2} V_0 \\ &= \frac{1}{4} \left( \frac{1}{m} + \frac{1}{m^*} \right) \langle p^2 \rangle + \frac{1}{2} V_0 \\ &= \left( \frac{1}{m} + \frac{1}{m^*} \right) \frac{3P_F^2}{20} + \frac{1}{2} V_0. \end{aligned} \quad (6.4)$$

Here the average of the square of the momentum  $\langle p^2 \rangle$  is calculated by using the Fermi distribution  $\tilde{n}(p)$  as,

$$\begin{aligned}
\langle p^2 \rangle &= \frac{\int_0^{P_F} \tilde{n}(p) p^2 d^3p}{\int_0^{P_F} \tilde{n}(p) d^3p}; \quad \text{with } \tilde{n}(p) = \frac{1}{e^{\frac{E-E_F}{pT}} + 1} \\
&= \frac{4\pi \int_0^{P_F} \tilde{n}(p) p^2 p^2 dp}{4\pi \int_0^{P_F} \tilde{n}(p) p^2 dp} \\
\Rightarrow \langle p^2 \rangle &= \frac{3P_F^2}{5}. \tag{6.5}
\end{aligned}$$

To arrive at the last step, the fact was used that at  $T = 0$ , below Fermi energy  $E_F$  (i.e.  $E < E_F$ ),  $\tilde{n}(p) = 1$ . At  $T = 0$ , energy ( $E$ ) of a system is given by the Helmholtz free energy ( $F$ ) i.e.

$$F = E = -PV + \mu N. \tag{6.6}$$

Here,  $P, V, N$  are the pressure, volume and number of particles of the system, respectively. Immediately, energy per particle (nucleon)  $e$  can be connected to chemical potential  $\mu$  as,

$$\begin{aligned}
\frac{E}{N} &= -P \frac{V}{N} + \mu \\
\Rightarrow e &= -\frac{P}{\rho} + \mu \\
\Rightarrow \mu &= e + \frac{P}{\rho}. \tag{6.7}
\end{aligned}$$

This relation is known as the Gibbs-Duhem relation. At zero pressure this leads to the Hugenholtz-Van Hove theorem [138] which has recently been used to link nucleon single-particle characteristics to macroscopic isovector properties in Ref. [139]. Keeping this in mind, starting from equating Eqs. (6.1) and (6.7) and invoking Eqs. (6.4) and (6.2) therein



one can write,

$$\begin{aligned}
\frac{P_F^2}{2m} + U &= e + \frac{P}{\rho} \\
\Rightarrow \frac{P_F^2}{2m} + V_0 + P_F^2 V_1 + V_2 &= \left( \frac{1}{m} + \frac{1}{m^*} \right) \frac{3P_F^2}{20} + \frac{1}{2} V_0 + \frac{P}{\rho} \\
\Rightarrow \frac{P_F^2}{2m} + \frac{1}{2} V_0 + P_F^2 V_1 &= \left( \frac{1}{m} + \frac{1}{m^*} \right) \frac{3P_F^2}{20} + \frac{P}{\rho} - V_2 \\
\Rightarrow \left( \frac{1}{m} + \frac{1}{m} + 2V_1 \right) \frac{3P_F^2}{20} + \frac{1}{2} V_0 &= \left( \frac{1}{m} + \frac{1}{m^*} \right) \frac{3P_F^2}{20} + \frac{P}{\rho} - V_2 - \frac{P_F^2}{5m} - \frac{7}{10} P_F^2 V_1 \\
\Rightarrow \left( \frac{1}{m} + \frac{1}{m^*} \right) \frac{3P_F^2}{20} + \frac{1}{2} V_0 &= \left( \frac{1}{m} + \frac{1}{m^*} \right) \frac{3P_F^2}{20} + \frac{P}{\rho} - V_2 - \frac{P_F^2}{5m} \\
&\quad - \frac{7}{20} P_F^2 \left( \frac{1}{m^*} - \frac{1}{m} \right) \tag{6.8}
\end{aligned}$$

Recognizing L.H.S of the above equation from Eq. (6.4), the energy per nucleon for SNM can be written as [95],

$$\begin{aligned}
e &= \frac{3}{10} \frac{P_F^2}{m} - \frac{1}{5} \frac{P_F^2}{m^*} - V_2 + \frac{P}{\rho} \\
&= \frac{P_F^2}{10m} \left( 3 - 2 \frac{m}{m^*} \right) - V_2 + \frac{P}{\rho}. \tag{6.9}
\end{aligned}$$

The state dependence of single-particle effective potential can be taken care in terms of an effective mass of the nucleon  $m^*$ . In a non-relativistic prescription for SNM,  $\frac{m}{m^*}$  can be expanded as a function of  $\rho$  [140]. Keeping terms only upto linear in  $\rho$ , the expansion is given by [95]

$$\frac{m}{m^*(\rho)} = 1 + k\rho. \tag{6.10}$$

The density dependence of the rearrangement potential of SNM can be taken as [95],

$$V_2(\rho) = a\rho^{\tilde{\alpha}}. \quad (6.11)$$

Then, energy per nucleon  $e$  of SNM in Eq. (6.9) takes the form

$$\begin{aligned} e &= \frac{P_F^2}{10m} \left( 3 - 2\frac{m}{m^*} \right) - a\rho^{\tilde{\alpha}} + \frac{P}{\rho} \\ &= \frac{g^2 \left( \frac{\rho}{2} \right)^{\frac{2}{3}}}{5 \cdot 2m} (3 - 2 - 2k\rho) - a\rho^{\tilde{\alpha}} + \frac{P}{\rho} \\ &= \frac{\lambda}{5} \rho^{\frac{2}{3}} (1 - 2k\rho) - a\rho^{\tilde{\alpha}} + \frac{P}{\rho}. \end{aligned} \quad (6.12)$$

Here,  $\lambda$  is given by,  $\lambda = \frac{g^2}{2^{2/3} \cdot 2m}$ . The pressure for SNM is then given by,

$$P = \rho^2 \frac{\partial e}{\partial \rho} = \frac{\lambda}{15} \rho^{\frac{5}{3}} - \frac{1}{3} \lambda k \rho^{\frac{8}{3}} - \frac{1}{2} \tilde{\alpha} a \rho^{\tilde{\alpha}+1} + \frac{1}{2} \rho \frac{\partial P}{\partial \rho}. \quad (6.13)$$

At  $\rho = \rho_0$ , the pressure vanishes ( $P = 0$ ) and the incompressibility is given by  $K_0 = 9 \left. \frac{\partial P}{\partial \rho} \right|_{\rho=\rho_0}$ . Extracting the value of  $a\rho^{\tilde{\alpha}}$  from Eq. (6.12) at  $\rho_0$  ( $P = 0$ ) the above equation can give the value of  $\tilde{\alpha}$  as,

$$\begin{aligned} 0 &= \frac{\lambda}{15} \rho_0^{\frac{5}{3}} - \frac{1}{3} \lambda k \rho_0^{\frac{8}{3}} - \frac{1}{2} \tilde{\alpha} a \rho_0^{\tilde{\alpha}+1} + \rho_0 \frac{K_0}{18} \\ \Rightarrow 0 &= \frac{\lambda}{15} \rho_0^{\frac{2}{3}} - \frac{1}{3} \lambda k \rho_0^{\frac{5}{3}} - \frac{1}{2} \tilde{\alpha} (a\rho_0^{\tilde{\alpha}}) + \frac{K_0}{18} \\ \Rightarrow 0 &= \frac{\lambda}{15} \rho_0^{\frac{2}{3}} - \frac{1}{3} \lambda k \rho_0^{\frac{5}{3}} - \frac{1}{2} \tilde{\alpha} \left[ \frac{\lambda}{5} \rho_0^{\frac{2}{3}} (1 - 2k\rho_0) - e_0 \right] + \frac{K_0}{18} \\ \Rightarrow K_0 &= 18 \left\{ -\frac{\lambda}{15} \rho_0^{\frac{2}{3}} + \frac{1}{3} \lambda k \rho_0^{\frac{5}{3}} + \frac{1}{2} \tilde{\alpha} \left[ \frac{\lambda}{5} \rho_0^{\frac{2}{3}} (1 - 2k\rho_0) - e_0 \right] \right\} \\ \Rightarrow K_0 &= -\frac{6}{5} \lambda \rho_0^{\frac{2}{3}} + 6 \lambda \rho_0^{\frac{2}{3}} \left( \frac{m}{m^*} - 1 \right) + 9 \tilde{\alpha} \left[ \frac{\lambda}{5} \rho_0^{\frac{2}{3}} \left( 3 - 2\frac{m}{m^*} \right) - e_0 \right] \end{aligned}$$

$$\Rightarrow \tilde{\alpha} = \frac{K_0 + \frac{6}{5}\lambda\rho_0^{\frac{2}{3}} - 6\lambda\rho_0^{\frac{2}{3}}\left(\frac{m}{m_0^*} - 1\right)}{9\left[\frac{\lambda}{5}\rho_0^{\frac{2}{3}}\left(3 - 2\frac{m}{m_0^*}\right) - e_0\right]}. \quad (6.14)$$

Using the expression for Fermi energy at  $\rho_0$  as  $E_F^0 = \lambda\rho_0^{\frac{2}{3}}$  the value of  $\tilde{\alpha}$  can be written as

$$\tilde{\alpha} = \frac{\frac{K_0}{9} + \frac{E_F^0}{3}\left(\frac{12}{5} - 2\frac{m}{m_0^*}\right)}{\frac{E_F^0}{5}\left(3 - 2\frac{m}{m_0^*}\right) - e_0}. \quad (6.15)$$

## 6.2.2 Asymmetric Nuclear Matter

For asymmetric nuclear matter (ANM), the equation for the energy per nucleon can be generalized as

$$e(\rho, \delta) = \frac{1}{\rho} \left[ \sum_{\tau} \frac{P_{F,\tau}^2}{10m} \rho_{\tau} \left( 3 - 2\frac{m}{m_{\tau}^*(\rho)} \right) \right] - V_2(\rho, \delta) + \frac{P(\rho, \delta)}{\rho}. \quad (6.16)$$

In Eq.(6.16),  $\tau$  is the isospin index,  $\rho_{\tau} = (1 + \tau\delta)\rho/2$ ; here,  $\tau = 1$  for neutrons and  $\tau = -1$  for protons. The Fermi momentum for the individual species can be written as  $P_{F,\tau} = g\rho_{\tau}^{1/3}$  with  $g = (3\pi^2)^{1/3}\hbar$ . Generalizing the expression in Eq. (6.10) density-dependent nucleon effective mass for asymmetric matter is written as

$$\frac{m}{m_{\tau}^*(\rho)} = 1 + \frac{k_+}{2}\rho + \frac{k_-}{2}\rho\tau\delta. \quad (6.17)$$

The constant  $k_+$  for ANM in Eq. (6.17) is equivalent to  $k$  in Eq. (6.10) with  $k = \frac{k_+}{2}$ . Following the expression of rearrangement potential for SNM in Eq. (6.11) the density dependence in the rearrangement potential for asymmetric nuclear matter can be generalized

as (keeping upto  $\sim \delta^2$ )

$$V_2(\rho, \delta) = (a + b\delta^2)\rho^{\tilde{\alpha}}, \quad (6.18)$$

which is independent of the isospin index  $\tau$ . The constant  $a$  weighs the rearrangement potential for SNM, whereas the constant  $b$  is a measure of the asymmetry dependence of the rearrangement potential.

The energy per nucleon  $e(\rho, \delta)$  can also be written in terms of the symmetry energy coefficients as

$$\begin{aligned} e(\rho, \delta) &= e(\rho, \delta = 0) + \frac{1}{2!} \left( \frac{\partial^2 e(\rho, \delta)}{\partial \delta^2} \right)_{\delta=0} \delta^2 + \frac{1}{4!} \left( \frac{\partial^4 e(\rho, \delta)}{\partial \delta^4} \right)_{\delta=0} \delta^4 + \dots \\ &= e(\rho, 0) + C_2(\rho)\delta^2 + C_4(\rho)\delta^4 + \dots \end{aligned} \quad (6.19)$$

As the nuclear force is invariant under isospin exchange, only the even powers of  $\delta$  survive in the expansion of  $e(\rho, \delta)$ . An expression for the pressure  $P(\rho, \delta) = \rho^2 \frac{\partial e}{\partial \rho}$  follows from the above equation as,

$$\frac{P(\rho, \delta)}{\rho} = \rho \frac{\partial e(\rho, 0)}{\partial \rho} + \rho \frac{\partial C_2(\rho)}{\partial \rho} \delta^2 + \rho \frac{\partial C_4(\rho)}{\partial \rho} \delta^4 + \dots \quad (6.20)$$

The right hand side of Eq.(6.16) can be expanded in powers of  $\delta$  using the expressions for  $P(\rho, \delta)$  and  $V_2(\rho, \delta)$  and using Eq.(6.17), keeping only upto order of  $\delta^2$  in  $\frac{P(\rho, \delta)}{\rho}$  as,

$$e(\rho, \delta) = \frac{1}{\rho} \left[ \sum_{\tau} \frac{P_{F,\tau}^2}{10m} (1 + \tau\delta) \frac{\rho}{2} \left( 3 - 2 \frac{m}{m_{\tau}^*(\rho)} \right) \right] - V_2(\rho, \delta) + \rho \frac{\partial e(\rho, 0)}{\partial \rho} + \rho \frac{\partial C_2(\rho)}{\partial \rho} \delta^2$$

$$\begin{aligned}
&= \left[ \sum_{\tau} \frac{\{(3\pi^2)^{\frac{1}{3}} \hbar \rho_{\tau}^{\frac{1}{3}}\}^2 (1 + \tau\delta)}{10m} \frac{(1 + \tau\delta)}{2} (3 - 2 - k_{+}\rho - k_{-}\rho\tau\delta) \right] - V_2(\rho, \delta) \\
&\quad + \rho \frac{\partial e(\rho, 0)}{\partial \rho} + \rho \frac{\partial C_2(\rho)}{\partial \rho} \delta^2 \\
&= \frac{g^2}{10m} \frac{1}{2^{2/3} \cdot 2} \left[ \sum_{\tau} \{(1 + \tau\delta) \rho\}^{\frac{2}{3}} (1 + \tau\delta) (1 - k_{+}\rho - k_{-}\rho\tau\delta) \right] - (a + b\delta^2) \rho^{\tilde{\alpha}} \\
&\quad + \rho \frac{\partial e(\rho, 0)}{\partial \rho} + \rho \frac{\partial C_2(\rho)}{\partial \rho} \delta^2 \\
&= \frac{g^2}{10m} \frac{\rho^{\frac{2}{3}}}{2^{2/3} \cdot 2} \left[ \sum_{\tau=1, -1} (1 + \tau\delta)^{\frac{5}{3}} (1 - k_{+}\rho - k_{-}\rho\tau\delta) \right] - (a + b\delta^2) \rho^{\tilde{\alpha}} \\
&\quad + \rho \frac{\partial e(\rho, 0)}{\partial \rho} + \rho \frac{\partial C_2(\rho)}{\partial \rho} \delta^2 \\
&= \frac{g^2}{10m} \frac{\rho^{\frac{2}{3}}}{2^{2/3} \cdot 2} \left\{ \left[ (1 + \delta)^{\frac{5}{3}} (1 - k_{+}\rho - k_{-}\rho\delta) \right] + \left[ (1 - \delta)^{\frac{5}{3}} (1 - k_{+}\rho + k_{-}\rho\delta) \right] \right\} \\
&\quad - (a + b\delta^2) \rho^{\tilde{\alpha}} + \rho \frac{\partial e(\rho, 0)}{\partial \rho} + \rho \frac{\partial C_2(\rho)}{\partial \rho} \delta^2 \\
\Rightarrow e(\rho, \delta) &= \frac{g^2}{10m} \frac{\rho^{\frac{2}{3}}}{2^{2/3} \cdot 2} \left\{ \left[ \left( 1 + \frac{5}{3}\delta + \frac{5}{9}\delta^2 \right) (1 - k_{+}\rho - k_{-}\rho\delta) \right] \right. \\
&\quad \left. + \left[ \left( 1 - \frac{5}{3}\delta + \frac{5}{9}\delta^2 \right) (1 - k_{+}\rho + k_{-}\rho\delta) \right] \right\} \\
&\quad - (a + b\delta^2) \rho^{\tilde{\alpha}} + \rho \frac{\partial e(\rho, 0)}{\partial \rho} + \rho \frac{\partial C_2(\rho)}{\partial \rho} \delta^2 \tag{6.21}
\end{aligned}$$

### 6.2.3 Symmetry energy parameters

Comparing then with Eq.(6.19) and equating coefficients of the same order in  $\delta$ , one gets

the expression for  $C_2(\rho)$  by putting  $y = \frac{g^2}{10m} \frac{1}{2^{2/3}}$  as,

$$C_2(\rho) = -b\rho^{\tilde{\alpha}} + \rho \frac{\partial C_2(\rho)}{\partial \rho} + \frac{g^2}{10m} \frac{\rho^{\frac{2}{3}}}{2^{2/3} \cdot 2} \left[ -\frac{10}{3}k_{-}\rho + \frac{10}{9}(1 - k_{+}\rho) \right]$$

$$\Rightarrow C_2(\rho) = -b\rho^{\tilde{\alpha}} + \rho \frac{\partial C_2(\rho)}{\partial \rho} + y\rho^{\frac{2}{3}} \left[ -\frac{5}{3}k_{-\rho} + \frac{5}{9}(1 - k_{+\rho}) \right]. \quad (6.22)$$

The relation between  $C_2(\rho)$  and its density derivative is a direct consequence of the Gibbs-Duhem relation. Using  $k_{+\rho_0} = 2\left(\frac{m}{m_0^*} - 1\right)$  [ $\rho_0$  correspond to  $\delta = 0$ ; see Eq. (6.17)] at saturation, the symmetry energy coefficient  $C_2$  reads as,

$$\begin{aligned} C_2^0 &= -b\rho_0^{\tilde{\alpha}} + \frac{L_0}{3} + E_F^0 \left[ -\frac{1}{3}k_{-\rho_0} + \frac{1}{9}(1 - k_{+\rho_0}) \right] \\ &= -b\rho_0^{\tilde{\alpha}} + \frac{L_0}{3} + E_F^0 \left[ -\frac{1}{3}k_{-\rho_0} + \frac{1}{9} \left( 3 - 2\frac{m}{m_0^*} \right) \right], \end{aligned} \quad (6.23)$$

where  $E_F^0 = 5y\rho_0^{2/3}$  is the Fermi energy at  $\rho_0$ . Similar equations can be obtained for higher-order symmetry energy coefficients  $C_4, C_6$ , etc. which is not dealt here. The expressions for  $C_2$  or the higher-order symmetry energy coefficients so obtained are exact within the precincts of chosen premises. The second density derivative of  $C_2$  at  $\rho_0$  can be calculated from Eq. (6.22) as,

$$\left( \frac{\partial^2 C_2}{\partial \rho^2} \right)_{\rho_0} = \tilde{\alpha}b\rho_0^{\tilde{\alpha}-2} + y\rho_0^{-4/3} \left[ \frac{25}{27}k_{+\rho_0} + \frac{25}{9}k_{-\rho_0} - \frac{10}{27} \right]. \quad (6.24)$$

With the help of Eq. (6.23) expressions for  $K_{sym}^0$  reads,

$$\begin{aligned} K_{sym}^0 &= 9\rho_0^2 \left( \frac{\partial^2 C_2}{\partial \rho^2} \right)_{\rho_0} = 9\tilde{\alpha}b\rho_0^{\tilde{\alpha}} + \frac{9}{5}E_F^0 \left[ \frac{25}{27} \cdot 2 \left( \frac{m}{m_0^*} - 1 \right) + \frac{25}{9}k_{-\rho_0} - \frac{10}{27} \right] \\ &= 9\tilde{\alpha} \left[ \frac{L_0}{3} - C_2^0 + E_F^0 \left\{ -\frac{1}{3}k_{-\rho_0} + \frac{1}{9} \left( 3 - 2\frac{m}{m_0^*} \right) \right\} \right] + E_F^0 \left[ \frac{10}{3} \left( \frac{m}{m_0^*} - 1 \right) + 5k_{-\rho_0} - \frac{2}{3} \right] \\ &= 3\tilde{\alpha} [L_0 - 3C_2(\rho_0)] + \frac{2}{3}E_F^0 \frac{m}{m_0^*} (5 - 3\tilde{\alpha}) + E_F^0(3\tilde{\alpha} - 4) + E_F^0(k_{-\rho_0})(5 - 3\tilde{\alpha}) \\ &= -3\tilde{\alpha}[3C_2^0 - L_0] + E_F^0 \left[ (3\tilde{\alpha} - 4) + \left( \frac{2}{3} \frac{m}{m_0^*} + k_{-\rho_0} \right) (5 - 3\tilde{\alpha}) \right]. \end{aligned} \quad (6.25)$$

Using the penultimate step of the Eq. (6.25), expression for  $k_{-\rho_0}$  can be written as,

$$k_{-\rho_0} = \frac{K_{sym}^0 - 3\tilde{\alpha} [L_0 - 3C_2(\rho_0)] - \frac{2}{3}E_F^0 \frac{m}{m_0^*} (5 - 3\tilde{\alpha}) - E_F^0(3\tilde{\alpha} - 4)}{E_F^0(5 - 3\tilde{\alpha})}. \quad (6.26)$$

The third density derivative of  $C_2$  at  $\rho_0$  can be calculated from Eq. (6.22) as,

$$\left( \frac{\partial^3 C_2}{\partial \rho^3} \right)_{\rho_0} = \tilde{\alpha}(\tilde{\alpha} - 2)b\rho_0^{\tilde{\alpha}-3} - y\rho_0^{-7/3} \left[ \frac{25}{81}k_{+\rho_0} + \frac{25}{27}k_{-\rho_0} - \frac{40}{81} \right]. \quad (6.27)$$

Eventually utilizing the value of  $k_{-\rho_0}$  from Eq. (6.26), the symmetry element  $Q_{sym}^0$  is given by,

$$\begin{aligned} Q_{sym}^0 &= 27\rho_0^3 \left( \frac{\partial^3 C_2}{\partial \rho^3} \right)_{\rho_0} = 27\tilde{\alpha}(\tilde{\alpha} - 2)b\rho_0^{\tilde{\alpha}} - 27y\rho_0^{2/3} \left[ \frac{25}{81}k_{+\rho_0} + \frac{25}{27}k_{-\rho_0} - \frac{40}{81} \right] \\ &= 9\tilde{\alpha}(\tilde{\alpha} - 2)[L_0 - 3C_2(\rho_0)] - E_F^0 \frac{m}{m_0^*} \left\{ 6\tilde{\alpha}(\tilde{\alpha} - 2) + \frac{10}{3} \right\} + E_F^0[9\tilde{\alpha}(\tilde{\alpha} - 2) + 6] \\ &\quad - E_F^0(k_{-\rho_0})[9\tilde{\alpha}(\tilde{\alpha} - 2) + 5] \\ &= 9\tilde{\alpha}(\tilde{\alpha} - 2)[L_0 - 3C_2(\rho_0)] - E_F^0 \frac{m}{m_0^*} \left\{ 6\tilde{\alpha}(\tilde{\alpha} - 2) + \frac{10}{3} \right\} + E_F^0[9\tilde{\alpha}(\tilde{\alpha} - 2) + 6] \\ &\quad - \frac{E_F^0[9\tilde{\alpha}(\tilde{\alpha} - 2) + 5] \left[ K_{sym}^0 - 3\tilde{\alpha} [L_0 - 3C_2(\rho_0)] - \frac{2}{3}E_F^0 \frac{m}{m_0^*} (5 - 3\tilde{\alpha}) - E_F^0(3\tilde{\alpha} - 4) \right]}{E_F^0(5 - 3\tilde{\alpha})} \\ &= 15\tilde{\alpha}[3C_2^0 - L_0] + K_{sym}^0(3\tilde{\alpha} - 1) + E_F^0(2 - 3\tilde{\alpha}). \end{aligned} \quad (6.28)$$

While exploring the standard Skyrme EDFs, exactly the same correlated structure was found between  $K_{sym}^0$  or  $Q_{sym}^0$  and  $[3C_2^0 - L_0]$  as in Eqs. (6.25) and (6.28).

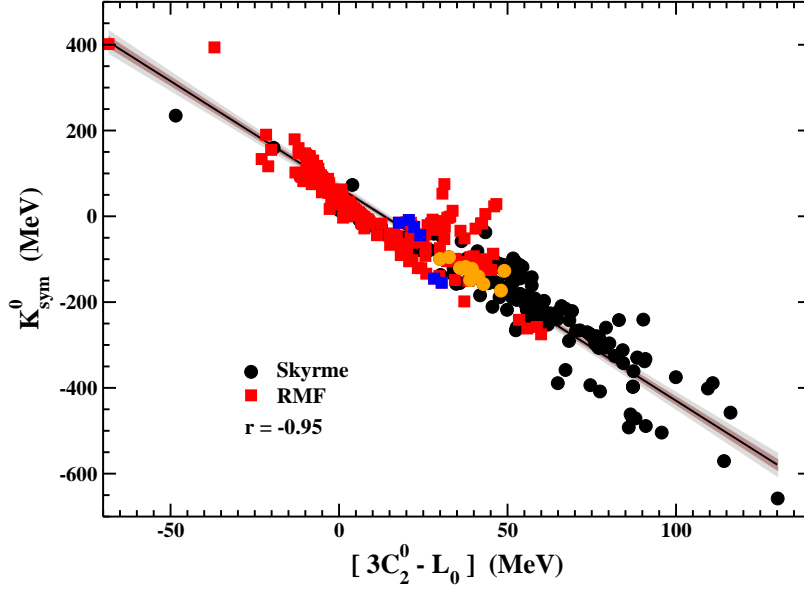


Figure 6.3: The correlation between  $K_{sym}^0$  and  $[3C_2^0 - L_0]$  as obtained from 500 EDFs [13, 14]. The black circles correspond to the Skyrme-inspired EDFs, the red squares refer to those obtained from RMF models. The models consistent with all the constraints demanded by Dutra et al. are highlighted by orange circles for Skyrme EDFs [13] and blue squares for RMF EDFs [14]. The inner (outer) colored regions around the best-fit straight line through these points depict the loci of 95% confidence (prediction) bands of the regression analysis.

### 6.3 Results and discussion

Eq. (6.25) throws a hint that there is a strong likelihood that  $K_{sym}^0$  calculated with different EDFs may be linearly correlated to  $[3C_2^0 - L_0]$ . This is realized from the correlated structure of  $K_{sym}^0$  with  $[3C_2^0 - L_0]$  as displayed in Fig.6.3 for five hundred energy density functionals [13, 14] that have been in use to explain nuclear properties. The results as presented in Fig. 6.3 span both the Skyrme-inspired nonrelativistic (black circles) EDFs which tend to have negative values for  $K_{sym}^0$  and also the relativistic mean-field EDFs (red squares) that tend to have larger, sometimes positive values for  $K_{sym}^0$ . Skyrme (orange circles) and RMF (blue squares) models chosen by Dutra et. al. [13, 14] which were found to satisfy specific constraints on nuclear matter and neutron star properties are highlighted.



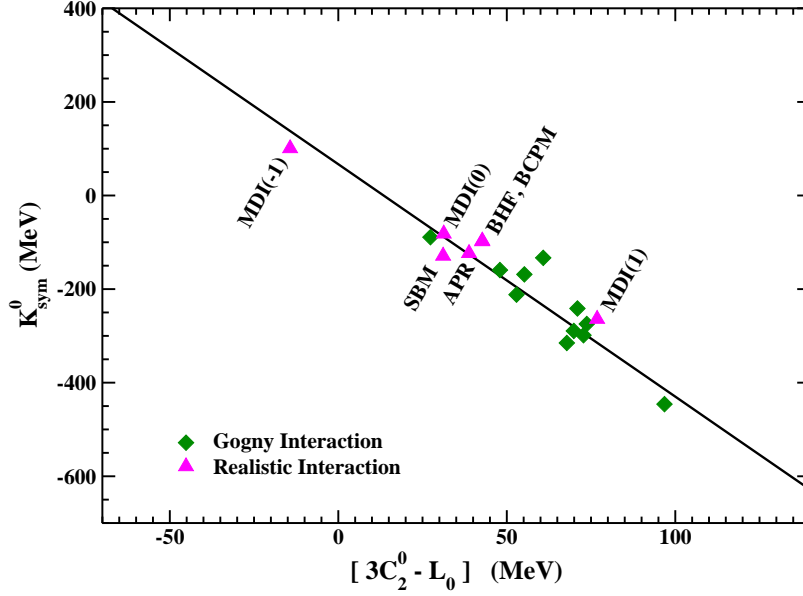


Figure 6.4: The correlation line between  $K_{sym}^0$  and  $[3C_2^0 - L_0]$  obtained from the Skyrme-RMF models in Fig. (6.3) is depicted. The magenta triangles are the results obtained from EDFs with realistic interactions, MDI(0), MDI(1), MDI(-1) [131], APR [141], BHF [142], BCPM [143] and SBM [144], respectively. The green diamonds represent results from a few Gogny interactions [130].

The linear correlation as observed seems to be nearly universal and intrinsic to an EDF consistent with nuclear properties. The correlation coefficient is seen to be  $r = -0.95$ . The near-universality in the correlation is brought into sharper focus in Fig. (6.4), where results corresponding to EDFs obtained from several realistic interactions (magenta triangles) and a few finite-range Gogny interactions (green diamonds) are displayed. They lie nearly on the correlation line. The linear regression analysis yields

$$K_{sym}^0 = d_1[3C_2^0 - L_0] + d_2, \quad (6.29)$$

with  $d_1 = -4.97 \pm 0.07$  and  $d_2 = 66.80 \pm 2.14$  MeV. This is a robust correlation among the symmetry energy elements. Incidentally, from the density-dependent M3Y (DDM3Y)

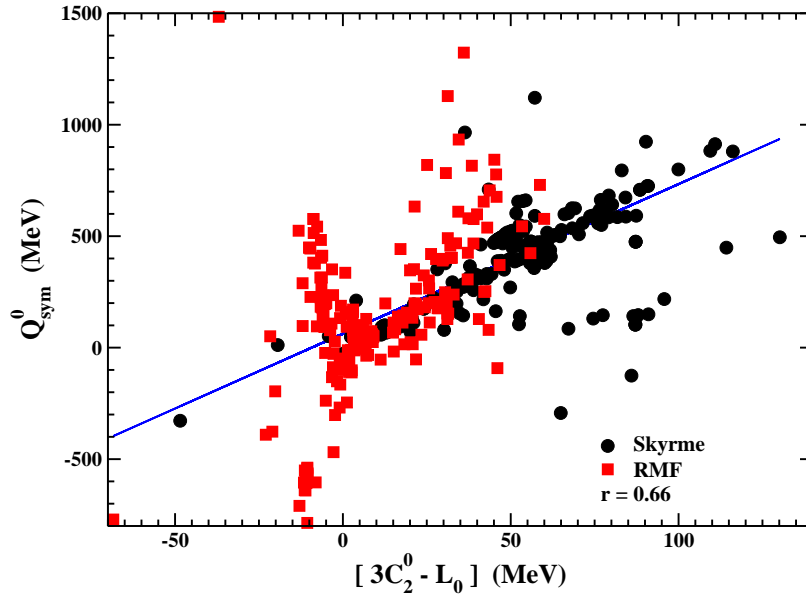


Figure 6.5: The correlation between  $Q_{sym}^0$  and  $[3C_2^0 - L_0]$  as obtained from 500 EDFs [13, 14]. The black circles correspond to the Skyrme-inspired EDFs, the red squares refer to those obtained from RMF models.

interaction, a similar kind of relation between these symmetry elements can be observed [41]. The correlation between the  $K_{sym}^0$  and  $L_0$  values from different effective forces and realistic interactions has also been considered in previous literature [41, 103, 123, 131, 133–135]. The results have shown relatively varying degrees of correlation (c.f. Figs (??) and (??)). In particular, the correlation between  $K_{sym}^0$  and  $L_0$  from all the 500 EDFs (see Fig. (6.2)) is not as strong as the correlated structure of  $K_{sym}^0$  with  $[3C_2^0 - L_0]$ .

Incidentally, a very similar correlated structure as  $K_{sym}^0$  is also anticipated for  $Q_{sym}^0$ , suggested by Eq. (6.28). In Fig. (6.5), values of  $Q_{sym}^0$  are plotted as a function of  $[3C_2^0 - L_0]$  for the same 500 models as in Fig. (6.3). However, the correlation between  $Q_{sym}^0$  with  $[3C_2^0 - L_0]$  is not as good as that for  $K_{sym}^0$ . The correlation coefficient is merely 0.66. One of the possible reason behind this is propagation of errors from  $K_{sym}^0$  in the right hand side of Eq. (6.28). Moreover, all three terms in the RHS of Eq. (6.28) have similar contributions

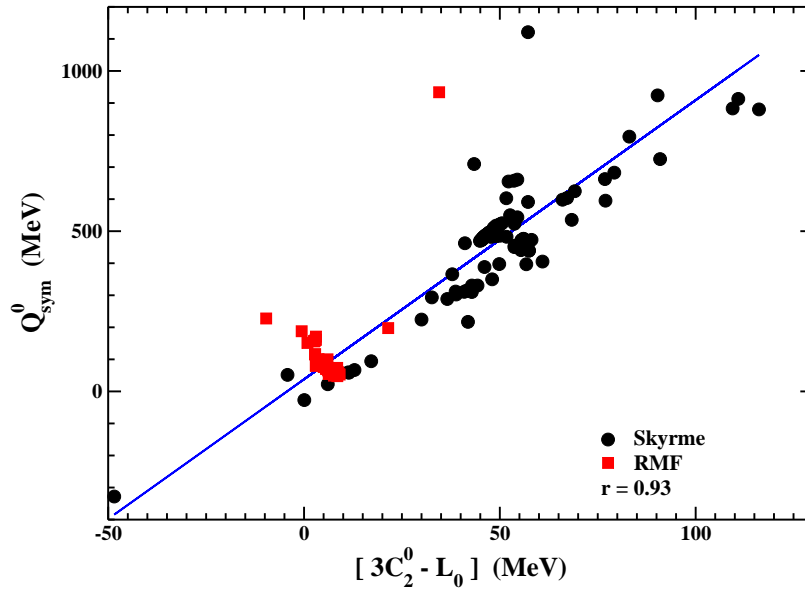


Figure 6.6: The correlation between  $Q_{sym}^0$  and  $[3C_2^0 - L_0]$  as obtained from  $\sim 200$  EDFs chosen from [13, 14] with constraints on  $K_0 = 230 \pm 30$  and  $\frac{m_0^*}{m} = 0.75 \pm 0.1$ . The black circles correspond to the Skyrme-inspired EDFs, the red squares refer to those obtained from RMF models.

to the value of  $Q_{sym}^0$  in terms of magnitude. Isoscalar properties like  $K_0$  or  $\frac{m_0^*}{m}$  may still possess some variation across the plethora of mean-field models compiled in Refs. [13, 14]. This can cause reasonable variation in the value of  $\tilde{\alpha}$  or  $E_F^0$  across different models, which might be screening the correlation between  $Q_{sym}^0$  and  $[3C_2^0 - L_0]$ . To limit the variation in  $\tilde{\alpha}$  and  $E_F^0$ , we restrict the values of  $K_0 = 230 \pm 30$  MeV and  $\frac{m_0^*}{m} = 0.75 \pm 0.1$  [42, 95]. This set of constraints are followed by  $\sim 110$  Skyrme models and  $\sim 80$  RMF models given in Refs. [13, 14]. In Fig. 6.6,  $Q_{sym}^0$  is plotted as a function of  $[3C_2^0 - L_0]$  for these  $\sim 200$  models. The correlation improved drastically for these constrained set of models with correlation coefficient  $r = 0.93$ . This again points out to the universal nature of the correlated structures, which were proposed by the analytical relations.

From accumulated experimental data over several decades and their theoretical analyses, there seems to be a broad consensus about the values of some of the nuclear constants.

The saturation density  $\rho_0$  of SNM, its energy per nucleon  $e_0$  and its incompressibility coefficient  $K_0$  are taken as a subset of the constants characterizing symmetric nuclear matter. The nucleon effective mass  $m_0^*$  for SNM at  $\rho_0$  is also taken as an input datum though its value is not as certain as  $e_0$  or  $\rho_0$ . Two more nuclear constants related to asymmetric nuclear matter (ANM) are further considered. They are the nuclear symmetry energy coefficients  $C_2(\rho)$  at  $\rho_0$  and at a somewhat lesser density  $\rho_1 (= 0.1 \text{ fm}^{-3})$ , “the crossing density”. There is less room for uncertainty in the symmetry energy coefficient  $C_2^0$  which has been determined from exploration of nuclear masses [1, 2]. With the realization that the nuclear observables related to average properties of nuclei constrain the nuclear EDFs better at around the average density of terrestrial atomic nuclei [145], the so-called “crossing density” [146] assumes a special significance. The symmetry energy  $C_2^1 (= C_2(\rho_1))$  at that density, in Skyrme EDFs is seen to be strongly correlated to the Giant Dipole Resonance (GDR) in spherical nuclei and is now fairly well constrained [29]. From the apparently universal, EDF-independent correlation between the isovector observables, the isovector elements  $L_0, K_{sym}^0$ , etc. can now be threaded to the above-mentioned nuclear constants as shown below.

With  $m_0^*$  as input,  $k_+$  is known. From given values of  $e_0, \rho_0$  and  $K_0$  for SNM,  $\tilde{\alpha}$  can be calculated as Eq. (6.15) [95]. The symmetry energy  $C_2(\rho_1)$  can be expressed as

$$C_2(\rho_1) = C_2^0 - L_0\epsilon + \frac{1}{2}K_{sym}^0\epsilon^2 - \frac{1}{6}Q_{sym}^0\epsilon^3 + \dots, \quad (6.30)$$

where  $\epsilon = \frac{(\rho_0 - \rho_1)}{3\rho_0}$ . From Eqs. (6.28), (6.29) and (6.30), ignoring terms beyond  $\epsilon^3$ , which are negligible,  $L_0, K_{sym}^0$  and  $Q_{sym}^0$  are calculated with known values of  $C_2^0$  and  $C_2^1$ . The constant  $k_-$  then follows from Eq. (6.25). From Eq. (6.17), the nucleon effective mass

splitting at saturation density to leading order in  $\delta$  is given as

$$\Delta m_0^* = \left( \frac{m_n^* - m_p^*}{m} \right)_{\rho_0} \simeq -k_- \rho_0 \left( \frac{m_0^*}{m} \right)^2 \delta, \quad (6.31)$$

where the approximation  $(m_n^* \cdot m_p^*) \simeq (m_0^*)^2$  is made.

Comparing Eqs. (6.25) and (6.29) one would expect  $|d_1|$  to be close to  $3\tilde{\alpha}$ . With the input values of the isoscalar nuclear constants  $e_0$ ,  $\rho_0$  and  $K_0$ ,  $3\tilde{\alpha}$  is seen to be 3.54 as opposed to  $\sim 5$  for  $|d_1|$ . The reason for this change seems to be two-fold, (a) all 500 EDFs employed in Fig. 6.3 have different values for  $\tilde{\alpha}$ , and (b) the RMF models are also included in the fit which have no explicit counterpart of  $\tilde{\alpha}$ .

In summary, the values of  $L_0$ ,  $K_{sym}^0$ ,  $Q_{sym}^0$  and  $\Delta m_0^*$  can be calculated in terms of empirically known nuclear constants namely,  $\rho_0$ ,  $e_0$ ,  $K_0$ ,  $C_2^0$ ,  $C_2^1$  and  $\frac{m_0^*}{m}$  using Eqs. (6.28)–(6.31). From the diverse theoretical endeavours like the liquid drop type models [1, 147, 148], the microscopic ab-initio or variational calculations [143, 149], or different Skyrme or RMF models – all initiated to explain varied experimental data, a representative set of the input nuclear constants for SNM is chosen with  $\rho_0 = 0.155 \pm 0.008 \text{ fm}^{-3}$  and  $e_0 = -16.0 \pm 0.2 \text{ MeV}$ . From microscopic analysis of isoscalar giant monopole resonances (ISGMR), the value of  $K_0$  is constrained as  $230 \pm 40 \text{ MeV}$  [145]. Analyzing the compact correlation between the 'experimental' double-differences of symmetry energies of finite nuclei and their mass number, Jiang et. al. [2] find  $C_2^0 = 32.1 \pm 0.3 \text{ MeV}$ . This value is included in the chosen set of nuclear constants. For  $C_2^1$ , the value  $C_2^1 = 24.1 \pm 0.8 \text{ MeV}$  as quoted from microscopic analysis of GDR in  $^{208}\text{Pb}$  [29] is taken. There is an overall consistency of this  $C_2^1$  value with those from the best-fit Skyrme EDFs [146] and with that given in [41]. For the nucleon effective mass, a value of  $\frac{m_0^*}{m} = 0.70 \pm 0.05$  is taken, this is consistent with the empirical values obtained from many analyses [150, 151].

The values of the symmetry energy elements calculated from Eqs. (6.28)–(6.31) using the values of input nuclear constants as mentioned come out to be  $L_0 = 60.3 \pm 14.5$  MeV,  $K_{sym}^0 = -111.8 \pm 71.3$  MeV,  $Q_{sym}^0 = 296.8 \pm 73.6$  MeV and  $\Delta m_0^* = (0.17 \pm 0.24)\delta$ . The value of  $L_0$  is remarkably close to its global average  $58.9 \pm 16$  MeV [152], obtained from analyses of terrestrial experiments and astrophysical observations. The value of  $L$  at  $\rho_1$  is calculated to be  $49.3 \pm 4.2$  MeV. From dipole polarizability in  $^{208}\text{Pb}$  an empirical value of  $L = 47.3 \pm 7.8$  MeV was obtained at  $\rho \simeq 0.11 \text{ fm}^{-3}$  [153]. There is no experimental value for  $K_{sym}^0$  or  $Q_{sym}^0$  to compare. However, the symmetry incompressibility  $K_\delta$  defined at the saturation density of nuclear matter at asymmetry  $\delta \left( K_\delta = K_{sym}^0 - 6L_0 - \frac{Q_0 L_0}{K_0} \right)$ , where  $Q_0 = 27\rho_0^3 \left( \frac{\partial^3 e}{\partial \rho^3} \right)_{\rho_0}$  has been extracted from breathing mode energies of Sn-isotopes [154]. Corrected for the nuclear surface term,  $K_\delta$  is quoted to be  $\simeq -350$  MeV [155]. This is in close agreement with the calculated value  $K_\delta = -378.6 \pm 17.0$  MeV;  $Q_0$  has been calculated from Eq. (6.16) to be  $-364.7 \pm 27.7$  MeV corresponding to  $\delta = 0$  [95] with the input nuclear constants mentioned.

The set of nuclear constants what is chosen in the present work is a conservative set; depending on possible new experimental inputs, their values may however change somewhat which would affect the calculated values of the density derivatives of the symmetry energy coefficients. The evaluated isovector elements are seen to be quite sensitive to the input quantities  $C_2^0$ ,  $C_2^1$  and  $\rho_0$ . There is still some variance in the choice of these input nuclear constants [96, 156, 157] besides the ones we have chosen. The aforesaid sensitivity can be gauged from the displayed six panels in Fig. 6.7. In the upper four panels (a)-(d), the contours of constant  $L_0$ ,  $K_{sym}^0$ ,  $Q_{sym}^0$  and  $\Delta m_0^*$  are shown in the  $C_2^0 - C_2^1$  plane in color shades, the white lines within the panels are the loci of constant isovector elements as marked when all other input elements are left unchanged. With increase in  $C_2^1$ ,  $L_0$  and  $K_{sym}^0$  are seen to decrease whereas  $Q_{sym}^0$  and  $\Delta m_0^*$  are found to increase. The opposite

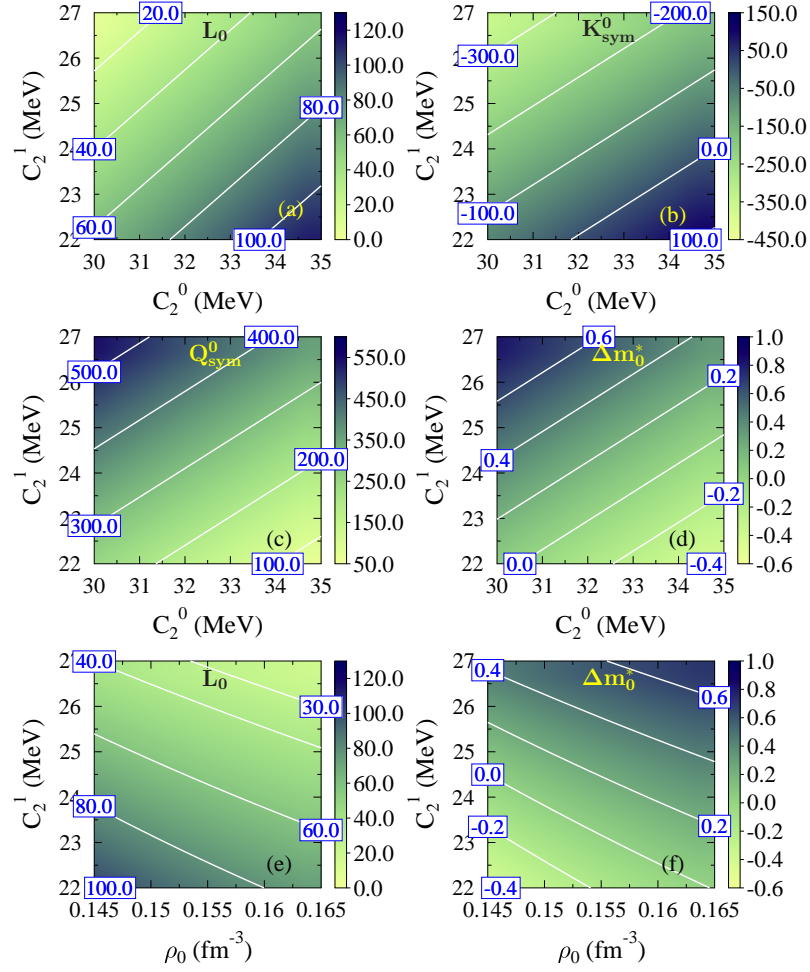


Figure 6.7: Contours of constant  $L_0$ ,  $K_{sym}^0$ ,  $Q_{sym}^0$  and  $\Delta m_0^*$  in color shades (as indicated on the right side of each panel) as functions of the input nuclear constants  $C_2^0$ ,  $C_2^1$  and  $\rho_0$  depicting the interdependence between various symmetry energy elements. The values of  $L_0$ ,  $K_{sym}^0$  and  $Q_{sym}^0$  are in units of MeV and those for  $\Delta m_0^*$  are in units of the free nucleon mass. For details, see text.

is observed for an increase in  $C_2^0$ . This points out the interdependence between different symmetry energy elements. The change in  $\rho_0$  has also a sizeable effect on the isovector elements. All other inputs remaining intact, an increase in  $\rho_0$  decreases  $L_0$  and  $K_{sym}^0$  and increases  $Q_{sym}^0$  and  $\Delta m_0^*$ . Only glimpses of these changes are shown in panels (e) and (f), where contours of constant  $L_0$  and  $\Delta m_0^*$  are drawn in the  $\rho_0 - C_2^1$  plane. The isovector elements as studied here are seen to be nearly insensitive to changes in  $e_0$  and  $m_0^*$  (not shown here). Similarly,  $K_0$  has little effect on these isovector elements except on  $\Delta m_0^*$ . An increase of  $K_0$  by, e.g.,  $\sim 30$  MeV is seen to push  $\Delta m_0^*$  drastically in the negative domain. Uncertainties in the input nuclear constants bear signature on the uncertainties in the calculated isovector elements.

## 6.4 Summary

To sum up, without reference to any specific nuclear interaction, with only a few reasonable approximations, analytic expressions for the density derivatives of the symmetry energy coefficient  $C_2(\rho)$  at the saturation density in terms of empirical nuclear constants are found out. The symmetry observables are seen to be sensitive to the values of the input nuclear constants, particularly to  $C_2^0$ ,  $C_2^1$  and  $\rho_0$ ; precise values of these constants are thus required to narrow down the uncertainties in the density dependence of the symmetry energy. In doing the calculations, a correlated structure connecting the different symmetry energy elements emerged. The consonance of these structures with those inherent in the plethora of EDFs based on relativistic and non-relativistic mean-field indicates a universality in the correlated structure in the symmetry energy coefficients. This helps further in a better realization of the information content of the isovector observables.



---

## SUMMARY AND FUTURE OUTLOOK

---

In this thesis work, we start from a general introduction to the nuclear symmetry energy arising from the asymmetry in the neutron-proton content of a nuclear system. Symmetry energy plays crucial roles in binding and shaping the finite nuclei as well as neutron stars. As the densities associated with finite nuclei and neutron stars are widely apart from each other, a microscopic description of symmetry energy over a wide range of density is very important. In this respect, importance of precise characterization of the properties of infinite nuclear matter, specially those which determine the density dependence of symmetry energy, is pointed out in the present work. As nuclear matter is not accessible in the laboratory, connecting the properties of nuclear matter to the observables of finite nuclei and neutron stars is very important. To this purpose, mean-field models both relativistic as well as non-relativistic are used in the present thesis work. In Chapter 2, details on the calculation of ground state properties e.g binding energy and charge radii of spherical nuclei are given in the mean-field formalism. The particulars are discussed both for a relativistic mean-field model and a non-relativistic one based on Skyrme force. A formal

introduction to the infinite nuclear matter properties is also given using both the relativistic and non-relativistic frameworks.

Throughout this thesis work, one of the primary motivation was to explore correlations of symmetry energy parameters to the properties of finite nuclei and neutron stars. Correlation between two quantities can be investigated in two ways: firstly, by exploring the two concerned quantities from a set of models or secondly, exploring them by means of a single model through a covariance analysis. The ingredients of optimizing the parameters of a model and eventually performing the covariance analysis is given in Chapter 3. By covariance analysis one can also calculate uncertainties in various quantities of interest, which gives a clear idea of relevance of proposing a new theoretical model. While performing the covariance analysis one obtains derivatives of different experimental observables of interest with respect to the model parameters, which can be further used to study the sensitivity of particular observables to different model parameters. Details of this sensitivity analysis is also given in Chapter 3.

Binding energies of finite nuclei are the most accurately known experimental quantities in nuclear physics. Information on these precisely known quantities are exploited in the literature to constrain the symmetry energy coefficient quite tightly. However, mean-field models obtained by fitting binding energies and charge radii of closed shell spherical nuclei show a wide variation in the slope of symmetry energy. In Chapter 4, it was identified that slope of symmetry energy can be constrained in a narrow range if the binding energies of extremely asymmetric nuclei (neutron number twice to that of protons) are included in the fit data to optimize the model parameters of a relativistic mean-field model. A sensitivity analysis was performed further to show quantitatively how the experimental data on binding energies of highly asymmetric nuclei help to constrain the value of different symmetry energy parameters.

To minimize the energy of an asymmetric nucleus, where the number of neutrons is higher than the protons, neutrons are pushed towards the surface giving rise to a neutron skin thickness. Droplet Model can account for this conclusion, which further suggests that slope of symmetry energy should be correlated to neutron skin thickness of a heavy nucleus. Exploration of microscopic mean-field models testify for the existence of this correlation. In Chapter 5, we point out that there might be a hint of model dependence in this correlation. Droplet Model provides a prescription for decomposing the neutron skin thickness into a bulk and surface part. The degree of model dependence in the correlation between slope of symmetry energy and neutron skin thickness of a heavy nucleus can be reduced if one looks for the correlation involving bulk part of the neutron skin thickness instead of total neutron skin thickness. An effective value of slope parameter is also suggested for a heavy nucleus in Chapter 5, which might be identified better with the experimental information on neutron skin thickness of a heavy nucleus.

In chapter 6, we start with some basic equations of statistical mechanics and arrive at the energy density functional of infinite nuclear matter with some reasonable assumptions. Analytical relations for different symmetry energy parameters are derived further, which show a dependence of higher order of symmetry energy parameters on the lower order ones. These inter-relationships are verified using 500 different mean-field models existing in the literature. Specially the correlation between curvature parameter of symmetry energy with linear combination of symmetry energy coefficient and its slope parameter is found to be a universal one.

In the present thesis work, parameters controlling the density dependence of symmetry energy are constrained by looking into different perspectives. A special attention is given to binding energies of highly asymmetric nuclei to constrain the slope parameter of the symmetry energy. This is realized by applying covariance analysis on a relativistic mean-

field model. Similar analyses should be performed with other type of mean-field models e.g. non-relativistic mean-field models based on Skyrme or Gogny force. It might clarify the robustness of the conclusions made in the present work with a particular variant of mean-field model.

The analytical relations we have derived using a simplistic model in Chapter 6 is followed by well tested Skyrme formalism. The quantities like isovector splitting of nucleon effective mass, which acquires a large range of values across different theoretical models, can be measured experimentally in near-future. The model we propose can be tested to explain the isovector splitting of nucleon effective mass in a simple way. One may also think of extending this formalism to explain the properties of finite nuclei, which might provide an alternative view of the finite nuclei in comparison to the modern mean-field models.

---

---

## BIBLIOGRAPHY

---

- [1] P. Möller, W. D. Myers, H. Sagawa, and S. Yoshida, *Phys. Rev. Lett* **108**, 052501 (2012).
- [2] H. Jiang, G. J. Fu, Y. M. Zhao, and A. Arima, *Phys. Rev. C* **85**, 024301 (2012).
- [3] W. D. Myers and W. J. Swiatecki, *Ann. Phys. (N. Y.)* **55**, 395 (1969).
- [4] W. D. Myers and W. J. Swiatecki, *Nucl. Phys.* **A336**, 267 (1980).
- [5] C. J. Horowitz and J. Piekarewicz, *Phys. Rev. Lett.* **86**, 5647 (2001).
- [6] S. Abrahamyan and et al., *Phys. Rev. Lett.* **108**, 112502 (2012).
- [7] D. J. Dubach and I. Sick, *Nucl. Phys. A* **503**, 589 (1989).
- [8] A. Tamii, I. Poltoratska, P. von Neumann-Cosel, Y. Fujita, T. Adachi, C. A. Bertulani, J. Carter, M. Dozono, H. Fujita, K. Fujita, K. Hatanaka, D. Ishikawa, M. Itoh, T. Kawabata, Y. Kalmykov, A. M. Krumbholz, E. Litvinova, H. Matsubara, K. Nakanishi, R. Neveling, H. Okamura, H. J. Ong, B. Özel-Tashenov, V. Y. Ponomarev, A. Richter, B. Rubio, H. Sakaguchi, Y. Sakemi, Y. Sasamoto, Y. Shimbara,

- Y. Shimizu, F. D. Smit, T. Suzuki, Y. Tameshige, J. Wambach, R. Yamada, M. Yosoi, and J. Zenihiro, *Phys. Rev. Lett.* **107**, 062502 (2011).
- [9] D. M. Rossi, P. Adrich, F. Aksouh, H. Alvarez-Pol, T. Aumann, J. Benlliure, M. Böhmer, K. Boretzky, E. Casarejos, M. Chartier, A. Chatillon, D. Cortina-Gil, U. Datta Pramanik, H. Emling, O. Ershova, B. Fernandez-Dominguez, H. Geissel, M. Gorska, M. Heil, H. T. Johansson, A. Junghans, A. Kelic-Heil, O. Kiselev, A. Klimkiewicz, J. V. Kratz, R. Krücken, N. Kurz, M. Labiche, T. Le Bleis, R. Lemmon, Y. A. Litvinov, K. Mahata, P. Maierbeck, A. Movsesyan, T. Nilsson, C. Nociforo, R. Palit, S. Paschalis, R. Plag, R. Reifarth, D. Savran, H. Scheit, H. Simon, K. Sümmerer, A. Wagner, W. Waluś, H. Weick, and M. Winkler, *Phys. Rev. Lett.* **111**, 242503 (2013).
- [10] X. Roca-Maza, M. Brenna, B. K. Agrawal, P. F. Bortignon, G. Colò, L.-G. Cao, N. Paar, and D. Vretenar, *Phys. Rev. C* **87**, 034301 (2013).
- [11] X. Roca-Maza, X. Viñas, M. Centelles, B. K. Agrawal, G. Colò, N. Paar, J. Piekarewicz, and D. Vretenar, *Phys. Rev. C* **92**, 064304 (2015).
- [12] L.-W. Chen, C. M. Ko, and B.-A. Li, *Phys. Rev. C* **72**, 064309 (2005).
- [13] M. Dutra, O. Lourenço, J. S. Sá Martins, A. Delfino, J. R. Stone, and P. D. Stevenson, *Phys. Rev. C* **85**, 035201 (2012).
- [14] M. Dutra, O. Lourenço, S. S. Avancini, B. V. Carlson, A. Delfino, D. P. Menezes, C. Providência, S. Typel, and J. R. Stone, *Phys. Rev. C* **90**, 055203 (2014).
- [15] M. Centelles, X. Roca-Maza, X. Viñas, and M. Warda, *Phys. Rev. Lett.* **102**, 122502 (2009).

- [16] C. Mondal, B. K. Agrawal, J. N. De, and S. K. Samaddar, *Phys. Rev. C* **93**, 044328 (2016).
- [17] C. Mondal, B. K. Agrawal, M. Centelles, G. Colò, X. Roca-Maza, N. Paar, X. Viñas, S. K. Singh, and S. K. Patra, *Phys. Rev. C* **93**, 064303 (2016).
- [18] N. K. Glendenning, *Compact Stars: Nuclear Physics, Particle Physics, and General Relativity* (Springer-Verlag, New York, 2000).
- [19] P. B. Demorest, T. Pennucci, S. M. Ransom, M. S. E. Roberts, and J. W. T. Hessels, *Nature* **467**, 1081 (2010).
- [20] J. Antoniadis and *et. al*, *Science* **340**, 448 (2013).
- [21] B. R. Barrett, P. Navrtil, and J. P. Vary, *Progress in Particle and Nuclear Physics* **69**, 131 (2013).
- [22] G. Hagen, T. Papenbrock, M. Hjorth-Jensen, and D. J. Dean, *Reports on Progress in Physics* **77**, 096302 (2014).
- [23] M. Bender, P. H. Heenen, and P.-G. Reinhard, *Rev. Mod. Phys.* **75**, 121 (2003).
- [24] M. Baldo and G. Burgio, *Progress in Particle and Nuclear Physics* **91**, 203 (2016).
- [25] A. W. Steiner and S. Gandolfi, *Phys. Rev. Lett.* **108**, 081102 (2012).
- [26] D. V. Shetty, S. J. Yennello, and G. A. Souliotis, *Phys. Rev. C* **75**, 034602 (2007).
- [27] M. A. F. et. al., *Phys. Rev. Lett.* **97**, 052701 (2006).
- [28] B.-A. Li, L.-W. Chen, and C. M. Ko, *Phys. Rep.* **464**, 113 (2008).
- [29] L. Trippa, G. Colò, and E. Vigezzi, *Phys. Rev. C* **77**, 061304(R) (2008).

- [30] X. Roca-Maza, M. Brenna, G. Colò, M. Centelles, X. Viñas, B. K. Agrawal, N. Paar, D. Vretenar, and J. Piekarewicz, *Phys. Rev. C* **88**, 024316 (2013).
- [31] A. Carbone, G. Colò, A. Bracco, L.-G. Cao, P. F. Bortignon, F. Camera, and O. Wieland, *Phys. Rev. C* **81**, 041301(R) (2010).
- [32] L.-W. Chen, *Phys. Rev. C* **83**, 044308 (2011).
- [33] M. B. Tsang and *et. al.*, *Phys. Rev. C* **86**, 015803 (2012).
- [34] T. Nikšić, D. Vretenar, and P. Ring, *Phys. Rev. C* **78**, 034318 (2008).
- [35] P. W. Zhao, Z. P. Li, J. M. Yao, and J. Meng, *Phys. Rev. C* **82**, 054319 (2010).
- [36] E. Chabanat, P. Bonche, P. Haensel, J. Meyer, and R. Schaeffer, *Nucl. Phys.* **A635**, 231 (1998).
- [37] X. Roca-Maza, G. Colò, and H. Sagawa, *Phys. Rev. C* **86**, 031306 (2012).
- [38] X. Roca-Maza, M. Centelles, X. Viñas, and M. Warda, *Phys. Rev. Lett.* **106**, 252501 (2011).
- [39] C. Mondal, B. K. Agrawal, and J. N. De, *Phys. Rev. C* **92**, 024302 (2015).
- [40] C. Mondal, B. K. Agrawal, J. N. De, and S. K. Samaddar, *Phys. Rev. C* **93**, 044328 (2016).
- [41] J. Dong, W. Zuo, J. Gu, and U. Lombardo, *Phys. Rev. C* **85**, 034308 (2012).
- [42] C. Mondal, B. K. Agrawal, J. N. De, S. K. Samaddar, M. Centelles, and X. Viñas, *Phys. Rev. C* **96**, 021302 (2017).
- [43] T. H. R. Skyrme, *Phil. Mag.* **1**, 1043 (1956).



- [44] T. H. R. Skyrme, Nucl. Phys. **9**, 615 (1959).
- [45] J. D. Walecka, Ann. Phys. (N.Y.) **83**, 491 (1974).
- [46] J. Boguta and A. R. Bodmer, Nucl. Phys. **A292**, 413 (1977).
- [47] W. Greiner and J. A. Maruhn, *Nuclear Models* (Springer-Verlag, Berlin; New York, 1996).
- [48] D. Vautherin and D. M. Brink, Phys. Rev. C **5**, 626 (1972).
- [49] S. K. Dhiman, R. Kumar, and B. K. Agrawal, Phys. Rev. C **76**, 045801 (2007).
- [50] B. G. Todd-Rutel and J. Piekarewicz, Phys. Rev. Lett **95**, 122501 (2005).
- [51] P. G. Reinhard, M. Rufa, J. Maruhn, W. Greiner, and J. Friedrich, Zeitschrift für Physik A Atomic Nuclei **323**, 13 (1986).
- [52] P. G. Reinhard, Rep. Prog. Phys. **52**, 439 (1989).
- [53] M. D. Estal, M. Centelles, X. Viñas, and S. K. Patra, Phys. Rev. C **63**, 024314 (2001).
- [54] J. Bardeen, L. N. Cooper, and J. R. Schrieffer, Phys. Rev. **106**, 162 (1957).
- [55] J. Bardeen, L. N. Cooper, and J. R. Schrieffer, Phys. Rev. **108**, 1175 (1957).
- [56] H. J. Lipkin, Annals of Physics **9**, 272 (1960).
- [57] Y. Nogami, Phys. Rev. **134**, B313 (1964).
- [58] G. E. P. Box, Journal of the American Statistical Association **71**, 791 (1976).
- [59] T. Editors, Phys. Rev. A **83**, 040001 (2011).

- [60] M. Kortelainen, T. Lesinski, J. Moré, W. Nazarewicz, J. Sarich, N. Schunck, M. V. Stoitsov, and S. Wild, *Phys. Rev. C* **82**, 024313 (2010).
- [61] P.-G. Reinhard and W. Nazarewicz, *Phys. Rev. C* **81**, 051303 (2010).
- [62] J. Dobaczewski, W. Nazarewicz, and P.-G. Reinhard, *Journal of Physics G: Nuclear and Particle Physics* **41**, 074001 (2014).
- [63] J. Piekarewicz, W.-C. Chen, and F. J. Fattoyev, *Journal of Physics G: Nuclear and Particle Physics* **42**, 034018 (2015).
- [64] J. Erler and P.-G. Reinhard, *Journal of Physics G: Nuclear and Particle Physics* **42**, 034026 (2015).
- [65] S. Brandt, *Statistical and Computational Methods in Data Analysis* (Springer, New York, 3rd English edition, 1997).
- [66] N. Metropolis, A. W. Rosenbluth, M. N. Rosenbluth, A. H. Teller, and E. Teller, *J. Chem. Phys.* **21**, 1087 (1953).
- [67] W. H. Press, S. A. Teukolsky, W. T. Vetterling, and B. P. Flannery, *Numerical Recipes in Fortran* (Cambridge University Press, 1992).
- [68] M. Kortelainen, J. McDonnell, W. Nazarewicz, P.-G. Reinhard, J. Sarich, N. Schunck, M. V. Stoitsov, and S. M. Wild, *Phys. Rev. C* **85**, 024304 (2012).
- [69] R. T. Birge, *Phys. Rev.* **40**, 207 (1932).
- [70] W. D. Myers and W. J. Swiatecki, *Nuclear Physics* **81**, 1 (1966).
- [71] P. Möller, J. Nix, W. Myers, and W. Swiatecki, *Atomic Data and Nuclear Data Tables* **59**, 185 (1995).

- [72] K. Pomorski and J. Dudek, Phys. Rev. C **67**, 044316 (2003).
- [73] C. Xu, B.-A. Li, and L.-W. Chen, Phys. Rev. C **82**, 054607 (2010).
- [74] B. K. Agrawal, J. N. De, and S. K. Samaddar, Phys. Rev. Lett. **109**, 262501 (2012).
- [75] B. K. Agrawal, J. N. De, S. K. Samaddar, G. Colo, and A. Sulaksono, Phys. Rev. C **87**, 051306(R) (2013).
- [76] B. A. Brown, Phys. Rev. Lett. **85**, 5296 (2000).
- [77] R. Kanungo and *et al*, Phys. Rev. Lett. **102**, 152501 (2009).
- [78] R. V. F. Janssens, Nature **459**, 1069 (2009).
- [79] B. K. Agrawal, Phys. Rev. C **81**, 034323 (2010).
- [80] G. A. Lalazissis, J. Konig, and P. Ring, Phys. Rev. C **55**, 540 (1997).
- [81] D. Vretenar, T. Nikšić, and P. Ring, Phys. Rev. C **68**, 024310 (2003).
- [82] R. Furnstahl, B. D. Serot, and H.-B. Tang, Nucl. Phys. **A615**, 441 (1997).
- [83] J. Boguta and H. Stoecker, Phys.Lett. **B120**, 289 (1983).
- [84] P. R. Bevington, *Data Reduction and Error Analysis for the Physical Sciences* (McGraw-Hill, New York, 1969).
- [85] P. Klüpfel, P.-G. Reinhard, T. J. Burvenich, and J. A. Maruhn, Phys. Rev. C **79**, 034310 (2009).
- [86] G. Audi, F. G. Kondev, M. Wang, B. Pfeiffer, X. Sun, J. Blachot, and M. MacCormick, Chin. Phys. C **36**, 12 (2012).

- [87] I. Angeli and K. Marinova, *Atomic Data and Nuclear Data Tables* **99**, 69 (2013).
- [88] W.-C. Chen and J. Piekarewicz, *Phys. Lett. B* **748**, 284 (2015).
- [89] M. Wang, G. Audi, A. Wapstra, F. Kondev, M. MacCormick, X. Xu, and B. Pfeiffer, *Chinese Physics C* **36**, 1603 (2012).
- [90] A. T. Gallant, J. C. Bale, T. Brunner, U. Chowdhury, S. Ettenauer, A. Lennarz, D. Robertson, V. V. Simon, A. Chaudhuri, J. D. Holt, A. A. Kwiatkowski, E. Mané, J. Menéndez, B. E. Schultz, M. C. Simon, C. Andreoiu, P. Delheij, M. R. Pearson, H. Savajols, A. Schwenk, and J. Dilling, *Phys. Rev. Lett.* **109**, 032506 (2012).
- [91] F. Wienholtz and *et. al.*, *Nature* **498**, 346 (2013).
- [92] C. J. Horowitz and J. Piekarewicz, *Phys. Rev. C* **64**, 062802(R) (2001).
- [93] R. Wang and L.-W. Chen, *Phys. Rev. C* **92**, 031303 (2015).
- [94] T. Sil, M. Centelles, X. Viñas, and J. Piekarewicz, *Phys. Rev. C* **71**, 045502 (2005).
- [95] J. N. De, S. K. Samaddar, and B. K. Agrawal, *Phys. Rev. C* **92**, 014304 (2015).
- [96] Z. Zhang and L.-W. Chen, *Physics Letters B* **726**, 234 (2013).
- [97] Z. Zhang and L.-W. Chen, *Phys. Rev. C* **92**, 031301 (2015).
- [98] B. A. Brown and S. Typel, *Phys. Rev. C* **64**, 027302 (2001).
- [99] R. Furnstahl, *Nucl. Phys. A* **706**, 85 (2002).
- [100] M. Warda, X. Viñas, X. Roca-Maza, and M. Centelles, *Phys. Rev. C* **80**, 024316 (2009).

- [101] P. Danielewicz, Nuclear Physics A **727**, 233 (2003).
- [102] S. S. Avancini, J. R. Marinelli, D. P. Menezes, M. M. W. Moraes, and C. Providência, Phys. Rev. C **75**, 055805 (2007).
- [103] I. Vidaña, C. Providência, A. Polls, and A. Rios, Phys. Rev. C **80**, 045806 (2009).
- [104] W. Satuła, R. A. Wyss, and M. Rafalski, Phys. Rev. C **74**, 011301 (2006).
- [105] M. Centelles, X. Roca-Maza, X. Viñas, and M. Warda, Phys. Rev. C **82**, 054314 (2010).
- [106] G. W. Hoffmann and et al., Phys. Rev. C **21**, 1488 (1980).
- [107] J. Zenihiro and et al., Phys. Rev. C **82**, 044611 (2010).
- [108] A. Krasznahorkay, H. Akimune, A. van den Berg, N. Blasi, S. Brandenburg, M. Csatos, M. Fujiwara, J. Gulyas, M. Harakeh, and M. H. et al., Nucl. Phys. **A731**, 224 (2004).
- [109] B. Klos and *et. al.*, Phys. Rev. C **76**, 014311 (2007).
- [110] E. Friedman and *et. al.*, Hyperfine Interact. **193**, 33 (2009).
- [111] C. M. Tarbert and D. P. W. *et al.*, Phys. Rev. Lett. **112**, 242502 (2014).
- [112] <http://hallaweb.jlab.org/parity/prex>. (2014).
- [113] T. Hashimoto, A. M. Krumbholz, P.-G. Reinhard, A. Tamii, P. von Neumann-Cosel, T. Adachi, N. Aoi, C. A. Bertulani, H. Fujita, Y. Fujita, E. Ganioglu, K. Hatanaka, E. Ideguchi, C. Iwamoto, T. Kawabata, N. T. Khai, A. Krugmann, D. Martin, H. Matsubara, K. Miki, R. Neveling, H. Okamura, H. J. Ong, I. Poltoratska, V. Y. Ponomarev, A. Richter, H. Sakaguchi, Y. Shimbara, Y. Shimizu, J. Simonis, F. D. Smit,

- G. Süsoy, T. Suzuki, J. H. Thies, M. Yosoi, and J. Zenihiro, Phys. Rev. C **92**, 031305 (2015).
- [114] B. A. Brown, W. A. Richter, and R. Lindsay, Phys. Lett. B **483**, 49 (2000).
- [115] R. W. Hasse and W. D. Myers, *Geometrical Relationships of Macroscopic Nuclear Physics* (Springer-Verlag, Heidelberg, 1988).
- [116] M. Warda, X. Viñas, X. Roca-Maza, and M. Centelles, Phys. Rev. C **81**, 054309 (2010).
- [117] M. Centelles, M. D. Estal, and X. Viñas, Nuclear Physics A **635**, 193 (1998).
- [118] M. D. Estal, M. Centelles, and X. Viñas, Nuclear Physics A **650**, 443 (1999).
- [119] J. Liu, Z. Ren, C. Xu, and R. Xu, Phys. Rev. C **88**, 024324 (2013).
- [120] B. K. Agrawal, S. Shlomo, and V. K. Au, Phys. Rev. C **72**, 014310 (2005).
- [121] N. R. Draper and H. Smith, *Applied Regression Analysis* (Wiley, New York, 1981).
- [122] X. Fan, J. Dong, and W. Zuo, Phys. Rev. C **89**, 017305 (2014).
- [123] P. Danielewicz and J. Lee, Nucl. Phys. A **818**, 36 (2009).
- [124] J. M. Lattimer and Y. Lim, Ap. J. **771**, 51 (2013).
- [125] J. Piekarewicz, B. K. Agrawal, G. Colò, W. Nazarewicz, N. Paar, P.-G. Reinhard, X. Roca-Maza, and D. Vretenar, Phys. Rev. C **85**, 041302(R) (2012).
- [126] B.-A. Li and L.-W. Chen, Modern Physics Letters A **30**, 1530010 (2015).
- [127] W. Zuo, L. G. Cao, B. A. Li, U. Lombardo, and C. W. Shen, Phys. Rev. C **72**, 014005 (2005).

- [128] E. N. E. van Dalen, C. Fuchs, and A. Faessler, Phys. Rev. Lett. **95**, 022302 (2005).
- [129] L. Ou, Z. Li, Y. Zhang, and M. Liu, Phys. Lett. B **697**, 246 (2011).
- [130] R. Sellahewa and A. Rios, Phys. Rev. C **90**, 054327 (2014).
- [131] L.-W. Chen, B.-J. Cai, C. M. Ko, B.-A. Li, C. Shen, and J. Xu, Phys. Rev. C **80**, 014322 (2009).
- [132] H.-Y. Kong, J. Xu, L.-W. Chen, B.-A. Li, and Y.-G. Ma, Phys. Rev. C **95**, 034324 (2017).
- [133] S. Yoshida and H. Sagawa, Phys. Rev. C **73**, 044320 (2006).
- [134] C. Ducoin, J. Margueron, C. Providência, and I. Vidaña, Phys. Rev. C **83**, 045810 (2011).
- [135] B. M. Santos, M. Dutra, O. Lourenço, and A. Delfino, Phys. Rev. C **90**, 035203 (2014).
- [136] K. A. Brueckner and D. T. Goldman, Phys. Rev. **116**, 424 (1959).
- [137] D. Bandyopadhyay, C. Samanta, S. K. Samaddar, and J. N. De, Nuclear Physics A **511**, 1 (1990).
- [138] N. Hugenholtz and L. van Hove, Physica **24**, 363 (1958).
- [139] R. Chen, B.-J. Cai, L.-W. Chen, B.-A. Li, X.-H. Li, and C. Xu, Phys. Rev. C **85**, 024305 (2012).
- [140] M. Baldo, G. F. Burgio, H.-J. Schulze, and G. Taranto, Phys. Rev. C **89**, 048801 (2014).

- [141] A. Akmal, V. Pandharipande, and D. Ravenhall, Phys. Rev. C **58**, 1804 (1998).
- [142] G. Taranto, M. Baldo, and G. F. Burgio, Phys. Rev. C **87**, 045803 (2013).
- [143] M. Baldo, L. M. Robledo, P. Schuck, and X. Viñas, Phys. Rev. C **87**, 064305 (2013).
- [144] B. K. Agrawal, S. K. Samaddar, J. N. De, C. Mondal, and S. De, International Journal of Modern Physics E **26**, 1750022 (2017).
- [145] E. Khan, J. Margueron, and I. Vidaña, Phys. Rev. Lett. **109**, 092501 (2012).
- [146] B. A. Brown, Phys. Rev. Lett. **111**, 232502 (2013).
- [147] W. D. Myers and W. J. Swiatecki, Phys. Rev. C **57**, 3020 (1998).
- [148] W.D.Myers and W.J.Swiaeteci, Nucl. Phys. **A601**, 141 (1996).
- [149] A. Akmal and V. R. Pandharipande, Phys. Rev. C **56**, 2261 (1997).
- [150] M. Jaminon and C. Mahaux, Phys. Rev. C **40**, 354 (1989).
- [151] X.-H. Li, W.-J. Guo, B.-A. Li, L.-W. Chen, F. J. Fattoyev, and W. G. Newton, Phys. Lett. B **743**, 408 (2015).
- [152] B.-A. Li and X. Han, Phys. Lett. B **727**, 276 (2013).
- [153] Z. Zhang and L.-W. Chen, Phys. Rev. C **90**, 064317 (2014).
- [154] T. Li and et al, Phys. Rev. Lett. **99**, 162503 (2007).
- [155] J. M. Pearson, N. Chamel, and S. Goriely, Phys. Rev. C **82**, 037301 (2010).
- [156] C. Li-Gang and M. Zhong-Yu, Chinese Physics Letters **25**, 1625 (2008).
- [157] M. Liu, N. Wang, Z.-X. Li, and F.-S. Zhang, Phys. Rev. C **82**, 064306 (2010).



